博士論文

Nonlinear internal wave generation around islands in stratified shear flow

（成層シア流が通過する島周辺における非線形内部波の生成）

小平　翼

Acknowledgements

My sincere thanks and respect go to my advisor, Professor Takuji Waseda, for his considerable guidance throughout my graduate study, his encouragement to the challenging research, his enthusiasm and insight in research. I gratefully acknowledge the many contributions Dr. Waseda has made to my personal and scientific development.

Special thanks are due Professor Motoyasu Miyata and Professor Wooyoung Choi. Their guidance was very helpful to build basis of this study. Although it was not included in this thesis, an experimental work on internal solitary wave conducted under the supervision of them and Dr.Waseda was precious opportunity for me. I appreciate the support from Dr.Choi to realize the experimental work.

I would like to thank the members of my committee. The guidance and assistant from Professor Toshiyuki Hibiya has surely contributed to this study. The advice from Professor Rheem Chang-Kyu was very helpful to clarify an achievement of this study. The comments from Professor Hiroyasu Hasumi and Dr Shinichiro Hirabayashi were more than helpful to put together this dissertation.

I would also like to thank JCOPE2 group in JAMSTEC. The talks given in their weekly seminar provided me knowledge of recent development in physical oceanography and their comments to my talk improved the quality of this study.

I would like to thank JSPS (Japan Society of Promotion of Science) for their financial support that enable me to go through the graduate study.

Numerical simulation of this research is partly carried out with super computer FX10 operated by Supercomputing Division, Information Technology Center, the University of Tokyo. The use of FX10 was quite helpful.

Finally, I would like to thank my family and friends, for providing me the support and encouragement.

Abstract

Synthetic Aperture Radar (SAR) has the potential to provide an immense amount of oceanic information. Previous studies have revealed that SAR images have manifested nonlinear oceanic internal waves (Alpers, 1985). We found more than 10 SAR images that show parabolic patterns around the Miyake and Mikura Islands. The parabolic signature (Fig.1) is reminiscent of a detached shock wave around obstacle in a compressible fluid. The islands are located in the pathway of the Kuroshio, and the flow speed was comparable to the propagation speed of the internal waves. So, the pattern was estimated to have been a manifestation of the nonlinear internal waves generated by a near critical stratified shear flow, the Kuroshio. It has not been studied even with the simplified topography and the topic is quite novel in the field of physical oceanography and fluid mechanics. In addition, if the SAR images exhibit nonlinear oceanic internal waves, it means that the SAR image provides information of small-scale oceanic process around the islands. Clarification of the small-scale processes around the islands is necessary for improvement of ocean modeling and a better understanding of ocean dynamics related to the Kuroshio. This study aims to clarify the nonlinear internal wave generation around the island in the Kuroshio and to better understand its generation mechanism.

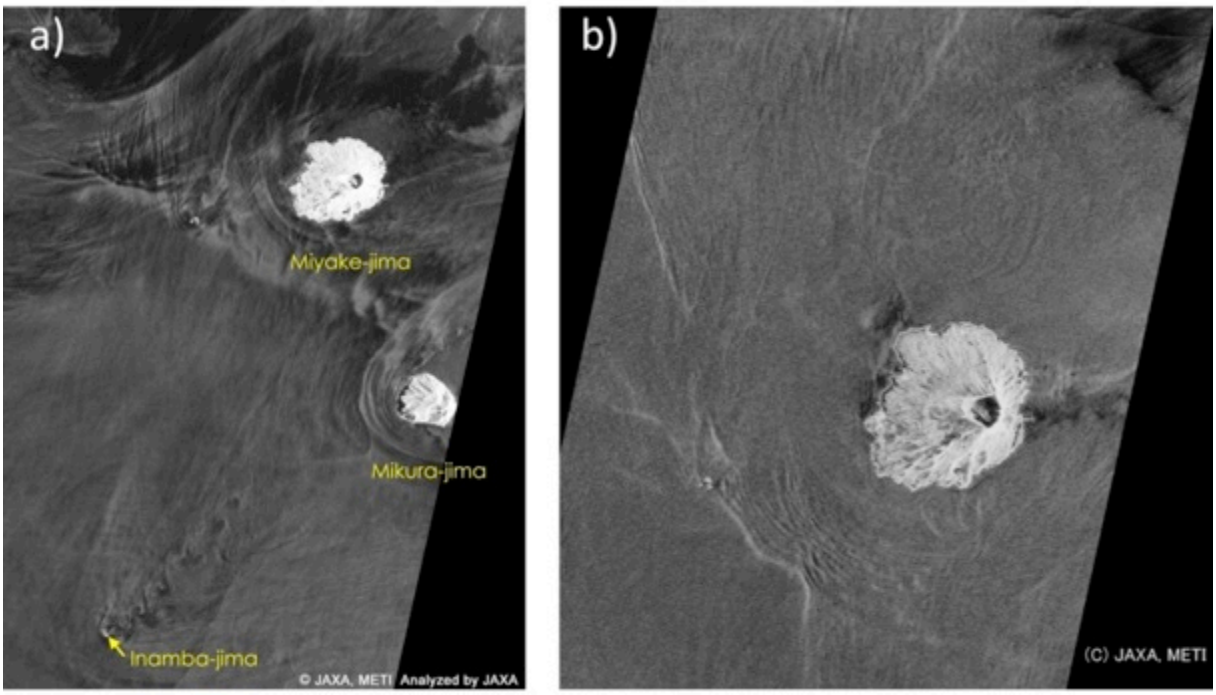

Fig.1 SAR images with parabola patterns obtained by ALOS/PALSAR at 19th of July 2006 (left, a), source: http://www.eorc.jaxa.jp/ALOS/img_up/l_pal_060612.htm,) and at 30th of August 2010 (right). Courtesy of JAXA/METI.

To demonstrate the idea that the Kuroshio traps the nonlinear internal wave, the relationship between SAR images within the Kuroshio must be investigated. We collected the SAR images showing parabolic patterns around the Miyake and Mikura Islands, and the patterns are shown in 13 days of 138 days among the published images from 2006 to 2011. Every image was taken when the Kuroshio approached the island based on the distance between the Miyake Island and the Kuroshio axis as reported in Quick Bulletin of Ocean Conditions. The maximum separation distance was 30 miles. For some cases, tidal flow might have increased the flow speed of the Kuroshio since the images were taken when the tidal gauge record was at a minimum. To discriminate the wind effect, in situ wind measurements were also studied, and we found that, when the images were taken, the average speeds were 2.8 m/s and 4.1 m/s at two observation stations in the Miyake Island. The gentle wind speed indicated that the parabolic patterns were not induced by wind, but rather the wind would enable the oceanic internal wave to be manifested in SAR images. These results support the idea that the Kuroshio plays a central role in creating the parabolic surface signatures by exciting internal waves. The analysis of JCOPE2 oceanic reanalysis data showed the Froude number did not change considerably between the seasons and the values indicate that mode-2 waves were likely to be trapped, while mode-1 waves were not. It was also found that internal waves with particular amplitude induce a greater velocity at surface, and the nonlinearity is larger in the summer season. As a result of analysis of the environmental condition, it can be said that both the summer season wind and oceanic stratification improve detection of mode-2 internal waves in SAR images.

To examine the idea that the Kuroshio induced trapped nonlinear internal waves around the islands, non-hydrostatic numerical simulations were conducted with horizontal grid resolution of 200 m. The initial and boundary conditions were set with vertical profiles of the Kuroshio axis reproduced in JCOPE2. As a result, a mode-2 internal wave was trapped and the parabolic pattern was observed in surface convergence field (Fig.2). The comparison between the simulations with stratification for summer and winter season revealed that mode-2 internal waves were trapped in both seasons, but the surface manifestation was more prominent in the summer season. This was consistent with the analysis of oceanic reanalysis data. Although the numerical simulations reproduced trapped internal waves around the Miyake Island which created a parabolic pattern in surface convergence field, the amplitude was small and the nonlinear characteristic was not clearly observed. Because of the possible shortcomings of observation and reanalysis, the density profile and the incoming flow speed of

the Kuroshio was artificially modified in the numerical experiment. The simulation indicated that nonlinear internal waves can be generated and be trapped around the islands under certain conditions, which warrants further observational studies. In addition to the mode-2 nonlinear internal waves, mode-1 nonlinear internal waves were also generated under extreme conditions. As a result of data analysis and numerical simulations, we conclude that, at the least, mode-2 internal waves were trapped around the islands. Further observational study is needed to verify the nonlinearity of mode-2 internal waves and possible trapped mode-1 waves.

We further studied the possible generation mechanism of nonlinear internal waves around the island topography in stratified shear flow. The forcing effect of shear flow and topography on the internal waves was examined, respectively, with two configurations. Configuration (1) was linearly sheared flow past a circular cylinder, and configuration (2) was vertically uniform flow past Gaussian bell topography. Both of the results showed a resonant generation of nonlinear internal waves in near critical flow, and indicated that both shear flow and the island topography force the nonlinear internal wave. The case of linearly sheared flow past Gaussian bell topography showed that internal waves were less generated with the broader Gaussian bell topography. The result is inconsistent to the ones with realistic numerical simulation where trapped internal wave often appears around the Miyake Island whose topography is broader than Mikura Island. The discrepancy indicated that actual topography around Miyake Island was important for the background flow to create critical situation. It is also suggested that background shear effect was important for nonlinear internal wave generation around the Mikura Island.

[References]

[1] Alpers, W. (1985). Theory of radar imaging of internal waves. Nature, 314(6008), 245-247.

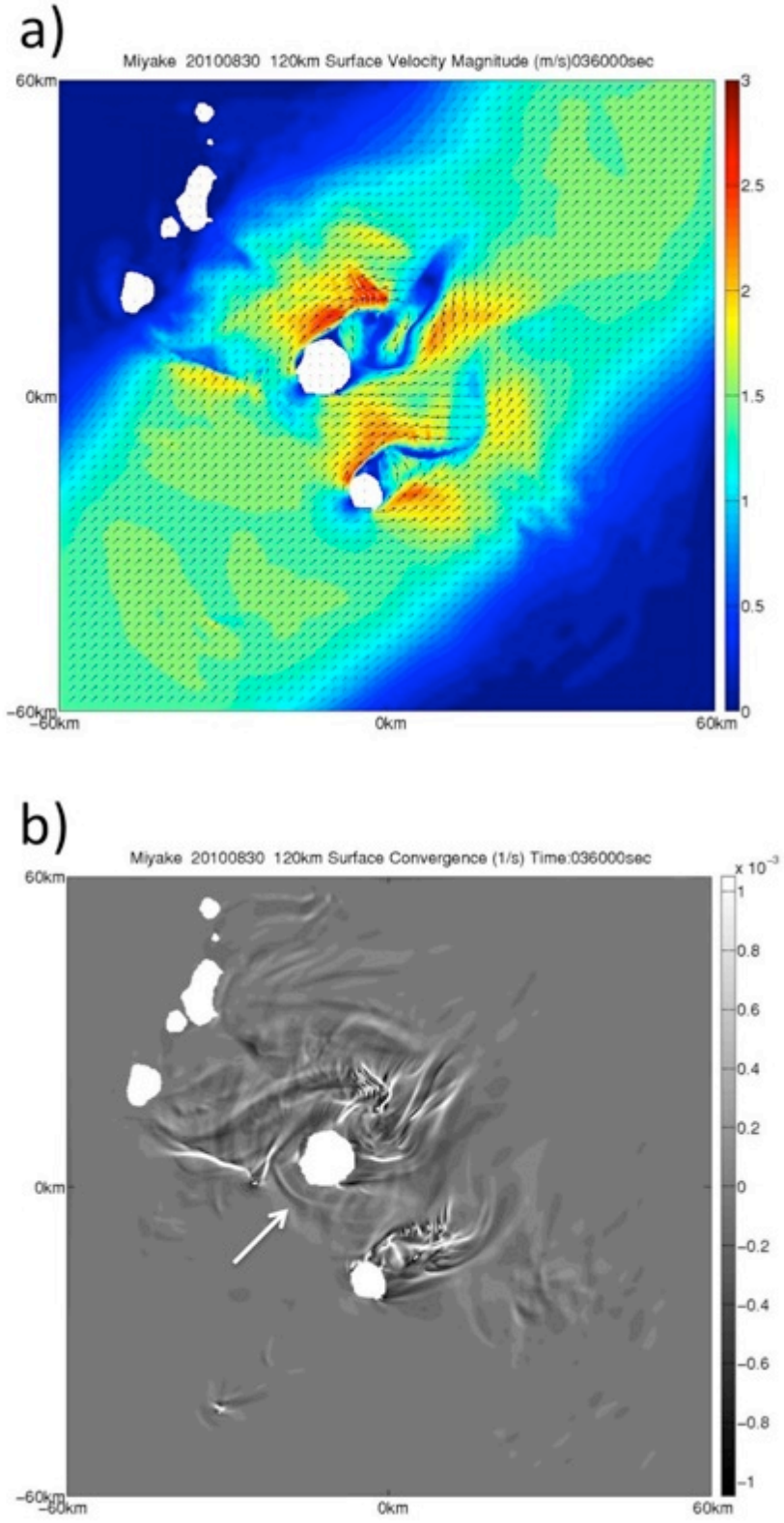

Fig.2 a) Surface flow field and b) surface velocity convergence field 10 hours after the numerical simulation for 30th in August 2010. The white allow indicates the parabola pattern created by a mode-2 internal wave.

Table of Contents

List of Figures

List of Tables

Chapter 1 Introduction

1.1 Synthetic Aperture Radar and Internal Solitary Waves

Ocean remote sensing has provided a great amount of information. Particularly, sea surface height (SSH) and sea surface temperature (SST) information have strongly contributed to studies and operational data assimilation. In contrast to sensors using visible or infrared electromagnetic waves, microwave sensors are independent of weather because the wavelength is much larger than cloud droplets. Synthetic aperture radar (SAR) is classified as an active microwave sensor. Basically, microwave sensors do not have fine resolution. For example, QuikSCAT continuously provided wind speed and direction of 10 meters above the sea surface for 10 years since 1999. The QuickSCAT had swath of 1800km, but the spatial resolution was 25 km. This coarse resolution is inevitable for microwave sensor because of the dimension of aperture attached to satellite. However, for an active microwave sensor, a technique has been developed to improve the resolution at surface to less than 100m. We shortly introduce the SAR measurement technique following the description in Jackson et al (2004).

To collect the backscattering from the surface, a microwave sensor is attached to emit signal obliquely to the surface. Since the sensor has a broad beam width, a particular area has been targeted for a period by continuous emission of the microwave. The period is usually from several seconds to tens of seconds. The obtained series of data is transformed to a synthetic image with fine resolution as if the radar aperture has a dimension of orbit path length. The obtained image through the synthesis is called a synthetic aperture radar (SAR) image.

The first space-borne SAR was equipped to the US satellite Seasat in 1978. After that, Soviet Union, European Space Agency, Japan and Canada engaged in SAR missions from 1978 to 2003 (Liu and Wu, 2001). The radar wavelength for each SAR was determined upon its objective. Some frequently used radar wavelengths are: 3.1cm for X-band, 5.66cm for C-band, 10.0cm for S band, and 23.5cm for L-band. For the ocean measurement, waves of a particular wavelength λ_w reflect the radar signal with wavelength of λ_r defined by (1.1) because of the Bragg scattering

$$\lambda_w = \lambda_r / 2\sin\theta \tag{1.1}$$

where θ is the radar incident angle (~18°to 50°). Therefore, windwaves of several centimeters to a meter create a significant influence on SAR image.

Wind waves are triggered by wind, but it is also modulated by oceanic flow. One of the unexpected but important finding from the American Seasat satellite was detectability of underwater topography by SAR (Alpers et al, 1984). Although the radar signal cannot penetrate into subsurface, the underwater topography changes the oceanic flow and the flow modulates wind wave fields, which mainly influence the backscattering distribution that SAR measures. As well as the topography, long surface waves are also known to modulate the backscattering by modulating short wind wave (Jackson et al, 2004), but here we focus on the modulation because of internal waves, particularly because of internal solitary waves. In this

study, we normally use the term "internal waves" for long internal waves whose wavelength is longer than water depth and use the term "nonlinear internal waves" for large amplitude internal waves.

Internal solitary wave is one of the nonlinear internal waves and has a single humped shape. An example of the observed solitary wave is shown in Figure 1.1. The mathematical formulation is introduced in next subsection and we describe internal solitary waves qualitatively in this section. Since internal solitary waves create horizontal velocity convergence and divergence zone, internal solitary wave is detected by SAR imagery. An example of the internal solitary wave detected by SAR image is shown in Figure 1.2. The image captures the northeastern South China Sea where the nonlinear internal waves are generated rigorously. The white line with length of more than 200km corresponds to the convergence zone created by the nonlinear internal wave.

According to Alpers (1985), modulation of backscattering intensity and wind waves by internal waves are formulated by (1.2).

$$\frac{\delta\sigma}{\sigma_0} = \frac{\delta E}{E_0} = -(4+\gamma)\tau_r \frac{\partial U}{\partial x} \tag{1.2}$$

where $\delta\sigma = \sigma - \sigma_0$ is deviation of normalized radar backscattering cross-section, σ, from its mean value σ_0, δE is as well deviation of the spectral energy density of wind waves from its mean value E_0, γ is ratio between group and phase velocity of wind waves ($\gamma = 0.5$) and U is sea surface current velocity induced by internal waves. The equation (1.2) describes that modulation of backscattering intensity σ depends on relaxation time τ_r and the strain rate of the sub-surface flow. Relaxation time τ_r physically means a time for wave system to respond the velocity strain $\partial U/\partial x$ and is of the order of 10-100 wave periods (Alpers and Hennings, 1984).

The equation (1.2) considers one-dimensional space. For two dimensional wave and wind field , the modulation of backscattering depends on the combination of the directions for wind wave propagation and velocity shear. If they are normal, the modulation does not happen according to this theory. Further description on the formulation of (1.2) is found in Alpers (1984). A schematic diagram explains the relation between nonlinear internal wave, wind wave and radar intensity (Figure 1.3).

Nonlinear internal waves are observed in shallow coastal area all over the world. The comprehensive report about the nonlinear internal wave manifestations can be found in “An atlas of internal solitary-like waves and their properties” (Jackson, 2004). The locations of detected internal solitary waves are summarized in the atlas in (Figure 1.4).

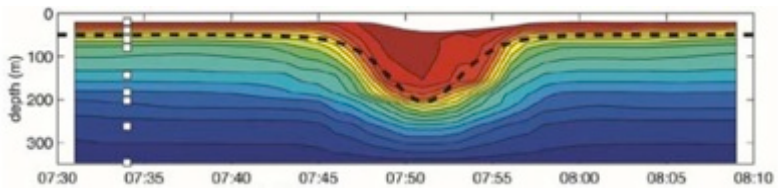

Figure 1.1 An internal solitary wave observed in northern South China Sea at the water depth of 350m (Fig. 5. in Duda et al, 2004). The black dashed lines show wave profile from weakly nonlinear theory and the contour intervals are 1℃, ranging from 11–12℃ to 28℃ .

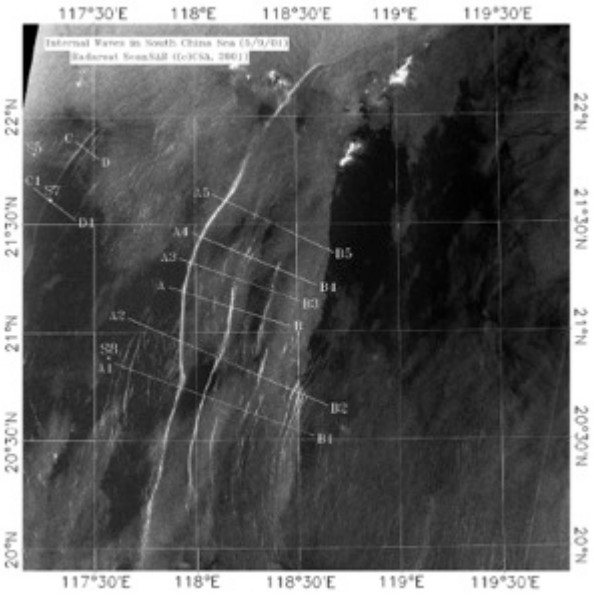

Figure 1.2 RADARSAT ScanSAR image collected northeast of the South China Sea (Fig. 3. in Liu et al, 2004).

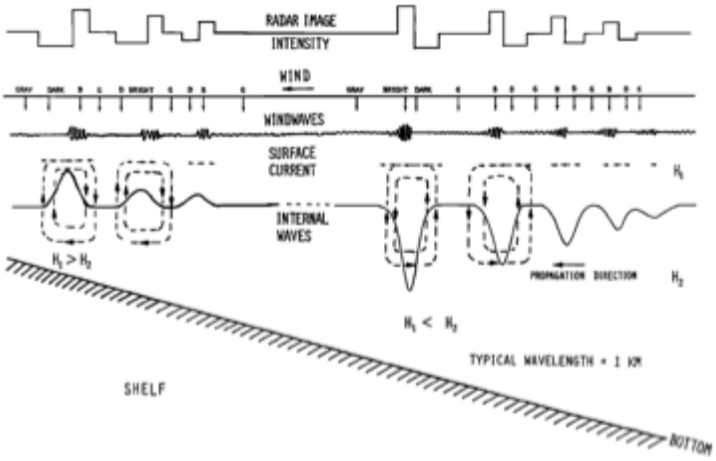

Figure 1.3 Schematic diagram for the relation between nonlinear internal wave, wind wave and radar intensity (Fig. 5. in Liu et al, 1998).

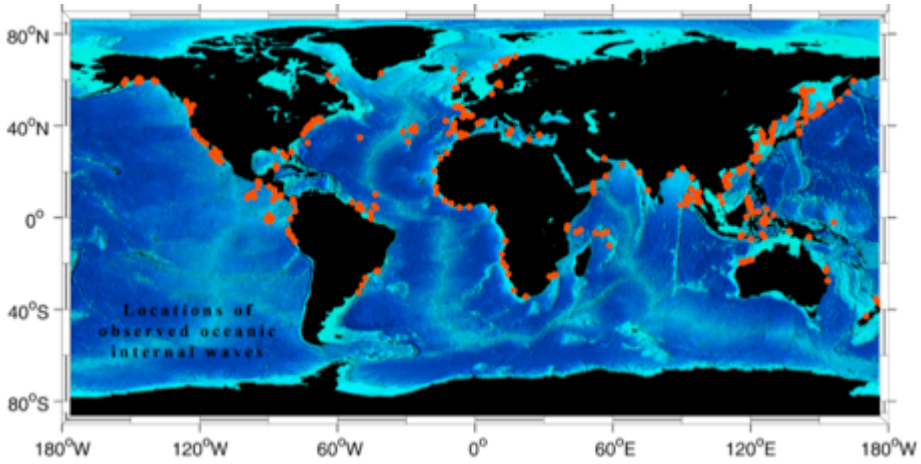

Figure 1.4 Locations of observed oceanic internal waves all over the world (Fig. 5. in Jackson and Apel, 2004).

1.2 Parabola Patterns around the Izu-Islands in Kuroshio appeared in SAR Image

The Phased-Array L-band Synthetic Aperture Radar (PALSAR) was equipped on the Advanced Land Observing Satellite (ALOS). The PALSAR detected an interesting image on 12th of June in 2006 (Figure 1.5, top). There are clear parabola patterns off the islands. One week later, SST distribution (Figure 1.5, bottom) was captured and shows the Kuroshio had approached those islands. Even though there was a week difference between both measurements, the patterns in the SAR image imply that the Kuroshio created a surface velocity field with a parabola signature.

The parabolic line reminds us a detached shock wave around obstacle in the supercritical compressible flow. In this case, the waves are not acoustic waves but an internal waves because the phase speed is comparable to the background oceanic current, the Kuroshio. The SAR image is only a snapshot and we cannot conclude whether those parabolic line patterns were steady or not. However, the idea is plausible However, we speculate that near supercritical flow, the Kuroshio, generated large amplitude internal waves and trapped them around the islands with a greater advection speed than internal waves' phase speed.
Compared to the well-known internal solitary wave generated by tidal flow in straits such as Gibraltar (Brandt et al, 1996), Luzon strait (Lien et al, 2005), Andaman Sea (Osborne and Burch 1980) and Knight Inlet (Farmer and Armi, 1999), the internal waves off the islands were generated by stable current, the Kuroshio. In addition, topography is not sill but island that should make the generated wave three-dimensional. These points distinguish the internal solitary wave generated around the island in the Kuroshio from the typical two-dimensional ones.

While the SAR has potential to provide a good amount of oceanic information, the images should be carefully interpreted because the images manifest not only oceanic condition but also atmospheric condition (Alpers and Huang, 2011). This discrimination is not easy but once a relation between the SAR image and the oceanic phenomena is revealed, we can utilize the SAR image to estimate the oceanic condition as scientists immediately recognize internal solitary wave generation around straits described above. Despite its potential, few studies have made use of SAR images for studying the Kuroshio except for the study on vortex train in the lee side of Izu-Islands by Isoguchi et al (2010).

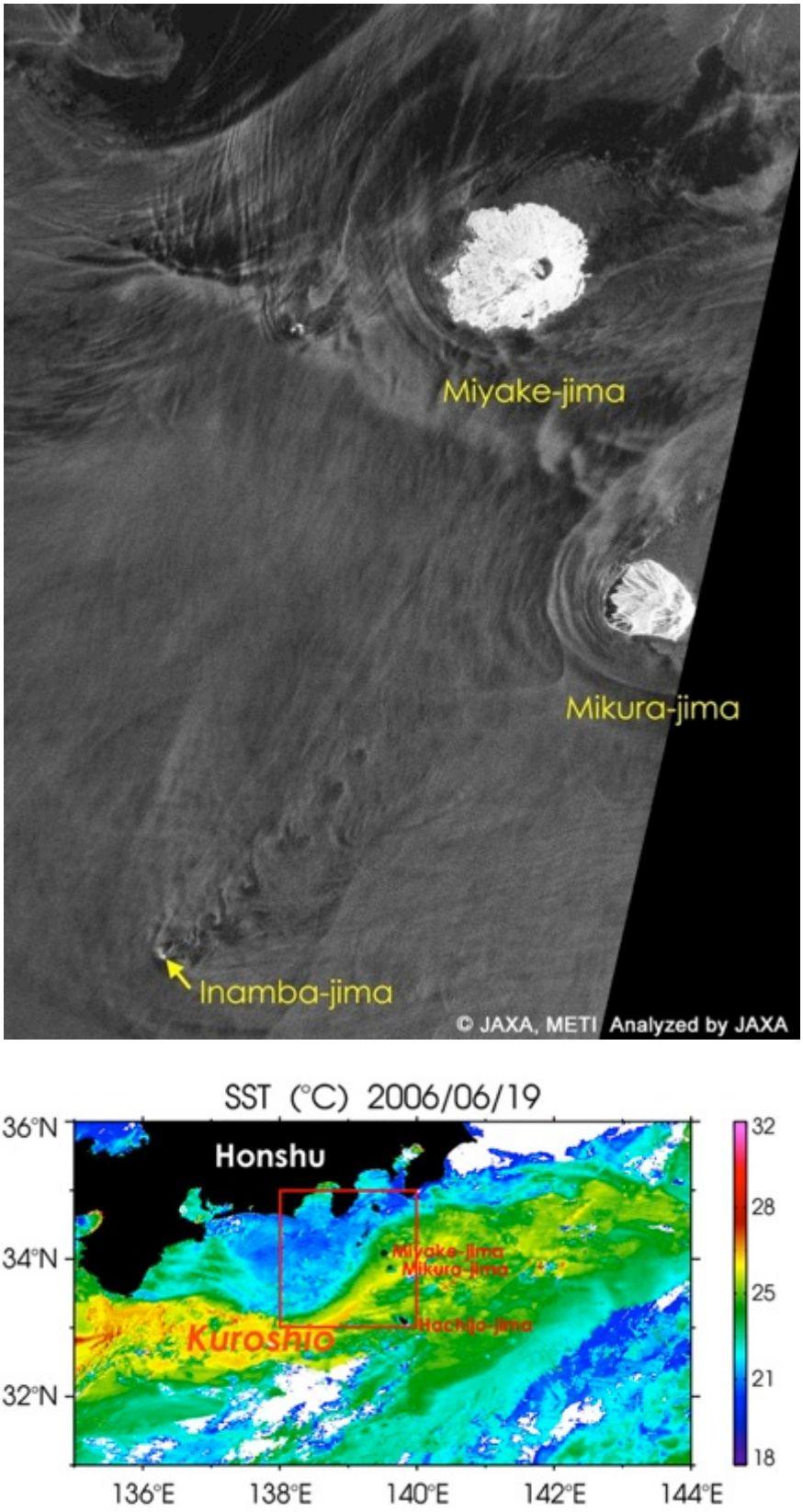

Figure 1.5　A SAR image (top) captured by PALSAR and SST field captured by MODIS (bottom) for 19/Jun/2006 and 12/Jun/2006 respectively. Courtesy of JAXA/METI. (source:http://www.eorc.jaxa.jp/ALOS/img_up/jpal_karman.htm).

1.3 The Izu-ridge and the Izu-Islands

The Miyake and Mikura Islands shown in Figure 1.5 locate at northern part of the Izu-ridge. The Izu-ridge has attracted an amount of attention from physical oceanographers because of its importance for Kuroshio and internal tide generation. Kuroshio is known to have bimodal path south Japan and paths are called the large-meander (LM) path and the non-large-meander (NLM) path as shown in Figure 1.6 (Usui et al., 2013). The NLM path is sometimes further classified to the offshore-NLM (oNLM) and the nearshore-NLM (nNLM) (Kawabe 1995). Izu-ridge with its topography is considered to have close relation with Kuroshio's pathway. Relatively deep region around 34°N is regarded as northern gate, while the region around 32°N- 33°N is regarded as southern gate for Kuroshio to enter the pacific basin.

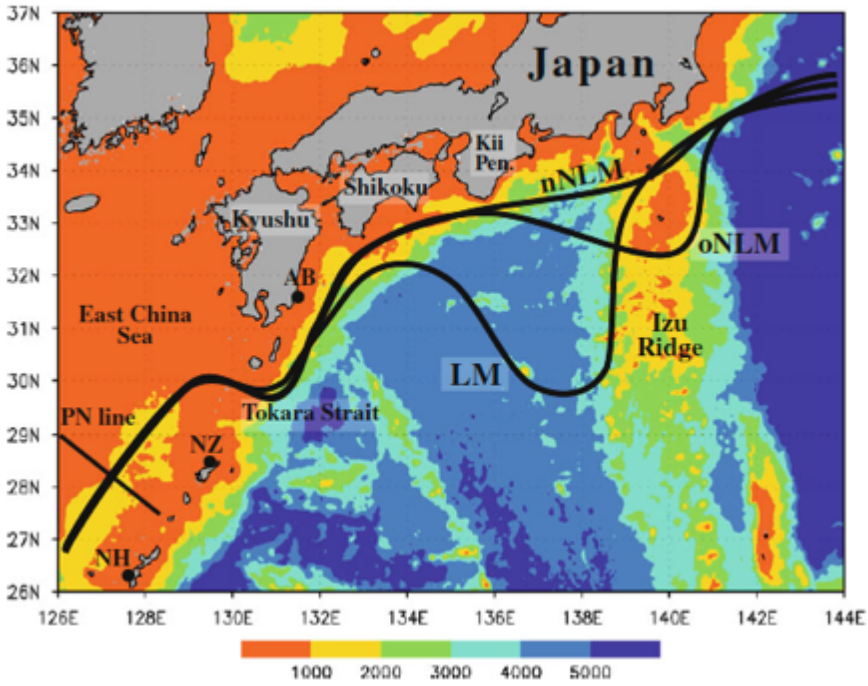

Figure 1.6 Sea bottom bathymetry (m) and three typical stable paths of the Kuroshio south of Japan: the large meander (LM) path, the offshore non-large meander (oNLM) path, and the nearshore non-large meander (nNLM) path (Fig. 1. in Usui et al 2013).

The idea of the gates simplifies the Izu-ridge topography as islands with wall and has provided progress in understanding of the Kuroshio dynamics (Mitsudera et al, 2006). An effect of the sloping bottom topography on the Kuroshio's large meander was further considered by Mitsudera et al. (2006). It was shown that baroclinicity in the Kuroshio flow and the sloping bottom topography is important for blocking and amplification of the large meander. On the other hand, Izu-Ogasawara ridge was clarified to be an energetic internal tide generation region as a result of three-dimensional numerical simulation (Niwa and Hibiya, 2002). The generated internal tides are thought to transfer the energy to small mixing scale through the nonlinear interaction with the background internal wave field. The

mixing is quite important for studies considering long time-scale, such as climate change, because the mixing determines the typical state of the ocean.

While an amount of attention was paid to the Izu-ridge, flow field around Izu-islands has not been studied intensively. Izu-Islands locate on the northern part of Izu-ridge and the northern gate is located near the Miyake and Mikura Islands. The complex topography of the island chain has been simplified or dismissed in the previous studies. However, the recent improvement of computation resources now enables numerical simulation with smaller spatial resolution. It is thought that the complex topography of the island should be included in the numerical ocean model to understand the dynamics of the Kuroshio and other physical oceanic processes, including internal tides, more accurately.

In addition to the scientific context, the velocity field around the Izu-islands in Kuroshio has attracted attention in the context of ocean renewable energy. The Miyake Island is known to be one of the prospective sites for an ocean current power generation system (Kodaira et al, 2013). To improve the quality of the feasibility study for an ocean current power generation system, the use of regional ocean models and in situ observation are encouraged. There are several difficulties in reproducing flow fields around the Izu-island accurately. An important but difficult point is the validation of the numerical simulation result. Point observations can provide the high-resolution data for time, but the spatial distribution of the ocean state cannot be obtained. Sea surface height information from satellites provides the surface velocity distribution with geostrophic approximation but it cannot be used for the flow field around the Izu-islands in the Kuroshio because the Rossby number is at most order unity and the measurement frequency should be too long for the coastal flow around the islands.

The other problem is more practical. Numerical ocean models often apply the hydrostatic approximation to the governing equation. The application helps the computation to be completed in a short time, but it neglects the dynamics related to the wave dispersion such as internal solitary wave trains. The wave dispersion becomes more important as the spatial scale of the phenomena becomes smaller. These two points make the numerical simulation with high-resolution around the island very challenging.

1.4 Objective

Examining the multiple parabolic lines which appeared in SAR images off the Izu-Islands posed special dynamical and numerical challenges. These parabolic lines may have implied the presence of three-dimensional nonlinear internal waves excited by the Kuroshio current.

Under a critical condition, disturbances cannot freely propagate upstream of an island, and a shock forms if there is no wave dispersion. However, the long internal wave was weakly dispersive, and the wave shape depends on a balance between the nonlinearity and the wave dispersion. From the SAR imagery, we can speculate that both effects were relevant. The nonlinear effect accentuates the parabolic pattern in the SAR image by inducing a strong surface convergence or divergence at the ocean surface, while the dispersive effect diffuses the shock into a wave-like pattern. Since the Kuroshio current speed changed sharply around the islands, several modes may have become critical simultaneously. Additionally, the critical condition might depend on not only the Kuroshio current but also the tidal current. These outstanding dynamical questions remain unchallenged. In particular, the three-dimensional nonlinear internal waves generated by the Kuroshio current's interaction with islands has not been studied numerically, even with the simplified topographic settings.

In consideration of the numerous dynamical processes hypothesized earlier, a non-hydrostatic simulation ought to be conducted. If indeed the SAR image of the Izu-Islands represents a manifestation of oceanic internal waves, it means that the SAR images can provide information on small-scale oceanic processes around the islands excited by the Kuroshio. The information is quite useful from an operational oceanographic point of view, and is quite interesting as for basic oceanography and fluid mechanics as well.

This study aims to clarify the nature of three-dimensional nonlinear internal wave generation around the islands, within the influence of the Kuroshio, and to better understand the dynamics involved. Data analysis and non-hydrostatic numerical simulations were conducted to support these ideas. The situation is highly complex with a continuously stratified shear flow (the Kuroshio) and complex topography around the islands. Therefore, as a supplement we conduct numerical simulations with simplified settings. These simplified settings help to obtain a better understanding of the three-dimensional nonlinear internal wave generation around the islands.

1.5 Overview

This thesis is mainly concerned with generation of nonlinear internal waves around the islands in the Kuroshio. The contents could be divided into two parts described as follows.

The first part focuses on the possible nonlinear internal wave generation around the Izu-Islands in Kuroshio. The goal is to clarify that nonlinear internal waves are manifested in SAR images as the parabola patterns around the island in the Kuroshio. Although the Kuroshio shown in SST image (Figure 1.5, bottom) convincingly shows that the SAR image (Figure 1.5, top) is mainly influenced by oceanic phenomena around the islands in the Kuroshio, a consideration is needed to discriminate the effect of oceanic surface current and atmospheric wind on SAR image as mentioned by Alpers and Huang (2011). Therefore, we first investigate the environmental condition when the parabola patterns were detected by PALSAR to demonstrate that those patterns are mainly dependent on the Kuroshio. Next, we conduct numerical simulation to reproduce the flow field including internal waves.

The second part concerns a basic nature of the three-dimensional nonlinear internal waves generated around island topography. We conduct numerical simulation with isolated island topography such as circular cylinder and Gaussian bell to obtain better understandings of the flow field around the islands in the Kuroshio. The situation is similar to previous studies concerned with atmospheric flow around mountain. However, our topography is island and the flow only passes around the topography, while atmospheric flow possibly goes over the mountain. This means that a stagnation point inevitably appears in front of the island topography and background velocity reduces from the far upstream value to zero. Under the long wave approximation, internal long waves have propagation speeds discretely. Therefore, several modes may be trapped around the obstacle.

This thesis is composed of the following sections. In chapter 2, fundamental theories for the nonlinear internal wave are described. In chapter 3, we investigate under what condition SAR images with parabola patterns were obtained. In chapter 4, numerical simulations of the stratified shear flow over the Izu-Islands topography is conducted to clarify that oceanic internal waves are responsible for the parabola signature appearing in the SAR images. Three-dimensional stratified shear flow over the isolated topography is examined in chapter 5 to support the results from chapter 4.

Chapter 2 Theoretical Background

A finite but small amplitude solitary wave is generally described by weakly nonlinear KdV theory. We introduce formulations of the KdV solitary wave for one, two and continuously stratified fluids in the following sections, but mainly focus on the continuously stratified case.

2.1 Solitary Wave in One-Layer Fluid

An infinitesimal fluid motion with long horizontal length scale in one layer is approximated to linear shallow water equation.

$$\frac{\partial \eta}{\partial t} + c_o \frac{\partial \eta}{\partial x} = 0 \tag{2.1}$$

$$c_o = \sqrt{g d_o} \tag{2.2}$$

where $\eta_{(x,t)}$ is wave shape, d_o is reference water depth, c_o is phase speed for linear long wave and g is gravity acceleration coefficient. In this formula, every wave has same phase speed. However, finite amplitude wave violates the linear approximation and also long wave approximation is not justified when the wavelength is not much larger than water depth d_o. When the both of the effects are comparable but weak, the wave follows weakly nonlinear KdV equation (2.3) that includes both of the weak nonlinearity and weak dispersion (Baines, 1998).

$$\frac{\partial \eta}{\partial t} + c_o \frac{\partial \eta}{\partial x} + c_o \frac{3}{2} \frac{\eta}{d_o} \frac{\partial \eta}{\partial x} + \frac{1}{6} c_o {d_o}^2 \frac{\partial^3 \eta}{\partial x^3} = 0 \tag{2.3}$$

The KdV equation is well known because it has analytical solutions for solitary wave and cnoidal waves. A formal derivation of (2.3) is described in Whitham (1984) with multiple asymptotic expansion with two small parameters $\alpha = a/d_o$ and $\beta = (d_o/l)^2$ with $\beta = O(\alpha)$ where a is wave amplitude and the l is horizontal scale of motion. The first two terms in (2.3) consist linear long wave equation. We describe below the physical interpretation of the third and fourth terms in (2.3).

We first focus on the nonlinearity that is neglected by linear wave equation. Nonlinear shallow water equations for one layer is described as follows

$$\frac{\partial u}{\partial t} + u \frac{\partial u}{\partial x} + g \frac{\partial \eta}{\partial x} = 0 \tag{2.4}$$

$$\frac{\partial d}{\partial t} + \frac{\partial (du)}{\partial x} = 0 \tag{2.5}$$

Where $d = d_o + \eta$ is total water height. In these nonlinear shallow water equations, waves moving to the right into still water of depth d_o satisfy the Riemann invariant (Whitham, 1984)

$$u = 2\sqrt{g(d_o + \eta)} - 2\sqrt{g d_o} \tag{2.6}$$

By removing u in the equations (2.4)-(2.6), following equation is obtained.

$$\frac{\partial \eta}{\partial t} + c_o \left(1 + \frac{3}{2} \frac{\eta}{d_o}\right) \frac{\partial \eta}{\partial x} = 0 \tag{2.7}$$

It became clear that the third term in (2.3) originates from nonlinearity and describes that finite amplitude increases the phase speed.

We have focused on the horizontally long wave motion, so the phase speed of the wave can be approximated to c_o, but a modification is needed if the wave is not so long and weak dispersion should be included. Linear dispersion relation for the wave in arbitrary depth d_o is described as follows.

$$\omega^2 = gk \tanh(kd_o) \tag{2.8}$$

Expanding this dispersion relation in powers of $kd_o(\ll 1)$ to the first order gives,

$$\omega^2 = {c_o}^2 k^2 (1 - k^2 d_o^2/3) \tag{2.9}$$

and the one direction form of (2.9) is given as follows.

$$\omega = c_o k (1 - k^2 d_o^2/6) \tag{2.10}$$

Waves of the form $\exp(ikx - i\omega t)$ satisfies (2.10) also satisfies the following equation.

$$\frac{\partial \eta}{\partial t} + c_o \frac{\partial \eta}{\partial x} + \frac{1}{6} c_o {d_o}^2 \frac{\partial^3 \eta}{\partial x^3} = 0 = 0 \tag{2.11}$$

Again, we can clearly see that the third term in (2.11) corresponds to the fourth term in (2.3) that stands for the wave dispersion. Compared to the nonlinearity, wave dispersion decreases the phase speed and the magnitude depends on the value of kd_o.

The formulation of the nonlinearity and the dispersion described above are included in the KdV equation (2.3). The third term in (2.3) stands for the effect of nonlinearity that increases the phase speed thus making the wave steeper, while the fourth term in (2.3) stands for the wave dispersion that decreases the phase speed thus making the wave flatten. The numerical integration of the KdV equation was compared with nonlinear shallow water equation by Peregrine (1966). The initial condition is gentle transition between uniform flow and still water and the time integration of nonlinear shallow water equation showed finite amplitude wave becomes steeper and steeper because dispersion term is absent. Finally, the wave slope became vertical. The discontinuous section is called hydraulic jump and it is mathematically described as a formation of shock. On the other hand, results of numerical integration for KdV equation showed development of an undular bore as shown in Figure 2.1.

The first two terms in the KdV equation (2.3) consist linear non-dispersive equation and the solution is sinusoidal wave. The additional two terms for nonlinearity and dispersion cancels out each other and have new solution. One of analytical solutions is the so called KdV solitary wave described as follows with only two parameters, amplitude a and reference water depth d_o.

$$\eta = a \operatorname{sech}^2 \left[\left(\frac{3a}{4h_o} \right)^{1/2} \left(\frac{x - ct}{d_o} \right) \right] \tag{2.12}$$

$$c = c_o \left(1 + \frac{a}{2d_o} \right) \tag{2.13}$$

A wave with single humped shape is often seen in the shallow water and can be described by (2.12). Terms in the bracket in (2.12) except for $(x - ct)$ are regarded as the inverse of a length scale. When the amplitude a becomes larger, the wavelength becomes shorter, so the wave shape narrows. The phase speed c also depends on the amplitude as we can see from (2.13), so the finite amplitude effect makes wave faster and narrower.

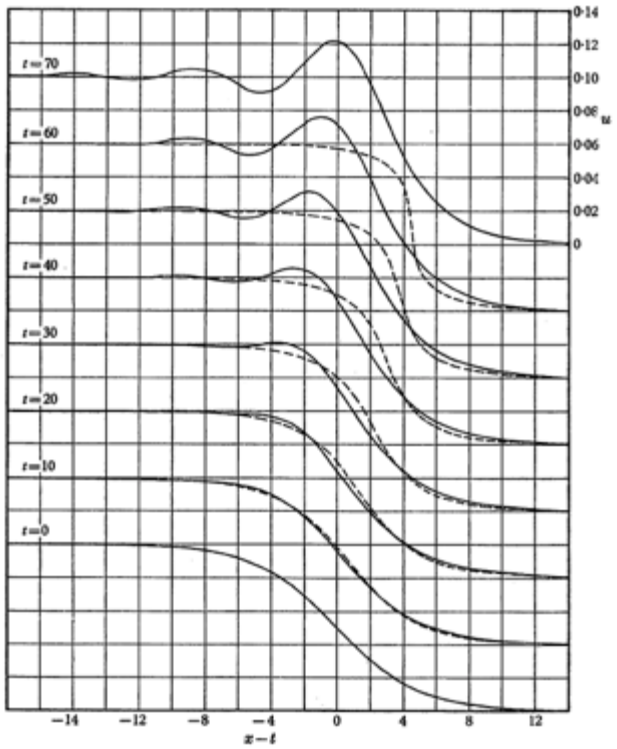

Figure 2.1 Initial growth of an undular bore as solutions of KdV equation (solid line) and development of hydraulic jump as a solution to the nonlinear shallow water equation (dashed line) (Fig. 4. in Peregrine 1966).

2.2 Solitary Wave in Two-Layer Fluid

Two-layer configuration is sometimes used as a simple model of the ocean: the upper and bottom layer is separated by thermocline and compose a two-layer configuration. Since the two-layer configuration has not one but two vertical length scales, intrinsic scale h and total depth H, there are several theories for internal solitary wave. According to Koop and Butler (1981), nonlinear internal wave studies with two-layer configuration can be categorized as follows.

(a) Shallow-water theory (Benjamin. 1966): $l/H \ll 1,\ h/H = O(1)$

(b) Deep-water theory (Benjamin. 1967, Ono, 1975): $l/H \to 0,\ l/h \ll 1,.$

(c) Finite-depth theory (Kubota et al., 1978): $l/h \gg 1,\ h/H \ll 1$

We here focus on the shallow water theory since we focus on shallow water configuration and because the shallow water theory is powerful thus widely used by the previous studies of internal solitary waves. There are weakly nonlinear KdV theory and fully nonlinear theory for two layer fluid system and they are consistently described in Choi and Camassa (1999). It has been known that weakly nonlinear KdV theory is insufficient to describe the large amplitude internal solitary waves observed in the ocean, so higher order weakly nonlinear theory and fully nonlinear theories have been suggested and studied. We here shortly introduce the formulation of the model equation for internal solitary waves described in Choi and Camassa (1999).

Incompressible and inviscid fluid with density ρ_i is considered and the governing

equations are continuity equation and Euler equations,

$$u_{ix} + w_{iz} = 0 \tag{2.14}$$

$$u_{it} + u_i u_{ix} + w_i u_{iz} = -p_{ix}/\rho_i \tag{2.15}$$

$$w_{it} + u_i w_{ix} + w_i w_{iz} = -p_{ix}/\rho_i - g \tag{2.16}$$

where subscripts with respect to space and time represents partial differentiation, while the i stands for the each layer. The situation concerned is two-fluids system (Figure 2.2) and $i = 1$ ($i = 2$) stands for upper layer (lower layer). The configuration is stably stratified two-fluids system ($\rho_1 < \rho_2$) with ligid surface for both of top and bottom boundaries, so the boundary conditions are given by

$$w_{(x,h_1,t)} = 0 \qquad w_{(x,-h_2,t)} = 0 \tag{2.17}$$

, while the boundary conditions for the interface are given by

$$\zeta_t + u_1\zeta_x = w_1\,, \quad \zeta_t + u_2\zeta_x = w_2\,, \quad p_1 = p_2 \;\; at \;\; z = \zeta(x,t) \tag{2.18}$$

, which stands for the continuity of pressure and normal velocity.

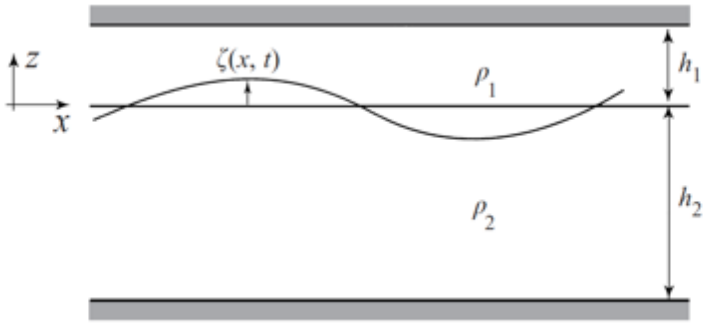

Figure 2.2 Two-fluid system with rigid lid (Figure.1 in Choi and Camassa, 1999)

Choi and Camassa (1999) derived a fully nonlinear model equation known as the MCC (Miyata-Choi-Camassa) equation. To derive the MCC equation, only the long wave approximation was used and the small amplitude approximation was not used. The disuse of the small amplitude approximation is the reason the MCC equation is a fully nonlinear model. The long wave approximation means there exists the following scaling relation between each component of velocity.

$$\frac{w_i}{u_i} = O\left(\frac{h_i}{L}\right) = O(\varepsilon) \ll 1 \tag{2.19}$$

where L is typical wave length. The other assumption for the amplitude is given by

$$\frac{u_i}{U_o} = O\left(\frac{\zeta}{h_i}\right) = O(1) \tag{2.20}$$

where U_o is characteristic speed chosen to be $U_o = (gh_1)^{1/2}$. With these assumptions, Choi and Camassa (1999) showed next evolution equations in dimensional form governing four unknown variables; interfacial displacement ζ, layer mean velocities $\overline{u_1}, \overline{u_2}$ and pressure at the interface P.

$$\eta_{1t} + (\eta_1\overline{u_1})_x = 0\,, \quad \eta_1 = h_1 - \zeta \tag{2.21}$$

$$\eta_{2t} + (\eta_2\overline{u_2})_x = 0\,, \quad \eta_2 = h_2 + \zeta \tag{2.22}$$

$$\overline{u_1}_t + \overline{u_1 u_1}_x + g\zeta_x = -\frac{P_x}{\rho_1} + \frac{1}{\eta_1}\left(\frac{1}{3}{\eta_1}^3 G_1\right)_x + O(\epsilon^4) \tag{2.23}$$

$$\overline{u_2}_t + \overline{u_2 u_2}_x + g\zeta_x = -\frac{P_x}{\rho_2} + \frac{1}{\eta_2}\left(\frac{1}{3}{\eta_2}^3 G_2\right)_x + O(\epsilon^4) \tag{2.24}$$

where G_1, G_2 is described with $\overline{u_1}$ and $\overline{u_2}$, respectively. From the evolution equations (2.21)-(2.24), fully nonlinear model (MCC equation) for a wave of permanent form moving with speed c is obtained and is implicitly given by

$$(\zeta_x)^2 = \left[\frac{3g(\rho_2 - \rho_1)}{c^2(\rho_1 h_1^2 - \rho_2 h_2^2)}\right]\frac{\zeta^2(\zeta - a_-)(\zeta - a_+)}{(\zeta - a_*)} \tag{2.25}$$

where

$$a_* = -\frac{h_1 h_2(\rho_1 h_1 + \rho_2 h_2)}{\rho_1 h_1^2 - \rho_2 h_2^2} \tag{2.26}$$

and $a_\pm$ are the roots of quadratic equation

$$\zeta^2 + \left(-\frac{c^2}{g} - h_1 + h_2\right)\zeta + h_1 h_2\left(\frac{c^2}{c_o^2} - 1\right) = 0 \tag{2.27}$$

The propagating speed c is written interms of the wave amplitude a as

$$\frac{c^2}{c_o^2} = \frac{(h_1 - a)(h_2 + a)}{h_1 h_2 - (c^2/g)a} \tag{2.28}$$

Once the amplitude of the internal wave is determined, the wave shape is obtained by numerically solving the (2.25). A validation of the fully nonlinear theory was conducted by Camassa, et al. (2006) through the comparison between both of the numerical solution of the Euler equation and laboratory experiments. The results showed that the solutions of the MCC equation match fairly well with experimental results even the wave amplitude was order unity. Figure 2.3 shows a comparison between the solutions of MCC, Euler equation and KdV solutions, and suggests that fully nonlinear solution deviates from the weakly nonlinear KdV solution.

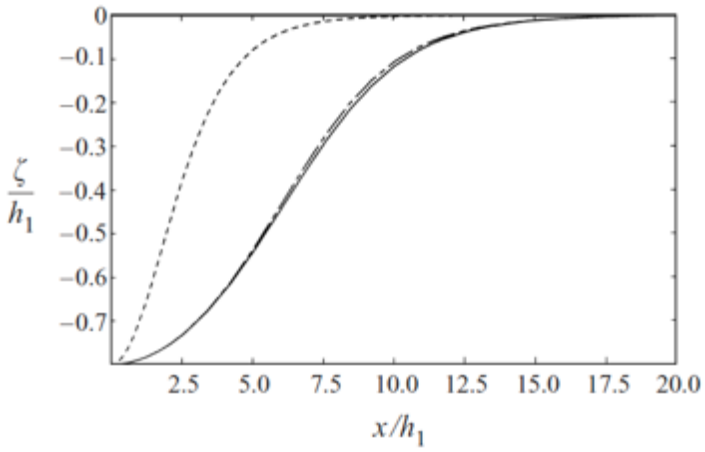

Figure 2.3 A comparison of solitary wave solution for $\rho_1/\rho_2 = 0.997$, $h_2/h_1 = 3$ and $a/h_1 = -0.8$. The solid line is the solution of MCC equation which is almost the same as the solution of Euler equation (— · —) and the KdV solitary waves (---) is much narrower than the others (Figure.6 in Choi and Camassa, 1999).

Weakly nonlinear KdV type theory was also obtained by applying another scaling given as

$$\frac{u_i}{U_o} = O\left(\frac{\zeta}{h_i}\right) = O(\varepsilon^2) \tag{2.29}$$

The obtained KdV equation for internal wave in two fluids is described as follows.

$$\zeta_t + c_o\zeta_x + c_1\zeta\zeta_x + c_2\zeta_{xxx} = 0 \tag{2.30}$$

$$c_o^2 = \frac{gh_1h_2(\rho_2 - \rho_1)}{\rho_1h_2 + \rho_2h_1}, \quad c_1 = -\frac{3}{2}c_o\frac{\rho_1h_2^2 - \rho_2h_1^2}{\rho_1h_1h_2^2 + \rho_2h_1^2h_2}, \quad c_2 = \frac{c_o}{6}\frac{\rho_1h_1^2h_2 + \rho_2h_1h_2^2}{\rho_1h_2 + \rho_2h_1} \tag{2.31}$$

The solitary wave solution is given by

$$\zeta_{KdV}(x - ct) = a\,\mathrm{sech}^2\left[\frac{x - ct}{L_{KdV}}\right] \tag{2.32}$$

with

$$L_{KdV}{}^2 = \frac{12c_2}{ac_1}, \quad c = c_o + \frac{c_1a}{3} \tag{2.33}$$

To have the solution, $ac_1 > 0$ is needed, so the polarity of solitary wave is defined by the sign of c_1, namely, the sign of $\rho_1h_2^2 - \rho_2h_1^2$. In the ocean, there is little difference in density between upper and lower layers, so a thickness ratio of the two layers h_1/h_2 mainly defines the polarity. When the value $\rho_1h_2^2 - \rho_2h_1^2$ close to zero, an another weakly nonlinear model called modified KdV or extended KdV (eKdV) equation is needed.

According to the Helfrich and Melville(2006), extended KdV equation for a two layer system with rigid lid, no mean flow and the Boussinesq approximation is described as follows.

$$\zeta_t + c_o\zeta_x + c_1\zeta\zeta_x + c_3\zeta^2\zeta_x + c_2\zeta_{xxx} = 0 \tag{2.34}$$

where

$$c_o^2 = \frac{gh_1h_2}{h_2 + h_1}\frac{(\rho_2 - \rho_1)}{(\rho_1 + \rho_2)}, \quad c_1 = \frac{3}{2}c_o\left(\frac{h_1 - h_2}{h_1h_2}\right),$$
$$c_2 = \frac{c_o}{6}h_1h_2, \quad c_3 = \frac{3}{2}c_o\left(\frac{h_1 - h_2}{h_1h_2}\right) \tag{2.35}$$

The eKdV and MCC theories agree well for the range $0.4 < h_1/(h_1 + h_2) < 0.6$ where the scaling requirement for eKdV is satisfied. The comparison between KdV, eKdV and MCC are introduced in the Helfrich and Melville (2006). All three theories show almost same relations for wave properties as far as the wave amplitude is small (Figure 2.4). As the wave amplitude becomes larger, KdV theory deviates from the other two theories. The eKdV and MCC theories show almost same relations while the requirement of eKdV is satisfied (Figure 2.4, right). However, the difference of the two becomes large once the configuration deviates from the requirement (Figure 2.4, left).

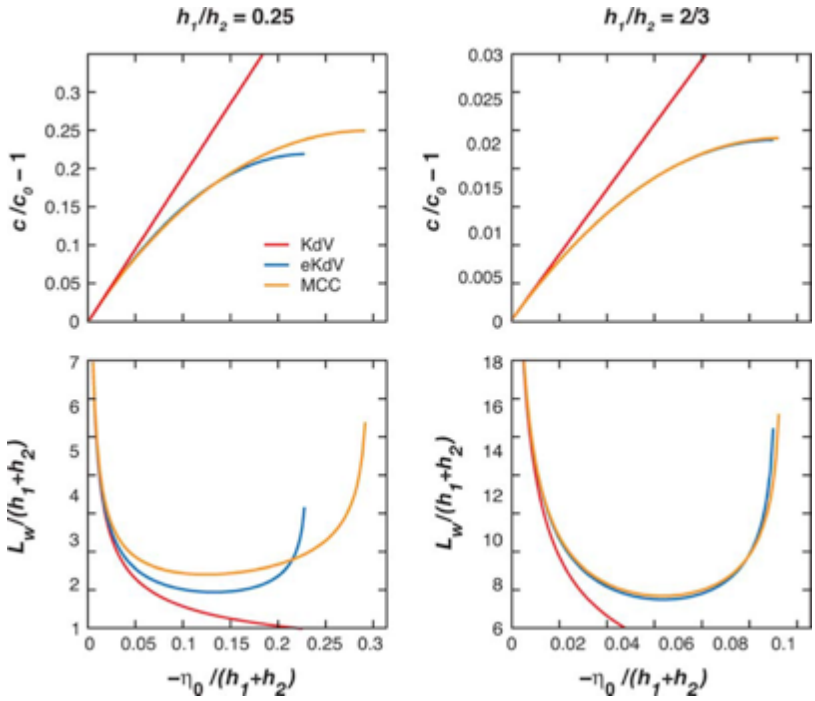

Figure 2.4 Comparison of solitary wave properties between KdV (red), eKdV (blue), and MCC. (yellow) theories. The top row shows the relation between wave speed and amplitude, while the bottom row shows the relation between wavelength and amplitude (Figure.5 in Helfrich and Melville, 2006).

2.3 Solitary Wave in Continuously Stratified Fluid

Two-layer model is useful to describe internal solitary waves, but the application is valid only for the density profile with thin thermocline. If a density profile changes gradually, a theory for the continuously stratified fluid is needed. Here we introduce a theory for continuously stratified fluid basically following the description by the Grimshaw (2001).

2.3.1 Linear Theory

We consider the basic state which has density $\rho_{o(z)}$, pressure $p_{o(z)}$ and a horizontal shear flow $u_{o(z)}$ between top $(z = \eta)$ and bottom boundary $(z = -h)$. Then, the equations of motion relative to this basic state are given by

$$\rho_o(u_t + u_o u_x + w u_{oz}) + p_x = -(\rho_o + \rho)(u u_x + w u_z) - \rho(u_t + u_o u_x + w u_{oz}) \tag{2.36}$$

$$p_z + g\rho = -(\rho_o + \rho)(w_t + u_o w_x + u w_x + w w_z) \tag{2.37}$$

$$g(\rho_t + u_o \rho_x) - \rho_o N^2 w = -g(u\rho_x + w\rho_z) \tag{2.38}$$

$$u_x + w_z = 0 \tag{2.39}$$

where $(u_{o(z)} + u, w)$ are the velocity components in the (x, z) directions, $\rho_{o(z)} + \rho$ is the density, $p_{o(z)} + p$ is the pressure and $N_{(z)}$ is bouyency frequency called Brunt-Visala frequency defined by

$$N^2 = -\frac{g}{\rho_o}\frac{\partial \rho_o}{\partial z} \tag{2.40}$$

The boundary conditions are

$$w = 0 \quad at \quad z = -h \tag{2.41}$$

$$p_o + p = 0 \quad at \quad z = \eta \tag{2.42}$$

$$\eta_t + u_o\eta_x + u\eta_x = w \quad at \quad z = \eta \tag{2.43}$$

The vertical particle displacement ζ is defined as follows as the primary dependent variable to describe the shape of internal wave.

$$\zeta_t + u_o\zeta_x + u\zeta_x + w\zeta_z = w \tag{2.44}$$

The isopycnal surfaces are then given by $z = z_o + \zeta$ and the perturbation density field is given by

$$\rho = \rho_{o(z-\zeta)} - \rho_{o(z)} \approx \rho_o g^{-1} N^2 \zeta$$

Linear long internal wave theory is obtained by neglecting the right hand side of (2.36)-(2.39) and by linearizing boundary conditions. Solutions are sought in the form of following separate variable

$$\zeta = A(x - ct)\phi(z) \tag{2.45}$$

, while the other dependent variable are then given by

$$u = A(x - ct)[(c - u_o)\phi(z)]_z \tag{2.46}$$

$$p = \rho_o(c - u_o)^2 A(x - ct)\phi_z(z) \tag{2.47}$$

$$\rho = \rho_o g^{-1} N^2 A(x - ct)\phi(z) \tag{2.48}$$

where c is the linear long wave speed, and the modal functions $\phi(z)$ are defined by the eigenvalue problem ,

$$\frac{\partial}{\partial z}\left(\rho_o(c - u_o)^2 \frac{\partial\phi(z)}{\partial z}\right) + \rho_o N^2\phi(z) = 0 \tag{2.49}$$

The boundary conditions are

$$\phi(z) = 0 \quad at \ z = -h \quad (bottom) \tag{2.50}$$

$$(c - u_o)^2\phi(z) = g\phi(z) \quad at \ z = 0 \quad (top) \tag{2.51}$$

The top boundary condition (2.51) is the boundary condition for free surface configuration. A simpler condition for top boundary with rigid lid approximation is given by

$$\phi(z) = 0 \quad at \ z = 0 \ \ (top) \tag{2.52}$$

We use (2.52) as the top boundary condition for analysis in this study because of its simplicity . The eigenvalue problem was solved numerically with shooting method. Generally, the eigenvalue problem defines an infinite sequence of discrete modes $\phi_m^{\pm}$, $m = 0,1,2,\ldots$, with corresponding speeds $c_m^{\pm}$. The super script "±" indicates propagation direction of wave in two-dimensional space, $c_m^+ > u_{Max} = \max(u_{o(z)})$ and $c_m^- < u_{Min} = \min(u_{o(z)})$. An example of the eigenfunctions for particular density profile is shown in Figure 2.5. The eigenfunction ϕ for mode-m takes m extremal values.

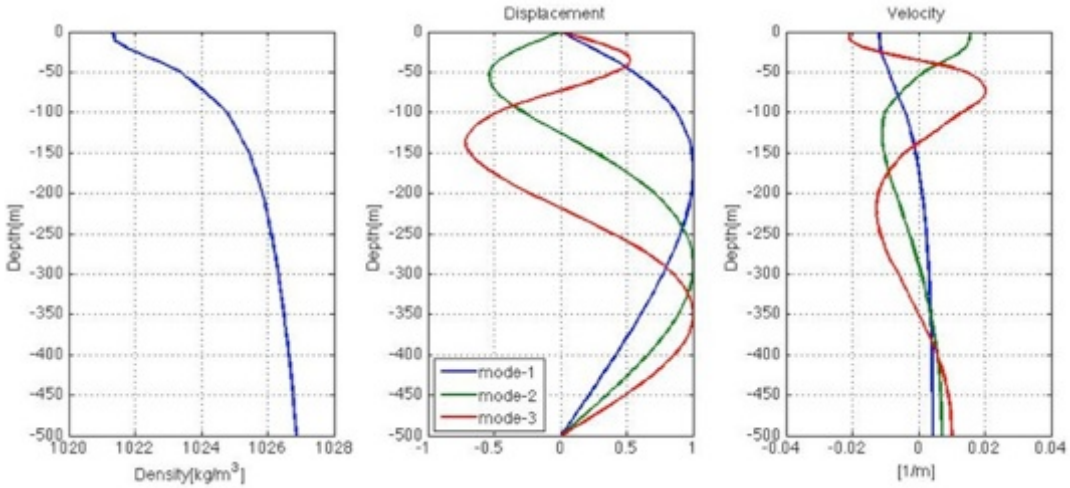

Figure 2.5 An example of the vertical profile of density, eigenfunctions ϕ and ϕ_z from left to right.

Waves propagating to opposing direction of the background flow $u_{o(z)}$ are considered in this study because we focus on a situation where the internal wave is trapped by background flow. The speeds $c_m^{\pm}$ are given in static frame of reference, so the waves with $c_m^{\pm} = 0$ are steady waves in the static frame of reference. The wave speed is counterpart of Doppler velocity in uniform flow. Modal function is normalized to have $\phi_{m(z_m)}^{\pm} = 1$ where z_m is position where $|\phi_{m(z)}^{\pm}|$ takes maximum value. With this normalization, $A(x-ct)$ corresponds to the maximum vertical displacement in vertical water column for specific position and time. As far as this linear theory can be applied, all variables for each mode are determined by (2.45)-(2.48) once the $A(x-ct)$ is determined.

There might be waves with $u_{Min} < c_m^{+} < u_{Max}$ and they are called critical-layer (singular) modes (Maslowe and Redekopp, 1980). Modal function and phase speed for those waves are not obtained by the eigenvalue problem and a different procedure is necessary (Maslowe and Redekopp, 1980). These modes are singular and they are beyond the focus of our research and we do not treat singular mode in this study.

If there is no background shear flow u_o, the eigenvalue problem becomes the following equation with Boussinesq approximation.

$$\frac{\partial^2 \phi_{m(z)}}{\partial z^2} + \frac{N^2}{c_m^2}\phi_{m(z)} = 0 \tag{2.53}$$

$$\phi_{m(z)} = 0 \quad at \quad z = -h, 0 \tag{2.54}$$

Since this is a 2nd order ordinary differential equation known as Sturm-Liouville problem, the eigenfunctions $\phi_{m(z)}$ (m=1,2,3…) compose vertical modes of velotiy $\partial\phi_{m(z)}/\partial z$ that are orthogonal to each other.

$$\delta_{mn} I_n = \int_{-h}^{0} \left(\frac{\partial \phi_{n(z)}}{\partial z} \frac{\partial \phi_{m(z)}}{\partial z} \right) dz \tag{2.55}$$

This relation enables us to decompose the observed velocity profile or results of simulation into different modes. The relation between wave shape $A_m(x-ct)$ and induced velocity u_m of particular mode m is given by

$$u_m = A_m(x - ct)c_m\phi_{mz} \tag{2.56}$$

The wave shape of each mode $A_m(x - ct)$ is obtained as follows

$$A_m(x - ct) = \int_{-h}^{0} u\phi_{mz}dz \Big/ \int_{-h}^{0} c_m\phi_{mz}\phi_{mz}dz \tag{2.57}$$

and the total velocity u can be written as the summation of each modes.

$$u = \sum A_n(x - ct)c_n\phi_{nz} \tag{2.58}$$

In the field of physical oceanography, one of the solutions of the eigenvalue problem with the largest phase speed is called as *barotropic* mode, while other modes are called as *baroclinic* mode. The barotropic mode is equivalent to the motion of long surface waves, while the baroclinic mode is equivalent to the motion of long internal waves. The barotropic mode induces vertically uniform flow, while the baroclinic mode induces the velocity whose vertical mean equals to zero if there is no background flow $u_{o(z)}$.

We finally note the effect of the background shear flow $u_{o(z)}$ on solution of eigenvalue problem to obtain internal wave's property. To have an insight, the Taylor Goldstein equation is useful and is given by, with Boussinesq approximation but without long wave approximation,

$$\frac{\partial^2\psi_{m(z)}}{\partial z^2} + \left\{\frac{N^2}{\left(u_{o(z)} - c\right)^2} - \frac{\partial^2 u_{o(z)}/\partial z^2}{\left(u_{o(z)} - c\right)} - k^2\right\}\psi_{m(z)} = 0 \tag{2.59}$$

At least for the linear situation with sinusoidal wave, next relation (2.60) is valid and the equations (2.49) and (2.59) are equivalent.

$$\phi_{m(z)} = \left(u_{o(z)} - c\right)\psi_{m(z)} \tag{2.60}$$

The Taylor Goldstein equation is relevant to the eigenvalue problem (2.49), but the eigenfunction is stream function. Background shear flow $u_{o(z)}$ appears in two terms in the Taylor Goldstein equation (2.59). The second term in the bracket is necessary to describe instability in boundary layer flow with homogeneous fluid. The Rayleigh criterion can be obtained by neglecting the first term. The importance of the term depends on the magnitude of each term in bracket in (2.59). If we consider the typical value of N^2 as $10^{-4}s^{-2}$, $\left(u_{o(z)} - c\right)$ as 1m/s and vertical length scale as 500m for the situation Kuroshio past around the island in summer, the ratio is given by

$$\frac{N^2}{\left(u_{o(z)} - c\right)^2} : \frac{\partial^2 u_{o(z)}/\partial z^2}{\left(u_{o(z)} - c\right)} : k^2 = O(10^{-4}) : O(10^{-5}) : O(10^{-6}) \tag{2.61}$$

which means that the first term is the most significant. However, the first two terms depend on the depth and it is unreasonable to neglect the background velocity profile when we consider the Kuroshio past islands.

2.3.2 Weakly Nonlinear Theory - KdV Equation

When the wave is not considered to be infinitesimal nor long enough to be non-dispersive, linear long wave theory cannot describe the internal wave accurately as time increases. Then, we need to include the effect of nonlinearity and wave dispersion in the model equations. A weakly nonlinear KdV type theory includes the both effect by asymptotic analysis with introducing two small parameters α and ϵ, respectively characterizing the wave amplitude

and dispersion. A KdV equation is obtained when the both effects balance ($\alpha=\epsilon^2$) with a corresponding time scale of ϵ^{-3}. The derivation of the KdV equation is described below.

To describe the nonlinear and dispersive nature of the long internal waves whose length scale is much larger than water depth and whose time scale is much longer than N^{-1}, following scaled variables are introduced

$$\tau = \epsilon\alpha t\,, \qquad \theta = \epsilon(x - ct) \tag{2.62}$$

and vertical displacement is rewritten as follows.

$$\zeta = \alpha A(\theta, t)\phi(z) + \alpha^2\zeta_2 + \cdots, \tag{2.63}$$

Here we only focus on a particular mode. At leading order, linear long wave theory is obtained. At the next order, equation for ζ_2 is obtained as follows.

$$\frac{\partial}{\partial z}\left(\rho_o(c-u_o)^2\frac{\partial\zeta_{2\theta}}{\partial z}\right) + \rho_o N^2\zeta_{2\theta} = M_2 \tag{2.64}$$

$$\zeta_{2\theta} = 0 \quad at\ z = -h \quad (bottom) \tag{2.65}$$

$$\rho_o(c-u_o)^2\zeta_{2\theta z} - \rho_o g\zeta_{2\theta} = N_2 \quad at\ z = 0 \quad (top) \tag{2.66}$$

where

$$M_2 = 2\{\rho_o(c-u_o)\phi_z\}_z A_\tau + 3\{\rho_o(c-u_o)^2\phi_z^2\}_z AA_\theta - \rho_o(c-u_o)^2\phi A_{\theta\theta\theta} \tag{2.67}$$

$$N_2 = 2\{\rho_o(c-u_o)\phi_z\}A_\tau + 3\{\rho_o(c-u_o)^2\phi_z^2\}AA_\theta \tag{2.68}$$

The left hand side of (2.64) is identical to the equations defining modal functions for first order. In order to have a solution for $\zeta_{2\theta}$, the required compatibility condition is satisfied. According to the fourth formula of (G) in Ince (1926), p.268, the compatibility condition is written as follows.

$$\int_{-h}^{0} M_2\phi dz = [N_2\phi]_{z=0} \tag{2.69}$$

By substituting (2.67) and (2.68) into (2.69) the following KdV equation is obtained.

$$A_\tau + \mu AA_\theta + \lambda A_{\theta\theta\theta} = 0 \tag{2.70}$$

where

$$I\mu = 3\int_{-h}^{0}\{\rho_o(c-u_o)^2\phi_z^3\}dz \tag{2.71}$$

$$I\lambda = \int_{-h}^{0}\{\rho_o(c-u_o)^2\phi^2\}dz \tag{2.72}$$

$$I = 2\int_{-h}^{0}\{\rho_o(c-u_o)\phi_z^2\}dz \tag{2.73}$$

The KdV equation has the following analytical solution

$$A = a\,\mathrm{sech}^2\,[\,\beta(\theta - V\tau)\,] \tag{2.74}$$

where

$$V = \frac{1}{3}\mu a = 4\lambda\beta^2 \tag{2.75}$$

Note that the dimensional amplitude at $z = \mathrm{z}_m$ is not a but αa because of the formulation (2.63). In addition, V denotes modulation of the phase speed and the actual total speed of wave propagation is $c + \alpha V$. If we change the scaled valuable θ and τ to original independent variables x and t, the solitary wave solution is written as follows.

$$\alpha A = \eta_o \operatorname{sech}^2 \left[\frac{(x - ct - \alpha Vt)}{L_{KdV}} \right] \tag{2.76}$$

where actual amplitude η_o and KdV length scale L_{KdV} satisfy following equation.

$$\eta_o L_{KdV}^2 = 12 \frac{\lambda}{\mu} \tag{2.77}$$

Since the right hand side is defined as constant for each mode, the larger amplitude solitary wave become narrower because amplitude η_o is proportional to L_{KdV}^{-2} as far as the internal solitary wave is in the range of requirement of KdV theory.

The second term and third term in (2.70) clearly shows the nonlinearity and dispersion respectively. The ratio μ/λ is dimensional quantity and it affects the nature of waveform; strong bore forms with large μ/λ and weak bore with a more sinusoidal motion forms with small μ/λ (Holloway, 2004). Observational study from Yang, et al. (2009) reported that the value is related with the frequency of the internal solitary wave appearance in South China Sea. The nondimensional Number related to the wave character is known as Ursell Number. The Ursell Number is defined as a ratio of the nonlinear term and the dispersion term. When we define the Ursell Number as a ratio of the second and third terms in (2.70),

$$Ur \equiv \frac{\mu A A_\theta}{\lambda A_{\theta\theta\theta}} \cong \frac{\mu}{\lambda} \frac{\eta_o}{\alpha} \epsilon^2 L_{KdV}^2 = O(\frac{\mu}{\lambda} \eta_o L_{KdV}^2)$$

The Ursell parameter is proportional to the value of $\mu\eta_o L_{KdV}^2/\lambda$. According to (2.77), the value of $\mu\eta_o L_{KdV}^2/\lambda$ takes 12 if the wave is perfectly described by KdV solitary wave profile.

2.3.3 Froude Number and Its Definition in This Study

The term "Froude Number" changes its meaning in different situation (see, Baines, 1998). In the field of marine engineering, the quantity $U/\sqrt{gL}$, where U is speed of a ship, L is typical horizontal length scale, is regarded as the "Froude Number" because it is the nondimensional parameter for wave drag produced by a ship (Baines, 1995). In the hydraulics of the streams the "Froude Number" is regarded as $U/\sqrt{gh}$, where U is speed of a stream and h is the water depth. As the "Froude Number", $U/\sqrt{gh}$, exceeds unity, it is known that nonlinear long wave such as hydraulic jump or undular bore emerges. The basic mechanism of the generation of the nonlinear waves is formation of a shock. The term "Froude Number" is not only used for the dynamics in homogeneous fluid but also the dynamics in stratified fluid. The quantities, U/NL and U/ND, where N is Brunt-Visalla frequency and D is typical vertical length scale, are both called "Froude Number" because they relate to the wave drag and wave propagation respectively. Since our focus is the nonlinear internal wave, we use the term "Froude Number" defined as a ratio of advection speed U and propagation speed of wave c

$$Fr = \frac{U}{c} \tag{2.78}$$

If the U is the flow speed of compressible fluid and the c is phase speed of acoustic wave, the Froude Number is equivalent to the Mach Number used in the field of aerodynamics. Like the shock wave, nonlinear wave emerges if the Froude Number exceeds unity. Upon the value of the Froude Number, the situation is categorized to following three.

(1) Subcritical ($Fr < 1$) : Waves can propagate upstream of the flow.

(2) Critical ($Fr = 1$) : Waves are steady from the static frame of reference.

(3) Supercritical ($Fr > 1$) : Waves cannot propagate upstream of the flow.

As it is shown in the subsection 2.4, the critical condition ($Fr = 1$) is important for the generation of the nonlinear internal wave.

In this study, our flow is not vertically uniform, so the Froude Number should be redefined. Following the typical definition of the Froude Number, Froude Number for internal waves in stratified shear flow is defined as

$$Fr_m = \left| \frac{U}{c_m - U} \right| \tag{2.79}$$

where U is vertical mean speed of background flow $u_{o(z)}$ and the c_m is wave's propagating speed of each mode from the static frame of reference. The c_m is considered to be one of the internal waves, which propagates in opposing discretion to the background flow. The denominator in the right hand side of (2.79) shows the propagating speed of the wave from the observer moving with speed U, so it is understood as the phase speed including background shear flow effect, while the numerator is advection speed of the flow.

We define the background flow has positive value, so the c_m is negative if the sitiatuion is subcritical and is positive at supercritical situation. The exactly critical situation makes c_m zero and the Froude Number defined by (2.79) becomes one. The Froude Number means physically same as the one defined for the wave in uniform flow.

2.3.4 Nonlinearity and Dispersion

The Ursell Number shows the ratio of the nonlinear and dispersion effect but each of them can be evaluated by comparison with linear term. According to Pelinovskii et al (2000), dimensional form of the KdV equation is written as

$$\eta_t + c\eta_x + \mu\eta\eta_x + \lambda\eta_{xxx} = 0 \tag{2.80}$$

This is just rewritten form of (2.70) with independent variables (x, t). The first two terms consist linear wave equation. Each of the first two terms $\eta_t + c\eta_x$ are one order greater than other terms, but the whole value of $\eta_t + c\eta_x$ is same order and acts as the tendency term shown in (2.70). The coefficients μ and λ are determined by c_m, $u_{o(z)}$ and $\phi_{m(z)}$ and they are explicitly defined by (2.71)-(2.73). Here we assume no background shear flow $u_{o(z)}$ for simplicity. By assuming that the wave is sinusoidal with wave number of k, we rewrite the KdV equation as follows

$$\eta_t + c(1 + \mu\eta/c - k^2\lambda/c\,)\eta_x = 0 \tag{2.81}$$

The relative importance of each term becomes clear with (2.81). The nonlinearity is estimated to be $\mu\eta/c$ as a ratio of the nonlinear term and linear term. If the η takes the value that makes $\mu\eta/c_m$ unity, the situation is strongly nonlinear and the assumpotion used to derive the KdV, $\alpha \ll 1$, is no longer valid. On the other hand, the importance of the wave dispersion depends on $k^2\lambda/c$.

The coefficients μ *and* λ are nondimensionalized by choosing h for both of horizontal and vertical length scale and they are given by

$$\mu' = (\mu h)/c, \qquad \lambda' = (2\pi)^2 * \lambda/(ch^2) \tag{2.82}$$

The coefficient $(2\pi)^2$ for nondimensional dispersion parameter λ' is added on purpose and the reason is described below. The μ and λ are dimensional and are given by

$$\mu = \frac{3c\int_{-h}^{0}\phi_z^3 dz}{2\int_{-h}^{0}\phi_z^2 dz}, \qquad \lambda = \frac{c_m\int_{-h}^{0}\phi^2\, dz}{2\int_{-h}^{0}\phi_z^2 dz}$$

The nondimensional forms of these coefficients are explicitly given by

$$\mu' = \frac{3\int_{-1}^{0}\phi_z^3 dz}{2\int_{-1}^{0}\phi_z^2 dz}, \qquad \lambda' = (2\pi)^2\frac{\int_{-1}^{0}\phi^2\, dz}{2\int_{-1}^{0}\phi_z^2 dz} \tag{2.83}$$

We can clearly see that μ' and λ' only depends on the eigenfunction. With μ' and λ', we can rewrite the KdV equation as follows

$$\eta_t + c_m\left(1 + \mu'\frac{\eta}{h} - \lambda'\frac{h^2}{l^2}\right)\eta_x = 0 \tag{2.84}$$

The equation (2.84) indicates that nonlinearity and dispersion balances as long as η/h and h^2/l^2 are same order and this is exactly the requirement of KdV formulation, namely $\alpha = \varepsilon^2$. For example, take the density profile as follows.

$$\rho_{(z)} - \rho_{(-0.2)} = \tanh\left((z + 0.2) * c_{shape}\right), \qquad -1 < z < 0 \tag{2.85}$$

The values of μ' and λ' for each profiles with parameter c_{shape} are calculated as shown in Figure 2.6(bottom). The values of μ' and λ' are same order and nonlinear term and dispersion terms in (2.84) that balance as far as the nonlinearity η/h and dispersion h^2/l^2 are comparable, which is exactly the requirement of KdV formulation. The series of μ' and λ' shown in Figure 2.6 shows that nonlinearity becomes significant as the density profile changes from linearly stratified to two-layer configuration, in other words, as c_{shape} becomes larger. The coefficient λ' is known to be weakly dependent on the detail of the density profile (Holloway and Pelinovsky, 2002).

If we consider the density anomaly $\Delta\rho$ of the density profile given by

$$\rho_{(z)} - \rho_{(-0.2)} = \Delta\rho\tanh\left((z + 0.2) * c_{shape}\right), \qquad -1 < z < 0 \tag{2.86}$$

One can immediately find that $\Delta\rho$ does not influence on the eigenfunction but changes phase speed. If we apply the Boussinesq approximation and neglect the background shear flow, the eigenvalue problem is rewritten as

$$\frac{\partial^2\phi(z)}{\partial z^2} + \frac{N^2}{c^2}\phi(z) = 0 \tag{2.87}$$

The profile (4.1) determines Brunt-Vaisala frequency as follows.

$$N^2 = -\frac{g}{\rho_{o(z)}}\frac{\partial\rho_{o(z)}}{\partial z} \approx -\frac{\Delta\rho g c_{shape}}{\rho_{ob}}\, sech^2\left((z + 0.2) * c_{shape}\right) \qquad -1 < z < 0 \tag{2.88}$$

There is no dependency on $\Delta\rho$ in (2.78) once c is changed to $c\sqrt{\Delta\rho}$.

By changing the parameter c_{shape}, a comparison between two-layer case and continuously stratified case can be made. It was found that two-layer configuration promotes the SAR to detect internal solitary wave because the nonlinear parameter and the value of modal function for velocity at surface are larger, while the dispersion parameter is smaller

compared to more gradually changing density profile.

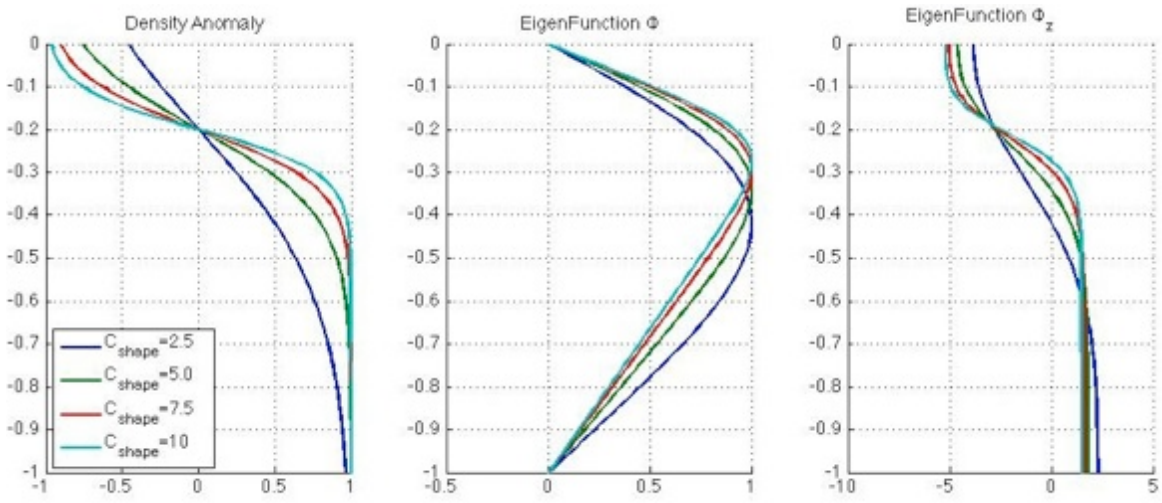

Cshape	Nonlinearity μ'	Dispersion λ'	Normalized Phase Speed
2.5	−1.797	1.858	0.797
5.0	−3.421	1.617	0.897
7.5	−4.377	1.440	0.936
10.0	−4.871	1.341	0.975
2−Layer	−5.625	1.054	1.000

Figure 2.6 Nondimensional coefficients for nonlinear term, dispersion term in KdV equations and phase speeds for the mode-1 internal waves in series of density profiles defined by hyperbolic tangent function and the 2-layer case. Phase speeds are normalized by the value of 2-Layer configuration.

2.3.5 Sea Surface Current induced by Internal Wave and related Internal Wave Properties.

Detection of the internal solitary wave by the SAR depends on the sea surface current induced by the internal solitary wave. Linear theory provides the relation between the amplitude of the internal wave and the velocity created by the internal wave (2.46) and it is shown again as follows.

$$u = A(x - ct)[(c - u_o)\phi(z)]_z$$

Backscattering intensity of SAR linearly depends on sea surface velocity strain and the component induced by internal wave is given by

$$u_x = [A(x - ct)]_x[(c - u_o)\phi(z)]_z \quad at \quad z = 0\ (sea\ surface) \tag{2.89}$$

The intensity of the strain induced by internal wave depends on the wave amplitude, wavelength, phase speed, background current and vertical structure of the eigenfunction. The large value of the surface velocity strain is necessary for the internal wave to be detected by SAR. Although wave amplitude and wavelength cannot be determined until it is measured, we could estimate the $[(c - u_o)\phi(z)]_z$ at the surface, phase speed c and nonlinearity μ' by solving the eigenvalue problem. We call these three variables as internal wave properties and

used in this study.

The values of three variables $[(c-u_o)\phi(z)]_z$, at the surface, propagating speed c and nonlinearity μ' are important because of the following two reasons. First surface convergence is linearly proportional to $[(c-u_o)\phi(z)]_z$, at the surface, so the large $[(c-u_o)\phi(z)]_z$ is preferable for the detection by SAR. If the situation can be approximated to two-layer case, large $[(c-u_o)\phi(z)]_z$ at surface is obtained when the interface is near surface. Next, if the wave is nonlinear, not only $A(x-ct)$ is large but also wave profile is steepened by nonlinear effect and make wave steepness $[A(x-ct)]_x$ larger compared to linear wave.

If the wave is solitary wave and its shape is described by KdV solution given by

$$A(x-ct) = \eta_o \operatorname{sech}^2\left[\frac{(x-ct-\alpha Vt)}{L_{KdV}}\right]$$

$$\eta_o L_{KdV}^2 = 12\frac{\lambda}{\mu}$$

and the induced velocity strain has following relation.

$$u_x \propto \frac{\eta_o}{L_{KdV}}[(c-u_o)\phi(z)]_z = \sqrt{\frac{(2\pi)^2}{12}\frac{\mu'}{\lambda'}\left(\frac{\eta_o}{h}\right)^3}\,[(c-u_o)\phi(z)]_z \tag{2.90}$$

The equation (2.90) describes that velocity strain at sea surface induced by internal solitary wave is proportional to not the wave amplitude η_o itself but ${\eta_o}^{3/2}$ because the solitary wave become steeper as amplitude becomes larger.

2.3.6 Higher Order Weakly Nonlinear Model and Fully Nonlinear Model

For an internal wave of large amplitude, a higher order weakly nonlinear model and fully nonlinear model for continuously stratified shear flows are available. The first one is called extended KdV equation and the latter one is called Dubreil-Jacotin-Long (DJL) equation.

Formally, the extended KdV equation is obtained by assuming the nonlinear coefficient parameter μ is small. The equation has the following form

$$A_t + (c + \mu A + \nu A^2)A_x + \lambda A_{xxx} = 0 \tag{2.91}$$

where the cubic nonlinear term $\nu A^2 A_x$ is included in addition to the original KdV equation (2.80). The cubic nonlinearity coefficient ν is more complex compared to other coeffcients and it is given by

$$\nu I = \int_{-h}^{0} \rho_o \{3(c-u_o)^2[3\xi_z - 2\phi_z^2]\phi_z^2 - \mu^2\phi_z^2 + \mu(c-u_o)[5\phi_z^2 - 4\xi_z]\phi_z\}dz \tag{2.92}$$

where ξ is a solution of the following ordinary differential equation

$$\frac{\partial}{\partial z}\left((c-u_o)^2\frac{\partial\xi}{\partial z}\right) + N^2\xi = -\mu\frac{\partial}{\partial z}\left[(c-u_o)\frac{\partial\phi}{\partial z}\right] + \frac{3}{2}\frac{\partial}{\partial z}\left[(c-u_o)^2\left(\frac{\partial\phi}{\partial z}\right)^2\right] \tag{2.93}$$

with boundary condition

$$\xi = 0 \quad at\ z = -h \quad (bottom)\ and\ 0\ (top) \tag{2.94}$$

and the normalized condition

$$\xi(z_m) = 0 \quad , where \quad \phi_{(zm)} = 1 \tag{2.95}$$

The inclusion of cubic nonlinear term to the model equation is important when the wave amplitude is large or the coefficient μ is close to zero. The extended KdV equation is known

to give the steady wave solution whose shape is wider than KdV solitary wave, so the eKdV equation is often used to compare with the observed wave profile.

Another model equation for large amplitude internal solitary wave is Dubreil-Jacotin-Long (DJL) equation given by

$$\nabla^2\eta + \frac{N_{(z-\eta)}{}^2}{c^2}\eta = 0 \tag{2.96}$$

with boundary conditions

$$\eta = 0 \quad at\ z = -h \quad (bottom)\ and\ 0\ (top) \tag{2.97}$$

$$\eta = 0 \quad at\ |x| \to \infty \tag{2.98}$$

The equation (2.96) is nonlinear elliptic eigenvalue problem and is solved by determining available potential energy for the internal solitary wave *a priori* and by minimizing the perturbation kinetic energy (Statsna and Peltier 2005). The method is called direct variational method produced by Turkington et al. (1991). With this method, neither of wave amplitude nor the propagation speed is fixed a priori. There is also the nonlinear elliptic eigenvalue problem producing wave shape of nonlinear internal wave in background shear flow shown in Statsna and Lamb (2002).

2.4 Generation Mechanism of the Internal Solitary Wave

An internal solitary wave is known for its stability; the wave propagates more than hundreds of kilometers without changing its shape significantly. This property enables the wave to be detected by satellite sensors frequently. As shown in this section, an internal solitary wave is formulated as a steady solution because of a balance between nonlinearity and wave dispersion. Therefore, once the internal solitary wave is generated, it propagates a long distance without changing its shape. Then, a question arises to the generation mechanisms of the internal solitary wave. The generation mechanisms are different in a number of ways (Jackson et al, 2012). We here describe the lee wave generation mechanism and the resonant forcing since they are related to this study.

2.4.1 Lee Wave Generation

The lee wave generation mechanism is first suggested by Maxworthy (1979) with laboratory experimental results. The experiment considered periodic flow over the obstacle for the model of tidal flow over the topographical features like sill. Suppose there is a two-fluid system with an upper layer with density ρ_1 and thickness h_1, while the lower layer has its density ρ_2 and thickness h_2. This is the simplest approximation of the ocean as a stratified fluid. The linear long phase speed of the internal wave is known as follows.

$$c_o^2 = \frac{gh_1h_2(\rho_2 - \rho_1)}{\rho_1 h_2 + \rho_2 h_1} \tag{2.99}$$

We consider the situation $h_1 \ll h_2$ as the h_1 is upper layer thickness above thermocline. The lee wave generation process is schematically described in Figure 2.7. As the flow increases its velocity larger than the internal wave's phase speed, no information can propagate upstream, so the situation is supercritical. However, when the flow passes over the topography, upper

layer thickness h_1 increases to create a steady state. As the h_1 increases, phase speed c also increases and became equals to background advection speed U. Then, the disturbance is steady even though the infinitesimal disturbance for original state should be propagated downstream. As the velocity of flow decreases, the disturbance can propagate upstream. The lee wave has large amplitude and thus nonlinearity becomes important. As time passes, the both effects of nonlinearity and dispersion balances to create nonlinear internal solitary wave train (Figure 2.7, b and c)

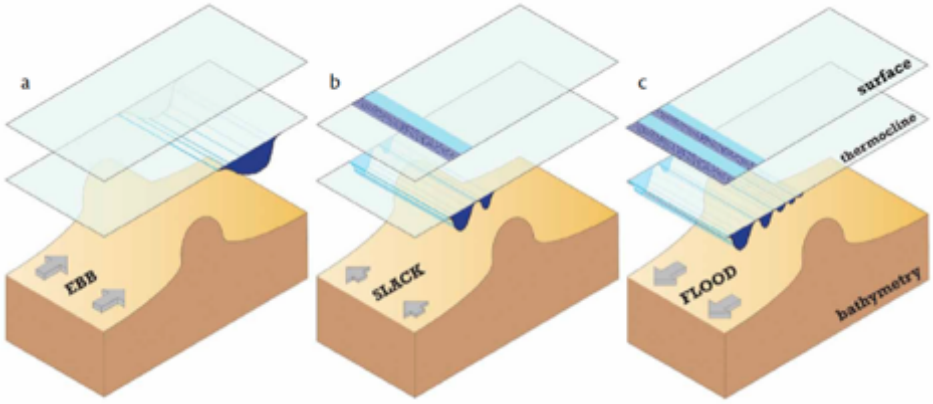

Figure 2.7 A schematic showing a mechanism of nonlinear internal wave generation suggested by Maxworthy (1979). (a) Supercritical flow past over the sill topography assuming ebb tide. Only the large amplitude lee waves remain left because of larger phase speed than linear wave. (b) As the flow decrease its velocity with time, the lee waves propagate upstream freely. The nonlinear effect steepens the wave. (c) The internal wave evolves into internal wave trains as predicted by the KdV theory. (Figure.2 in Jackson et al, 2012).

Hibiya (1986) modeled this lee wave generation with a two-layer fluid system and clarified the mechanism of large amplitude lee wave generation analytically. The use of characteristics examined the role of tidal advection effect on the generated large amplitude internal wave. In his model, infinitesimal internal waves named elementary waves are successively generated by the interaction between tidal flow and topography during the tidal cycle and an internal wave composed by elementary waves is effectively amplified as the Froude Number exceeds unity since the elementary waves slowly propagate. The amplified internal wave is periodically generated in both the accelerating and decelerating periods and they are superimposed if the tidal advection effect makes the waves approach. In his model, the nonlinear effect and dispersion effect was not considered, but could produce the initial state of the internal wave profile that should be applied to models such as the KdV equation. Hibiya (1988) additionally included background shear current in his model and clarified that the shear flow changes amplitudes of the right and left going waves significantly from the situation without the shear flow. The background shear flow modifies the advection speed of elementary waves and their amplitude that result in the asymmetry between the left and right going wave. The shear effect describe well why the large amplitude internal wave is only propagated eastward in the Gibraltar strait where the background shear flow is available as exchange flow between Mediterranean sea and Atlantic sea.

2.4.2 Resonant Forcing

Another generation mechanism of the internal solitary wave is resonant forcing from the topography. This is similar to the lee wave generation mechanism in terms of the trapping the internal wave around the topography, but here the background flow is not periodic but steady. Since the steady flow over the topography is assumed, only the near critical situation is described by the KdV equation and other subcritical and supercritical situation are known to reach the steady state after a sufficient time. Grimshaw and Smith (1986) considered the finite but small topographic change given as

$$z = -h + \alpha F(X) \tag{2.100}$$

where $X = \varepsilon x$ and incopolated the effect into the KdV equation. As a result of asymptotic expansion, forced KdV equation (fKdV) is obtained as follows (Grimshaw, 2001).

$$A_\tau + \Delta A_X + \mu A A_X + \lambda A_{XXX} + \delta F_X(X) = 0 \tag{2.101}$$

$$I\delta = \rho_o {u_o}^2 \phi_z \qquad at \quad z = -h \tag{2.102}$$

where Δ is the detuning parameter which defines the subcritical or supercritical flow. According to the numerical simulation of the fKdV equation in the Grimshaw and Smith (1986), solitary wave train propagates from the generation region over the topography. They applied the topography given as

$$F(X) = Go * G(\xi X) \tag{2.103}$$

$$G(\xi X) = \mathrm{sech}^2(\xi X) \quad or \quad G(\xi X) = \mathrm{sech}^2(\xi X) \tag{2.104}$$

and reported that the internal solitary wave trains appeared both positive ($Go > 0$) and negative ($Go < 0$) forcing. This is reasonable because the $F_X(X)$ is either positive or negative value depending on the location X.

The weakly nonlinear model for three-dimensional wave is known as Kadomstev-Petviashvili (KP) equation. The topographic forcing is also included in the KP equation and the one is called fKP equaiton. Originally, the KP equation governs the vertical displacement of the free surface in shallow water induced by a weakly nonlinear wave, but the amplitude of the vertical mode for continuously stratified flow is also governed by the KP equation (Johnson and Vilenski, 2004). The forced KP equation (fKP) without the cubic nonlinear term for continuously stratified flow is given by (Hanazaki, 1994)

$$-\frac{1}{C_n}(A_T + \Delta A_X) + a_1 A A_X + a_3 A_{XXX} + \frac{1}{2}\int_{-\infty}^{X} A_{YY}\, dX + G_X = 0 \tag{2.105}$$

The difference between fKdV (2.101) and fKP (2.105) is the term depending on the transverse direction to the main propagation direction of the wave. The KP equation is not fully three-dimensional equation because it requires the following scaling for independent variable (Hanazaki, 1994).

$$X = \varepsilon^{1/2} x, \quad Y = \varepsilon y, \quad T = \varepsilon^{3/2} t \tag{2.106}$$

The scaling is appropriate to describe diffraction of internal solitary wave, but three-dimensional wave with large curvature is not well reproduced by the KP equation. In addition, it is also difficult to treat spatially varying background flow field with KP equation.

The KP equation is used for studying the diffraction of the nonlinear oceanic internal wave whose shape is sometimes arc. In addition, the KP equation has been used for studying

the atmospheric nonlinear internal wave generated around the mountain topography in near critical situation. Johnson and Vilenski (2004) used the nondimensional forced Kadomtsev–Petviashvili (fKP) equation to study the dependence of drag on the topography, and generated internal wave properties that depended on topographic height and the difference between background uniform flow and linear wave propagation speed. The difference was called the detuning parameter, which was a parameter dynamically equivalent to the Froude Number. While Johnson and Vilenski (2004) studied nonlinear internal wave evolution by changing the parameters in the evolution equation, Burk and Haack (2000) confined their attention to the observed wave clouds upwind of coastal orography around the California coast. They conducted sub-kilometer-scale numerical simulation and reported generation of an undular bore. The induced vertical velocity distribution at particular level manifests the atmospheric bow shock.

These previous studies only focus on specific waves near critical because the background velocity field does not allow other waves to remain around the obstacle. However, if the obstacle or topography pierces the fluid, as an island pierces the water column from sea bottom to surface, the background velocity decreases as it approaches the obstacle and allows several modes to be left. The situation of near critical flow past an island topography has never studied even with the simplified topography. We numerically study the oceanic nonlinear internal wave generation around the Izu-islands in Chapter 4 and also the nonlinear internal wave around island topography in Chapter 5.

Chapter 3 Nonlinear Internal Waves Signature around Izu-Islands in Kuroshio manifested in SAR images.

Nonlinear internal waves would be generated around the Izu island in near critical stratified shear flow, the Kuroshio, by the resonant excitation of the internal waves. If the idea is correct, SAR images with parabola patterns were obtained when the Kuroshio approached the island and the wind was gentle. The other factor such as tidal flow and the seasonal variation of the oceanic stratification could influence on the generation of the nonlinear internal waves. In this section, we investigated environmental conditions to support the ideas that Kuroshio creates the critical situation and generate nonlinear internal waves.

3.1 Detection of the Parabola Patterns by SAR and Environmental Condition.

3.1.1 Parabola Patterns around Islands shown in SAR images

The Phased-Array L-band Synthetic Aperture Radar (PALSAR) was installed to the Advanced Land Observing Satellite (ALOS) that was launched on 24th January in 2006 and stopped observation on 12th May in 2011 (Figure 3.1). The PALSAR has several observation modes and the high-resolution-mode has spatial resolution from 7 to 44m on the ground with measuring width with 40-70km. Although the repeat cycle is 46 days, variable off-nadir angle makes it possible to observe specific point every two days. The PALSAR is L-band SAR, so the wavelength of the signal is 23.5cm. The typical incident angle is about 30deg, so the Bragg scattering signal was obtained by the wind wave with wavelength of 23.5cm.

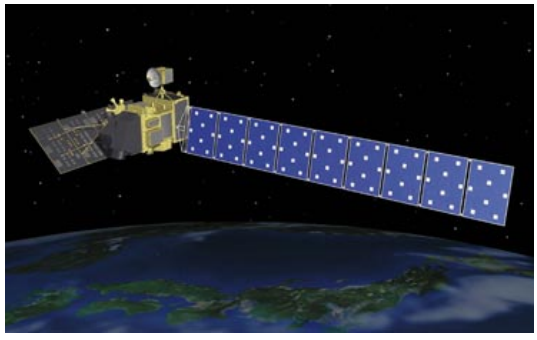

Figure 3.1 The satellite ALOS and PALSAR (source: http://www.jaxa.jp/projects/sat/alos/)

A number of SAR images obtained by PALSAR can be ordered in the CROSS-EX website (https://cross.restec.or.jp/) or ALOS User Interface Gateway (https://auig.eoc.jaxa.jp/). To see the images with high resolution, one has to buy the images, but some of the images with low resolution can be browsed and downloaded for free. We collected images including Izu-Islands to check how frequently the parabola patterns were measured. The measurement was done for 138 days in total and we found that the parabola patterns were found in 13 days. We introduce those pictures in Figure 3.2-Figure 3.4. Because of the low resolution, compared to

the one (Figure 1.5) we introduced in Chapter 1, the pattern is not clear. However, in all the pictures, parabola patterns can be seen in the southwestern side of the island. It should be noted that almost all of the images were obtained during the summer season from June to October. The seasonality might be related to the seasonal variation of environmental conditions. The summary of the environmental conditions analyzed in the following subsections is shown in a Table 3.1.

As we described in section 1.2, parabolic patterns shown in SAR images imply there are trapped internal waves around the islands in the Kuroshio because the area is known as a pathway of the Kuroshio. Actually, one of the SAR images on 30th August 2010 was taken just one hour before the ADCP observation was started (Kodaira et al, 2013). The results of the 4 days ship-borne ADCP observation showed the strong ocean current around the Miyake Island (Figure 3.5). However, since the SAR images are influenced by both of atmospheric wind and oceanic surface current, we need to check both of the atmospheric and oceanic conditions to understand under what condition those parabola patterns were captured.

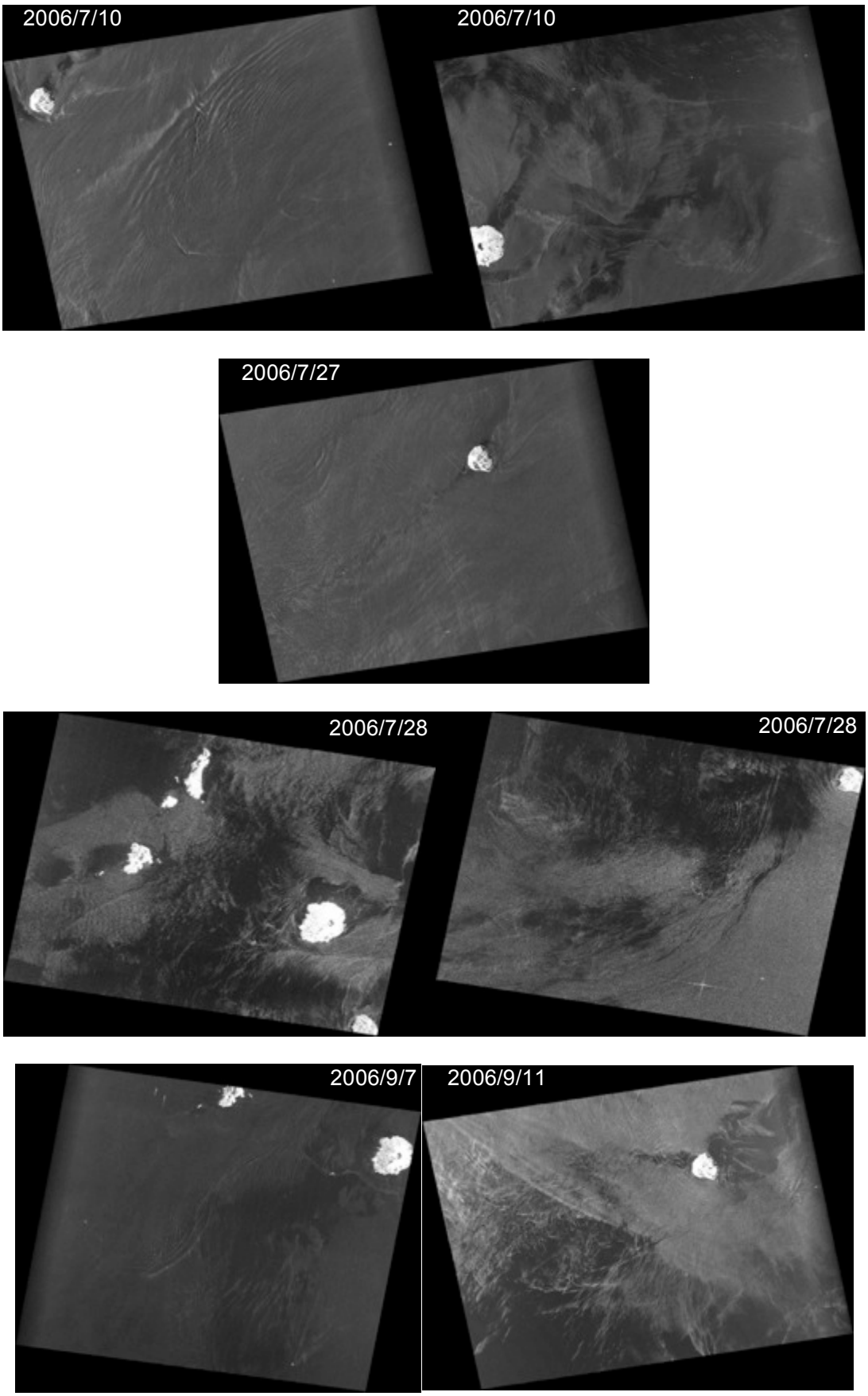

Figure 3.2 SAR images with parabola patterns. The images were acquired from CROSS-EX website (https://cross.restec.or.jp/).

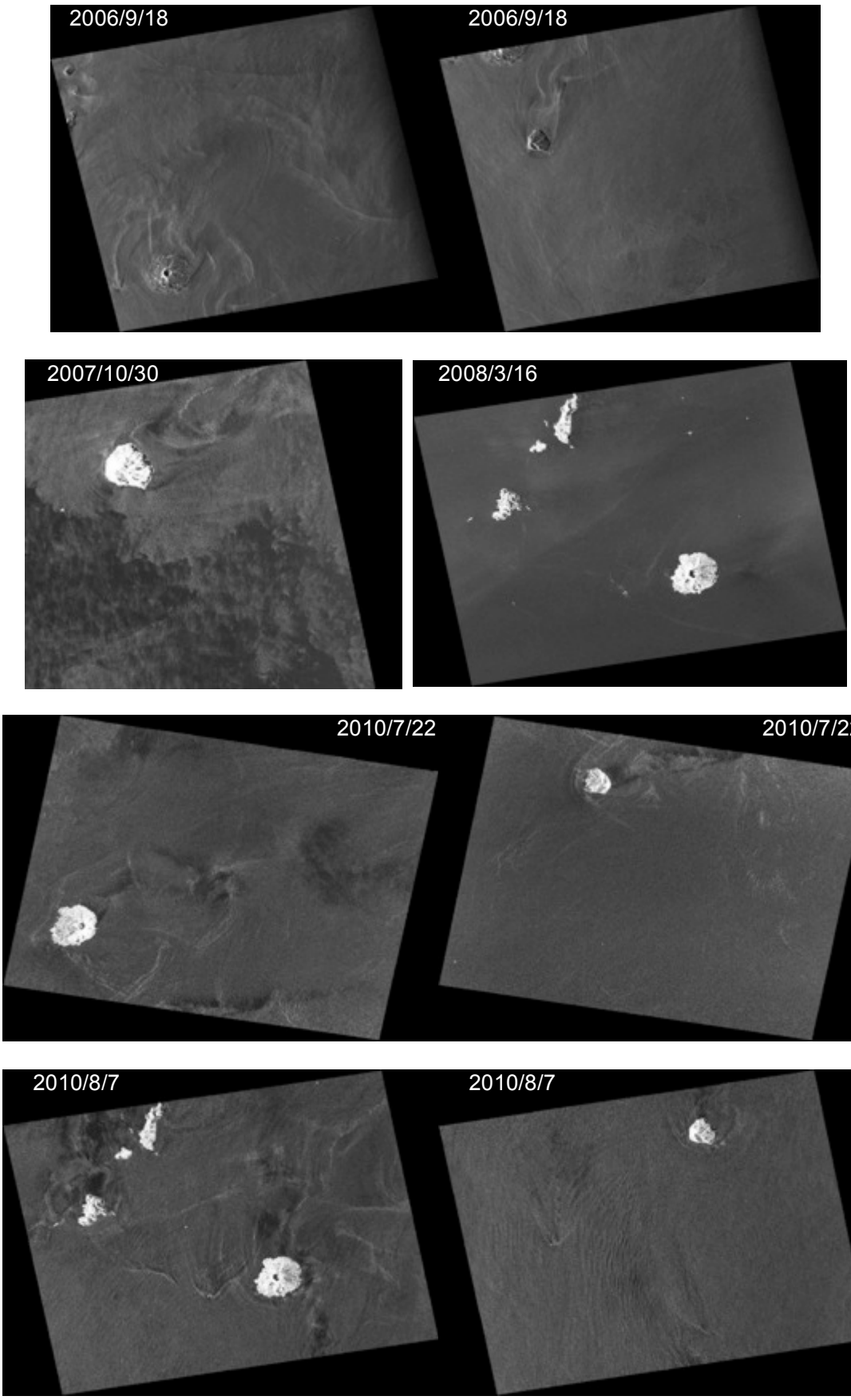

Figure 3.3 SAR images with parabola patterns. The images were acquired from CROSS-EX website (https://cross.restec.or.jp/) (continue).

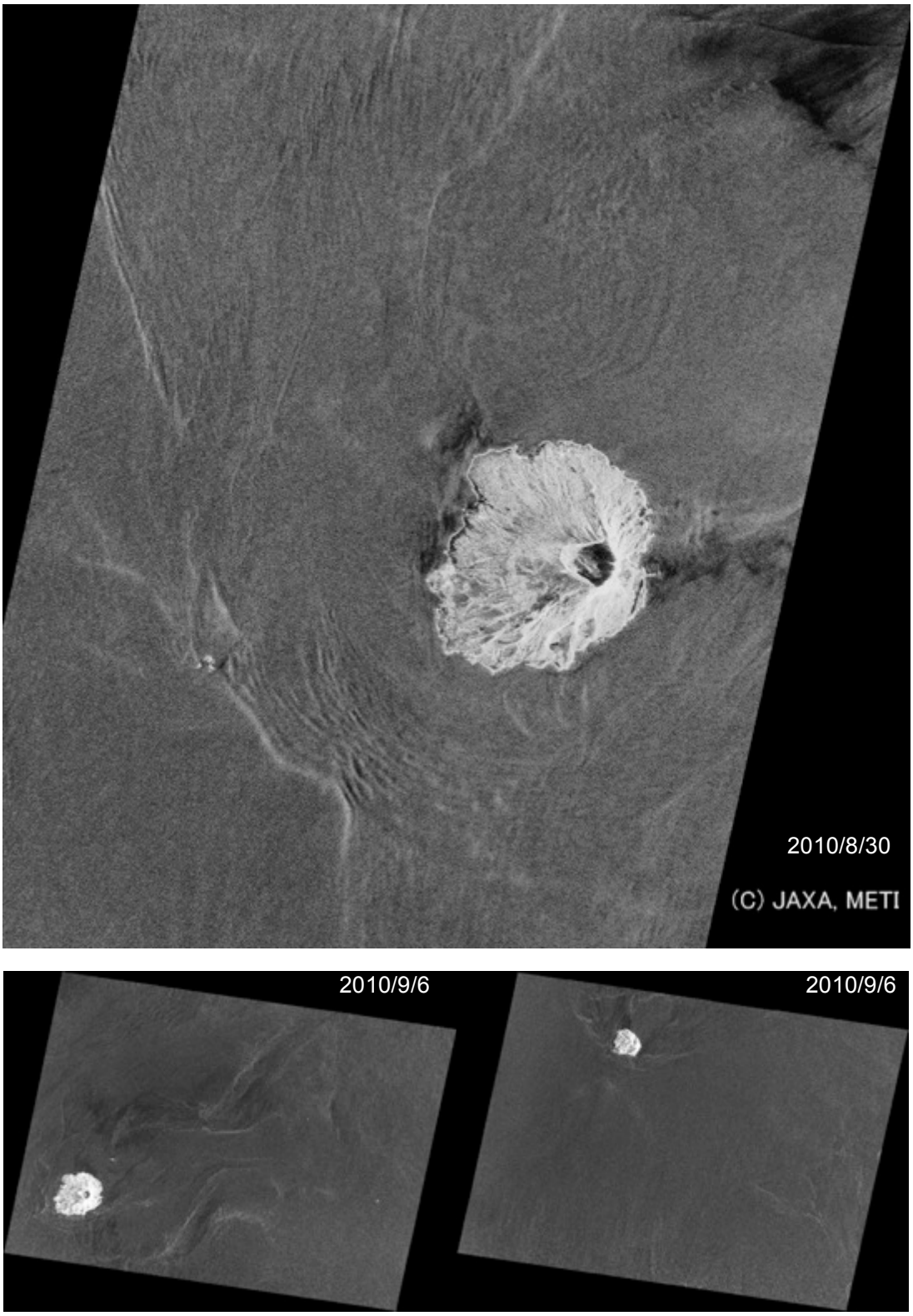

Figure 3.4　SAR images with parabola patterns (continue). The images were acquired from CROSS-EX website (https://cross.restec.or.jp/). The image obtained on 30th August 2010 was provided by Dr.Isoguchi (Courtesy of JAXA/METI).

Table 3.1　Collected SAR images with parabola patterns and environmental condition.

Date	Time	Parabola patterns		Kuroshio-axis	Wind at Miyake		Wind at Tsubota		Tidal Level
		Miyake	Mikura	distance[mile]	speed[m/s]	direction	speed[m/s]	direction	deviation[cm]
2006/6/12	1:00	Yes	Yes	0	1.3	WNW	1.0	SE	−101.6
2006/7/10	13:00	−	Yes	20	2.9	SSW	5.0	SW	2.4
2006/7/27	13:00	−	Yes	30	1.6	ESE	1.0	NE	−11.6
2006/7/28	1:00	−	Yes	30	1.2	NE	3.0	ENE	−57.6
2006/9/7	1:00	Yes	−	0	1.7	N	5.0	SSW	−89.6
2006/9/11	13:00	−	Yes	0	4.5	NE	5.0	N	−13.6
2006/9/18	13:00	Yes	Yes	30	6.1	SSW	8.0	SSW	−8.6
2007/10/30	13:00	Yes	Yes	25	2.5	S	3.0	WSW	−20.6
2008/3/16	13:00	Yes	−	0	5.3	WSW	5.0	WSW	−45.6
2010/7/22	1:00	Yes	Yes	10	1.5	NNE	5.7	SSW	−21.6
2010/8/7	13:00	Yes	Yes	0	2.2	SSE	3.1	SW	7.4
2010/8/30	1:00	−	Yes	20	4.4	SW	3.3	WNW	−11.6
2010/9/6	1:00	Yes	Yes	0	1.7	NE	5.0	SSW	−103.6

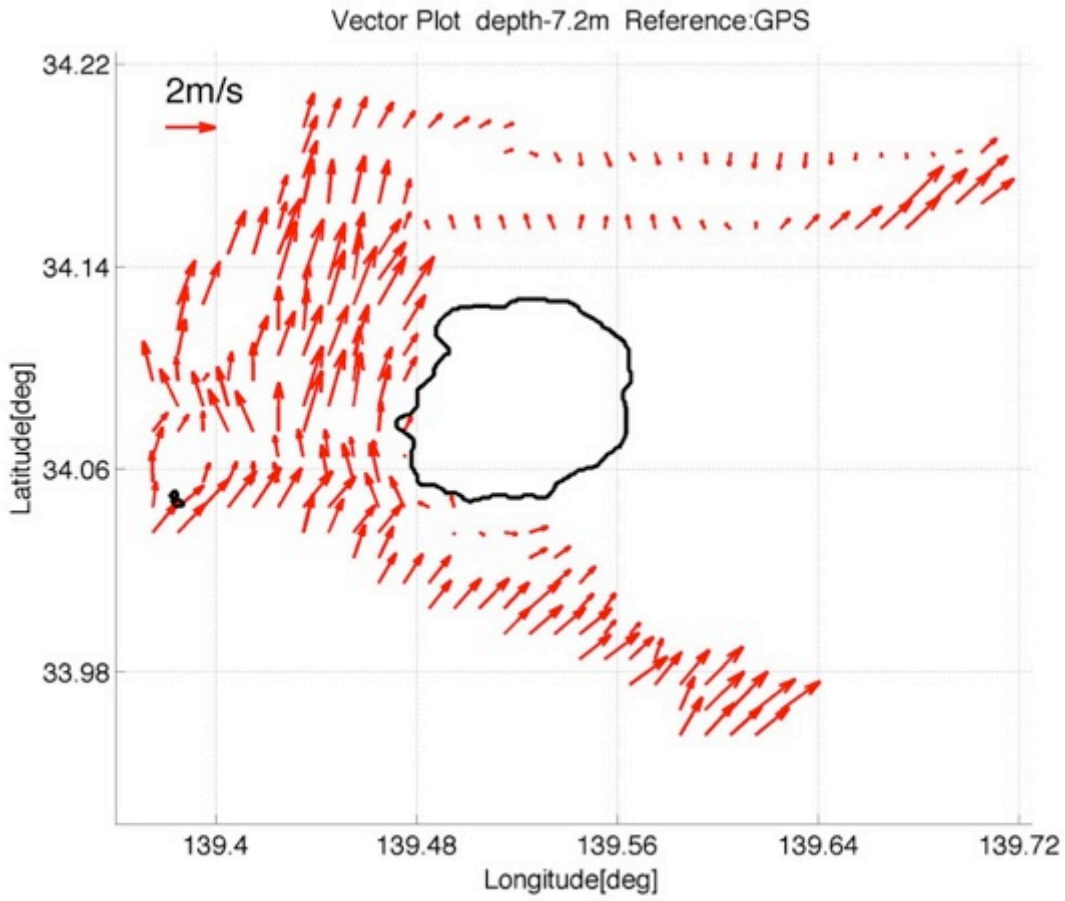

Figure 3.5　Results of 4-days ship-borne ADCP observation described in section 3.3. The acquired velocity data is temporally (2.5mins) and spatially (0.01deg×0.01deg) averaged.

3.1.2 Kuroshio axis

The Japan Coast Guard issues the Quick Bulletin of Ocean Conditions (QOBC) every weekday. The QOBC reports distances from specific points, such as islands or capes, to the Kuroshio axis and the Miyake Island is included to the list. The QOBC is not issued on weekends and national holidays. The missing values from these days are interpolated to the nearest value in the time series. The time series of the distance between the Kuroshio axis and the Miyake Island and the date when SAR image were obtained are shown in Figure 3.6. Red squares in Figure 3.6 show the days when SAR images with the parabola patterns were captured. The maximum distance between Miyake Island and Kuroshio axis among the days with red circles is 30 miles. This implies that parabola patterns were detected only when the Kuroshio approached the Miyake Island. On the other hand, blue squares in Figure 3.6 show the days when the distance is no more than 30 miles but the obtained SAR images do not include parabola patterns. This result suggests that the approach of Kuroshio to the islands is a necessary, but not a sufficient condition for PALSAR to acquire the SAR image containing parabol1a patterns.

It should be noted that the parabola patterns are detected almost all the cases in the summer season from June to October. If we assume the parabola patterns in SAR images manifest oceanic internal solitary waves, the detection is related to atmospheric and oceanic conditions that have seasonal variation. It is readily thought that wind becomes strong in winter, which prevents the manifestation of oceanic internal solitary waves in SAR image. In addition, ocean density profile varies with season, which may influence the internal wave properties. These are only qualitative description of the seasonal variation of atmospheric and oceanic condition, so we analyze the both quantitatively in this section.

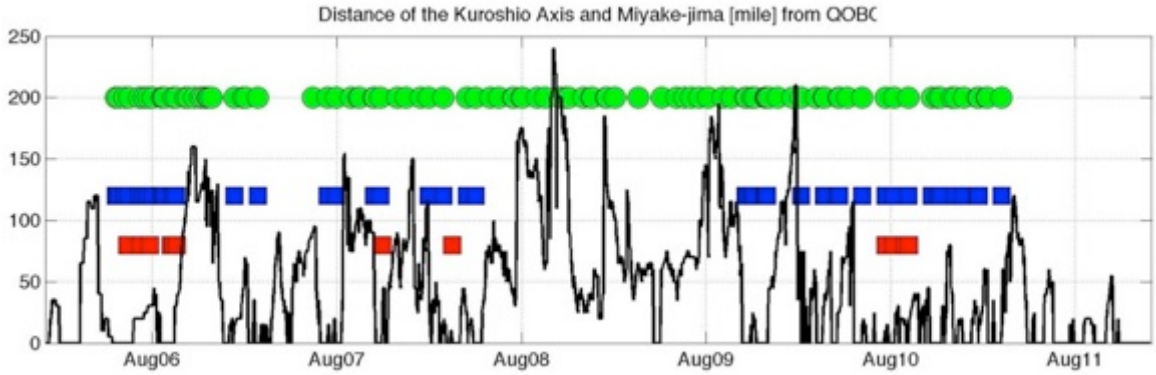

Figure 3.6 Distance between Kuroshio axis and the Miyake Island (-) with marks showing SAR image obtained. Green Circle show the dates when SAR images were obtained. Red squares show the days when SAR images with the parabola patterns obtained, while Blue squares show the days without the patterns even the distance is no more than 30mile.

3.1.3 Wind

When wind blows strongly, SAR does not detect internal waves because their modulation effect is overwhelmed by wind. If the parabola patterns in SAR images are manifestation of internal waves, they should have been obtained when the wind was gentle with its speed less

than 10m/s (Jackson, et al. 2004). It is also possible that wind creates parabola patterns in SAR images. In addition, seasonal variation of the wind around the islands should be checked to clarify why the parabola patterns are almost all captured in the summer season. Therefore, we next check the atmospheric wind condition around islands.

The Japan Agency of Meteorology has collected and published in situ wind measurement data at two locations in Miyake Island. Those observation points, named Miyakejima and Miyake-Tsubota, are located on the northwest and southeast sides of the island, respectively (Figure 3.7,Figure 3.8). We used hourly averaged wind data to clarify the relation between wind and parabola patterns in SAR images. Since the Kuroshio is necessary to detect the pattern, we check the wind data when SAR images are obtained with the Kuroshio axis distance of 30mile or less. The average speeds were 2.8m/s and 4.1m/s at two observation stations and the maximum wind speed was 8m/s when the parabola patterns were obtained (

Table 3.3). This result indicates the parabola pattern was detected when wind was gentle, which enables the oceanic internal waves manifested in the parabola patterns in SAR images.

If the parabola patterns are manifestations of the oceanic internal waves, the propagation direction should be close to wind direction because no modulation of wind wave happens if the oceanic internal wave propagates normal to wind wave propagation. Therefore, not only the wind speed, but also the wind direction, is important for oceanic an internal wave to be detected by SAR. Isoguchi et al (2010) described, southerly or southwesterly winds are dominant around the study area from early summer to midsummer because of seasonal evolution of the Asian summer monsoon. In fact, the wind data from Miyake-Tsubota shows that southwesterly wind is frequently measured. On the other hand, the wind direction measured by Miyakejima varies more and sometimes shows opposite wind direction compared to the data of Miyake-Tsubota. The opposite directions were measured on 27th/Jul/2006, 7th/Sep/2006, 22nd/Jul/2010 and 6th/Sep/2010. The wind speeds measured at Miyakejima were less than 2.0m/s on these days. The discrepancy of the wind direction between two stations can be explained by the following two points. Firstly, the small wind speed that makes the observed wind direction unsteady. Secondly, mountain topography of the Miyake Island locally changes the wind direction. We do not pursue this discrepancy further because the data at least showed a clear tendency that SAR images with parabola patterns were detected only when the wind was gentle, i.e. when the wind speed was no more than 8m/s.

Seasonal variation of the wind around the Miyake Island was also studied. A time series of the monthly averaged wind speed obtained from two stations showed clear seasonal variation. The wind speed was minimal in summer and maximal in winter. The amplitude of the variation is roughly 2m/s. We further checked how the distribution of the histograms of wind speed changes with season. The Figure 3.10 shows the histograms for hourly wind speed measured in February and August from 2006 to 2011. The numbers of measured wind speed larger than 8m/s increases significantly in winter. The stronger wind is one reason that prevents possible manifestation of the oceanic internal waves in SAR images in winter.

Table 3.2 AMEDAS wind measurements locations at the Miyake Island.

Name of the station	Longitude	Latitude	Altitude
Miyakejima	139.52E	34.12N	36.4m
Miyake-Tsubota	139.56E	34.07N	20.0m

Table 3.3 Statistical wind data at the Miyake Island.

Name of the station	with parabola patterns		without parabola patterns	
	average	maximum	average	maximum
Miyakejima	2.8m/s	6.1m/s	5.8m/s	13m/s
Miyake-Tsubota	4.1m/s	8.0m/s	6.0m/s	12m/s

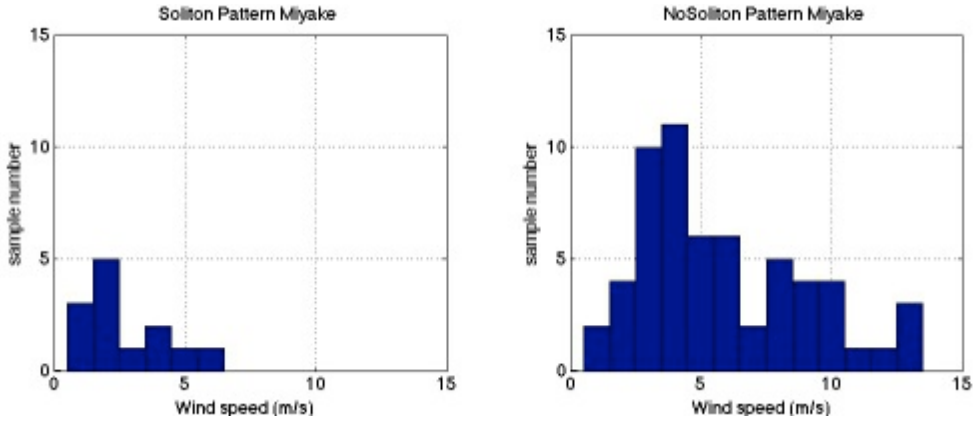

Figure 3.7 Histograms of the hourly averaged wind data from the observation site Miyakejima operated by Japan Meteorology Agency. The left (right) figure shows data for the days when parabola patterns are shown (not shown) in SAR images.

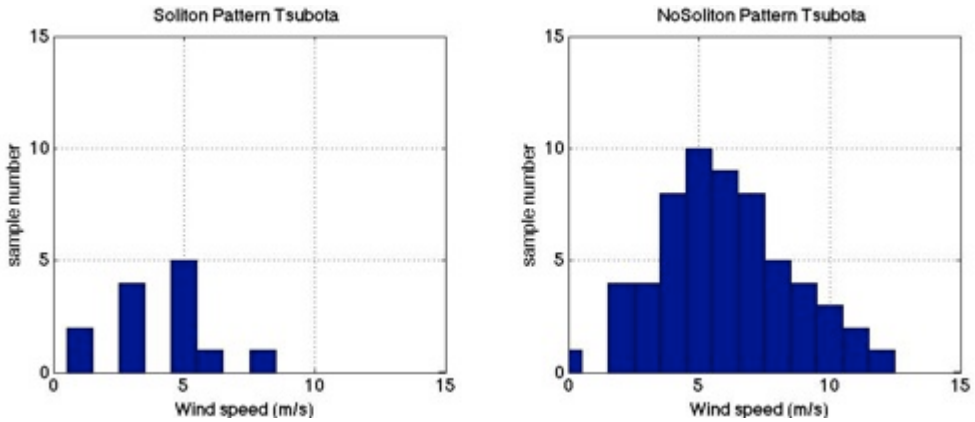

Figure 3.8 Histograms of the hourly averaged wind data from the observation site Miyake-Tsubota operated by Japan Meteorology Agency. The left (right) figure shows data for the days when parabola patterns are shown (not shown) in SAR images.

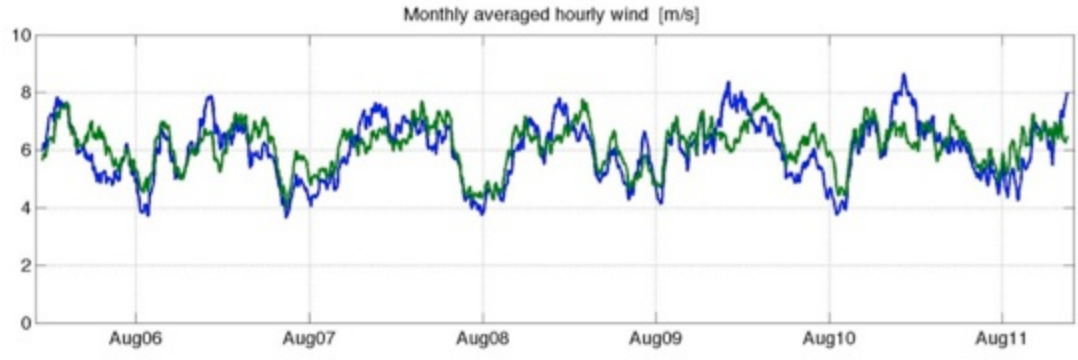

Figure 3.9 Time series of the monthly averaged wind speed measured at stations named Miyakejima (blue line) and Miyake-Tsubota (green line).

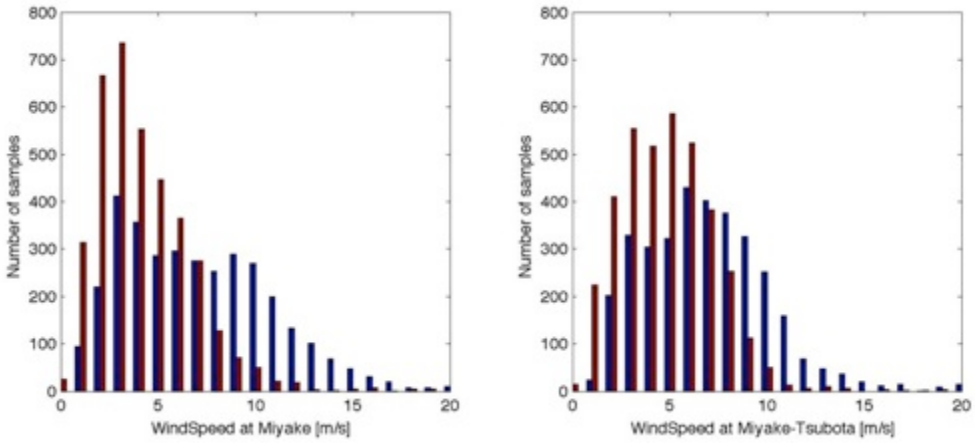

Figure 3.10 Histograms of hourly averaged wind speed measured in February (blue) and August (red) from 2006 to 2011. The left panel is created from the data obtained at Miyakejima and the right panel is from Miyake-Tsubota.

3.1.4 Tide

The other factor is tidal flow, for which in situ tidal gauge measurement at the Miyake Island is available. The tide gauge records for summer in 2006 and 2010 are shown in Figure 3.11 with red markers showing the time when the parabola patterns were detected. Some of the markers located at minimal value of tidal level, but not necessarily. The tidal gauge record does not directly mean the tidal current. The relation between the sea surface height and tidal flow is described later in the subsection 3.2.3. However, we can interpret from the tidal gauge record and the time series of the SAR images obtained that the parabola patterns do not strongly depend on the phase of the tide, neap or spring. Therefore, tidal flow might help internal wave generation and trapping but it is not the main factor.

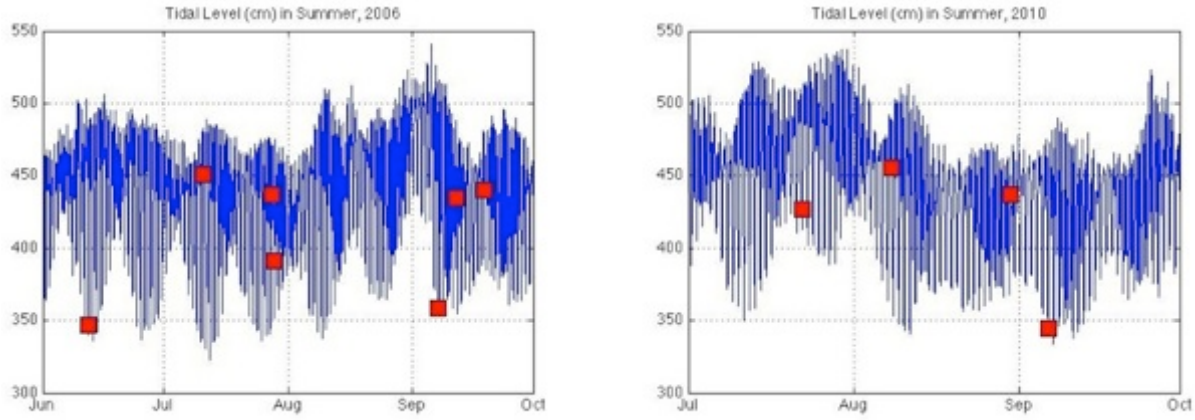

Figure 3.11. Tidal gauge record at the Miyake Island operated by Japan Meteorology Agency.

3.2 Internal Wave Properties Estimated by Ocean Reanalysis Data

The data analysis described above showed that the detection of the parabola patterns requires approach of the Kuroshio and gentle wind. This result convinced us that the parabola patterns in SAR images are manifestations of the oceanic internal waves caused by and trapped by the Kuroshio around the islands. In particular, finite amplitude internal waves may evolve and create a large modulation on the wind wave field if the situation is near critical.

The properties of internal waves depend on the background density and velocity profile. The density profile changes with season, so the surface manifestation of the internal wave may have seasonal variation. There is no long-term in situ measurement providing stratification and velocity profile at the Kuroshio axis, so we make use of ocean reanalysis data to investigate in which season internal waves induce strong surface convergence and estimate which mode of internal wave may be trapped.

3.2.1 Seasonal Variation of Internal Wave Properties

Japan Coastal Ocean Predictability Experiment (JCOPE2) has been conducted by Japan Agency for Marine-Earth Science and Technology (JAMSTEC) and has provided ocean reanalysis data. The product is called as JCOPE2 and the JCOPE2 was created by using Princeton Ocean Model with a generalized coordinate of sigma (POMgcs; Mellor et al., 2002) with data assimilation (Miyazwa et al, 2009). The summary of JCOPE2 used for analysis in this section is described in Table 3.4.

Table 3.4 JCOPE2 Reanalysis Data.

Numerical Domain	(108.0E, 10.5N)- (180.0E, 62.0N)
Simulation Period	1993-2013
Wind forcing	NCEP

Although JCOPE2 is recognized as high-resolution ocean reanalysis data with a spatial grid of 1/12° and 46 vertical levels, it might be still be insufficient to reproduce vertical profiles of the Kuroshio, particularly for the velocity near the islands. Therefore, we traced the Kuroshio axis at longitude 139E as shown in red line in Figure 3.12 (left) and the line is about 0.5 degree latitude west of the Miyake and Mikura Island.

The vertical velocity profile of the Kuroshio axis is assumed to have the same direction over the depth and the profile is obtained by using the magnitude of eastward and northward velocity. Based on this velocity profile, the Kuroshio axis is defined as the location with a maximum flow rate from surface to the -1000m depth. The Kuroshio sometimes moves northward and flows over areas with bottom depth shallower than -1000m, but those data are omitted.

An example of the surface flow field and vertical section of velocity and temperature are shown in Figure 3.12. The Kuroshio axis is shown with orange dashed line in Figure 3.12 (right). The Kuroshio has a width of about 100km and the temperature profile changes from south to north to create a thermal wind structure. We averaged the vertical profiles of the Kuroshio axis for each month from 2006 to 2011 and obtained the monthly profiles. The density is calculated by the International Equation of State 1980 (EOS-80) with potential temperature and practical salinity produced by JCOPE2. Although there is new International Thermodynamic Equation of Seawater 2010 (TEOS-10), we used EOS-80 because of negligible difference and because the EOS-80 is used in the numerical simulation in the next section.

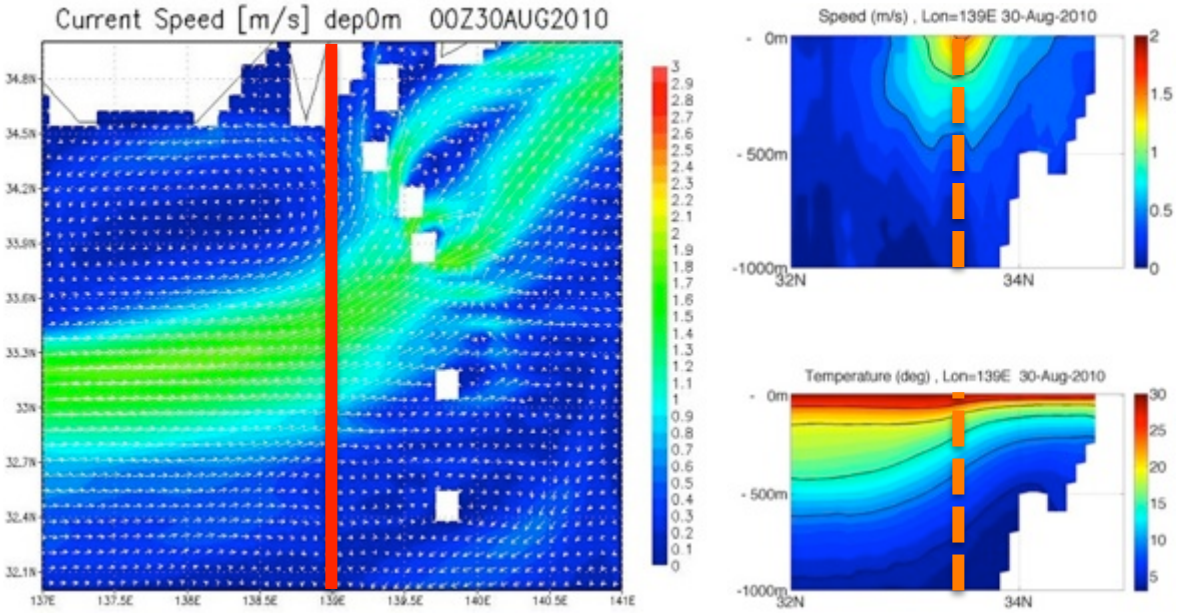

Figure 3.12 An example of the surface velocity field of JCOPE2 reanalysis (left). Right panels show the velocity magnitude and temperature distribution on the vertical section along the longitude 139E.

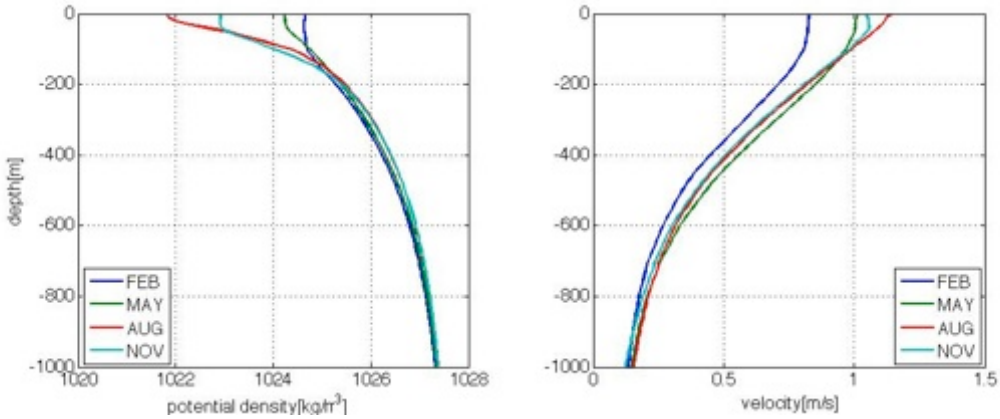

Figure 3.13 Seasonal variation of the density profile (left) and velocity profile (right) of Kuroshio axis.

The density profile of February shows a fully mixed layer below to about -100m, while the one for August has almost no mixed layer (Figure 3.13, left). The two profiles are manifestations of the seasonal variation, which changes internal wave properties significantly. On the other hand, vertical velocity profiles decrease in February compared to the other month (Figure 3.13, right). The reason of the decrease is not further investigated in this study but the decrease might diminish the trapping of internal waves around the islands.

As we described in the subsection 2.3.5, surface velocity convergence induced by internal wave is related to the backscattering field measured by SAR. Three environmental properties, $[(c-u_o)\phi(z)]_z$ at the surface, phase speed c and the coefficient μ' for nonlinear term in

KdV equation are important to determine the magnitude of sea surface velocity convergence that is given by linear theory as

$$u_x = [A(x - ct)]_x[(c - u_o)\phi(z)]_z$$

In this subsection, we analyze the seasonal variation of those three values and also the Froude Number. We focus on the waves that shall be trapped around the islands, so internal wave propagating in an opposing direction to the background flow was analyzed. We define background shear flow as having positive values, so the propagating speed of the wave takes a negative value from the observer moving with the speed of the vertical mean of background shear flow. To make every analysis consistent, one of the waves for each mode with negative value of c is considered in this study even if there is no background shear flow.

At first we neglected the velocity and obtained the solutions of the eigenvalue problems. The solutions are compared with ones including the background velocity to evaluate the effect of background shear flow. As Kuroshio approaches the island, sea bottom becomes shallower because of the topography around island. To consider this situation, we used a part of vertical profiles from surface to particular depth to solve the eigenvalue problem. Figure 3.14 shows the solutions of phase speed, the value of $[(c - u_o)\phi(z)]_z$ and nonlinearity for mode-1 and mode-2 internal wave. The results for each month and each depth from -1000m to -200m were obtained by solving eigen value problem without background shear flow. Both of mode-1 and 2 waves' phase speeds decrease with shallower water depth and in winter since the typical value of Brunt-Vaisala frequency N^2 is proportional to the density difference and inverse of water depth. On the other hand, other quantities depend on the profile of the N^2. The value $[(c - u_o)\phi(z)]_z$ for both of mode-1 and 2 take maximum in summer in terms of its absolute value. The tendency is independent of depth and this means that internal wave is more likely to induce larger surface velocity in summer. The distribution of nonlinearity coefficient μ' for mode-1 shows large magnitude of μ' in summer because thinner mixing layer thickness increase the nonlinearity as knowledge from the theories for two-layer fluids. On the other hand, the distribution of μ' for mode-2 internal wave is complex. The sign changes not only in the year at particular depth but also changes with depth for particular month. The sign of the nonlinear parameter defines the polarity of nonlinear internal wave, so mode-2 can take either positive or negative polarity. However, this means that μ' for mode-2 is sensitive to the density profile.

To check the effect of background velocity, we additionally applied the monthly velocity profile to the eigenvalue problem and conducted the same analysis. For calculation of the properties, only a part of the velocity profile up to particular depth was considered. The results (Figure 3.15) show that inclusion of background velocity modifies the properties from the ones without the velocity (Figure 3.16), but the modulation is not changing the whole distribution. Rather both of the results (Figure 3.15 and Figure 3.16) share the common seasonal variation. The distribution of $[(c - u_o)\phi(z)]_z$ for mode-1 has almost no difference, but the nonlinearity coefficient μ' tends to decrease its magnitude in summer with background shear flow. This implies that background shear discourage the internal waves to have nonlinear character. The distribution of $[(c - u_o)\phi(z)]_z$ for mode-2 has no positive value and the minimal value located in August at every depth. Both the values $[(c - u_o)\phi(z)]_z$ and

μ' for mode-2 waves changes considerably for shallow area in winter season and background shear changes the values to reduce the surface convergence. Froude number is also calculated and both of the mode-1 and 2 can be critical at shallow area. However, this might be overestimating because velocity profile at the 139E is used, while it decreases as approaching the island.

According to the analysis of the internal wave properties estimated by monthly averaged environment configuration, both of the mode-1 and mode-2 took maximal values in summer season. The results support the idea that internal waves are likely to be manifested in summer season.

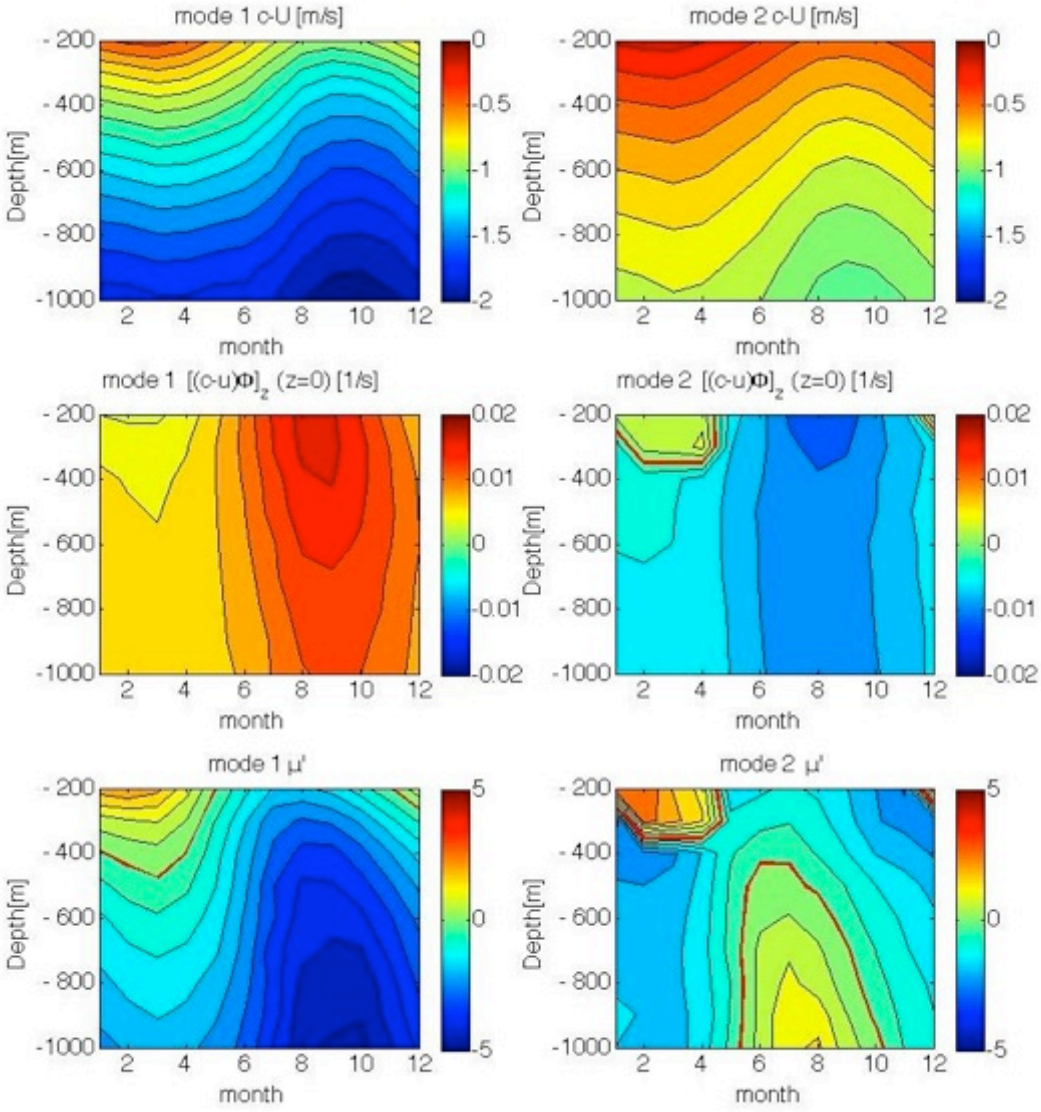

Figure 3.14 Internal wave properties obtained by solving the eigenvalue problem with monthly averaged density profiles of the Kuroshio axis from JCOPE2 ocean reanalysis data. Top panels show the phase speed of the internal wave. The middle panels show values of vertical mode for induced velocity at the surface. The bottom panels show nondimensional coefficient for the nonlinear terms in the KdV equation. Red lines show the contour line of zero in each distribution

.

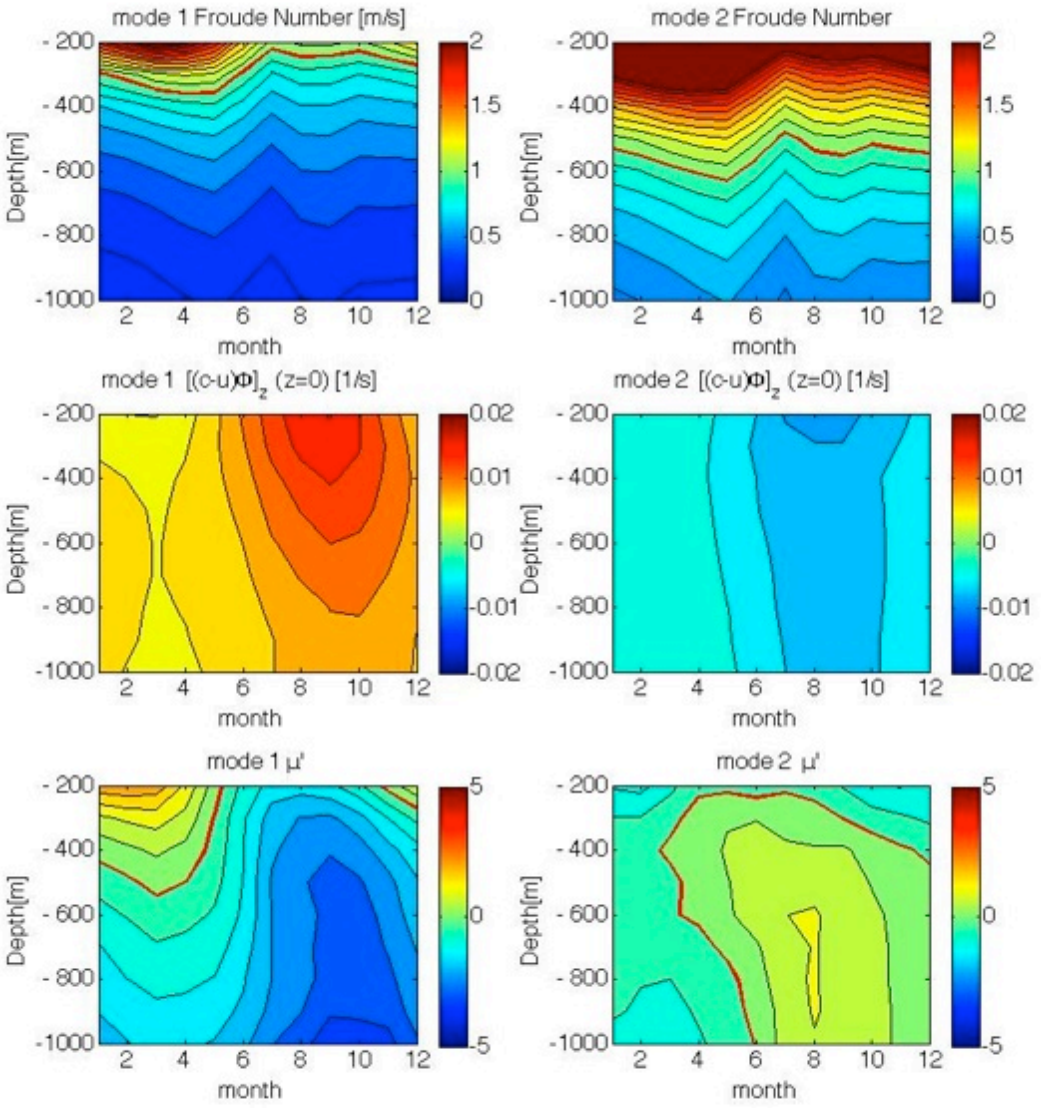

Figure 3.15 Internal wave properties obtained by solving the eigenvalue problems with monthly averaged density and velocity profiles of the Kuroshio axis from JCOPE2 ocean reanalysis data. Top panels show the phase speed of the internal wave. The middle panels show values of vertical mode for induced velocity at the surface. The bottom panels show the nondimensional coefficients for the nonlinear terms in KdV equation. Red lines in the top panel show the contour line of unity in each distribution, while red lines in the other panels show the contour line of zero.

3.2.2 Accuracy of Internal Wave Properties estimated from Ocean Reanalysis Data

To evaluate the accuracy of estimation of internal wave properties from JCOPE2 reanalysis data, we compared the internal wave properties obtained by JCOPE2 and insitu measurement. Monthly variation of vertical profiles and the one for specific point and time were examined as described below.

Japan Oceanographic Data Center (JODC) has published statistical dataset that provide vertical profiles of temperature and salinity around Japan. The area around Japan is decomposed to the squared grid of 1 degree longitude by 1 degree latitude (Figure 3.16) and the statistical dataset is available for each grid. The dataset was created by taking average of insitu observation data from 1903 to 2003. Number of samples used to create the data depends on season and depth. The typical number of the samples is over 100 above the -500m but the number reduces abruptly below it.

The density profile of JODC statistical dataset was used to solve the eigenvalue problem and obtained internal wave properties were shown in Figure 3.17. The results were quite similar to the one obtained with JCOPE2 reanalysis data even the two datasets has difference in creating monthly profiles. This means that monthly variation is much larger than the spatial variation in the area where Kuroshio flows and JCOPE2 can be used to study to seasonal variation of internal waves.

To evaluate the accuracy with smaller temporal and spatial scale, density profile obtained by Argo floats were studied. The 19 profiles measured around Izu-Islands, in the area from (138.5E, 33N) to (139.5E, 34N), from 2006 to 2011 (

Table 3.5) were collected and they are used to obtain internal wave properties. The data was downloaded from the Japan Argo Delayed-mode Data Base operated by JAMSTEC (http://www.jamstec.go.jp/ARGO/_argo_web/search/search.html). From each data, density profile down to -1000m with every 10m is created by interpolation and extrapolation. The extrapolation is done for only two cases whose minimum measurement depth is shallower than -1000m. We set the minimum depth of profiles as -1000m because there is almost no variation below -1000m. Since Argo data does not measure the velocity profile, we neglect the velocity profile $u_{o(z)}$ for this comparison.

The results showed that phase speeds are close in JCOPE2 and Argo, but the coefficient for the nonlinear term μ' does not match well, particularly for mode-2 internal wave (Figure 3.18). From this result, it can be said that the JCOPE2 data can be used to predict which baroclinic long wave the Kuroshio traps around the islands, but the estimated nonlinearity of the internal wave might be different from the real situation.

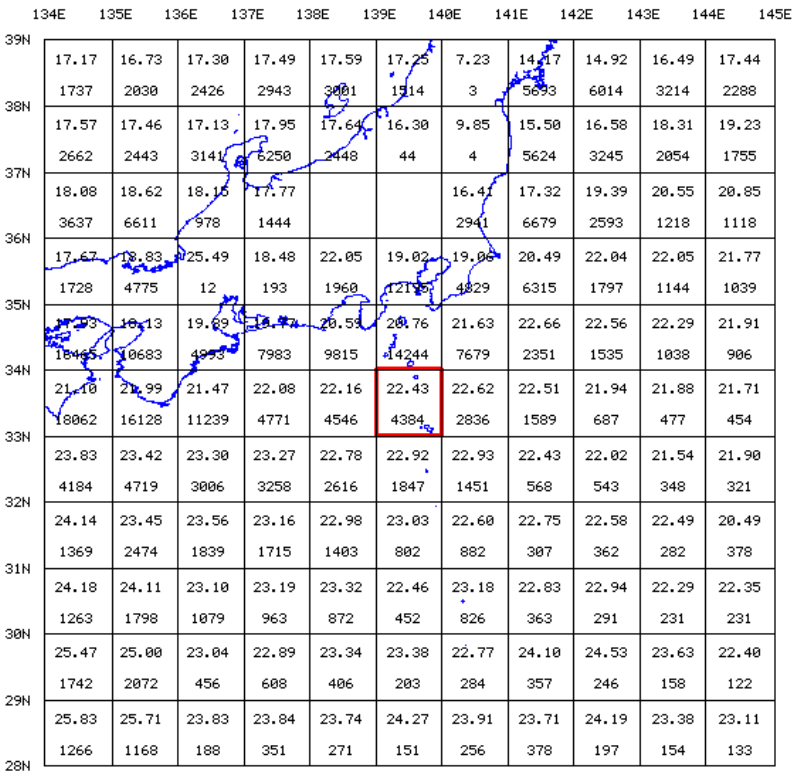

Figure 3.16 Area around Japan divided into grids where JODC statistical data is available.

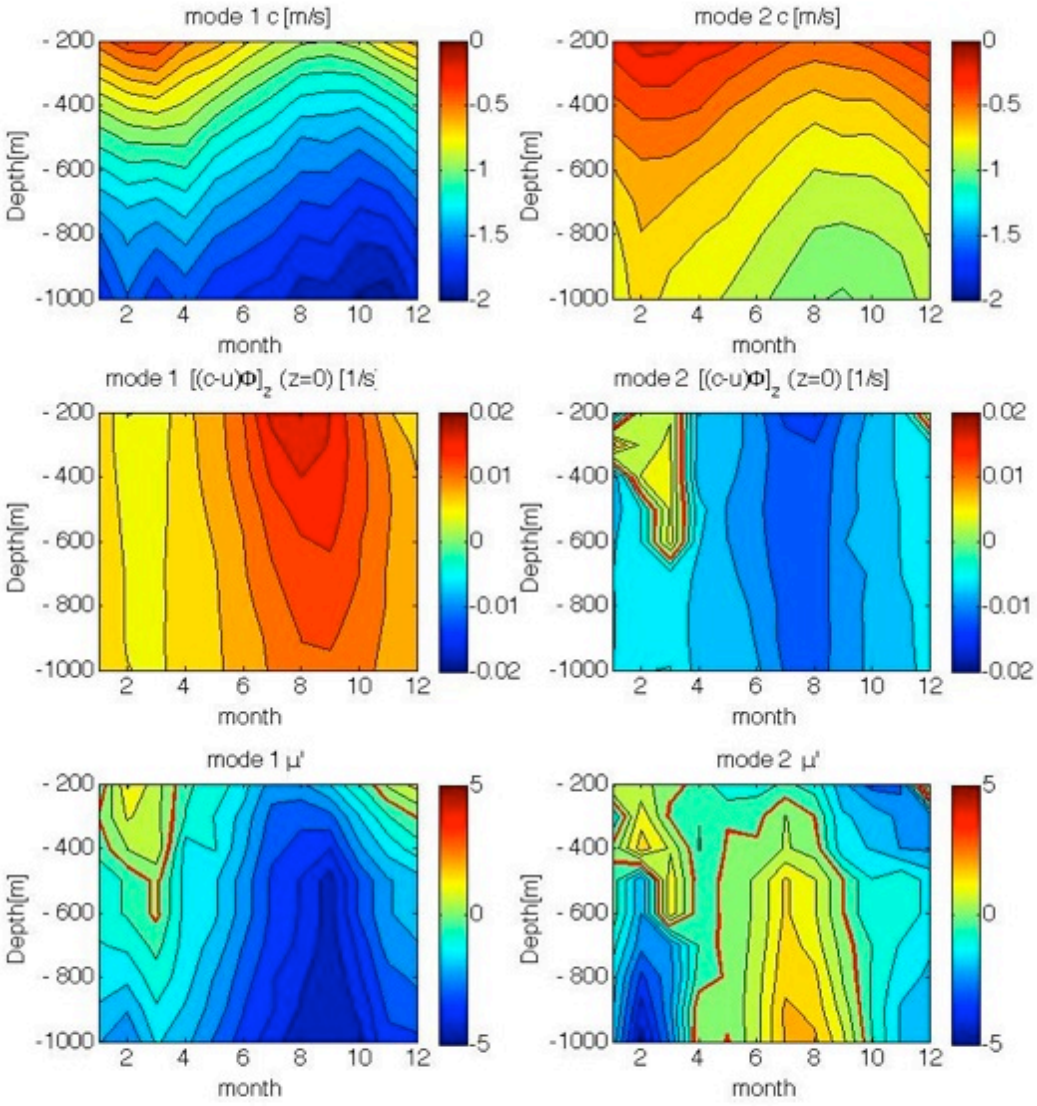

Figure 3.17　Internal wave properties obtained by solving the eigen value problem with JODC statistical data set around Miyake island. Top panels show the phase speed of internal wave. The middle panels show values of vertical mode for induced velocity at surface. The bottom panels show nondimensional coefficient for nonlinear term in KdV equation.　Red lines show the contour line of zero in each distribution.

Table 3.5. Argo floats data used for the comparison with JCOPE2.

	Date	Time	Latitude	Longitude	Layer. No	bottom(dbar)
No.1	2007/4/24	17:37:52	33.067	139.34	62	974.9
No.2	2007/4/29	18:21:49	33.533	138.981	70	1868.4
No.3	2007/5/4	19:07:07	33.565	139.045	68	1699.7
No.4	2007/5/9	19:09:29	33.638	138.831	71	2000.4
No.5	2007/8/12	19:25:29	33.07	138.762	71	1987.7
No.6	2007/8/17	16:30:24	33.18	138.648	61	1178
No.7	2009/4/20	20:18:27	33.461	138.723	73	2013.5
No.8	2009/10/27	10:45:11	33.004	138.535	72	1983.3
No.9	2009/11/1	10:28:48	33.23	138.985	71	1821.6
No.10	2009/11/6	10:13:09	33.451	139.481	70	1793.6
No.11	2010/10/12	13:21:21	33.074	138.751	73	2010.5
No.12	2010/10/17	15:11:28	33.1	139.285	64	1232.6
No.13	2010/10/22	15:39:27	33.384	139.497	64	1210.7
No.14	2010/11/19	2:05:26	33.658	138.948	114	1943.9
No.15	2011/4/16	15:44:11	33.046	139.038	71	1853.1
No.16	2011/7/18	5:26:24	33.257	138.878	95	994.8
No.17	2011/7/28	0:28:03	33.89	139.37	104	1400.5
No.18	2011/11/4	11:11:03	33.812	139.4	56	1699.2
No.19	2011/12/29	3:38:27	33.984	139.084	59	1136

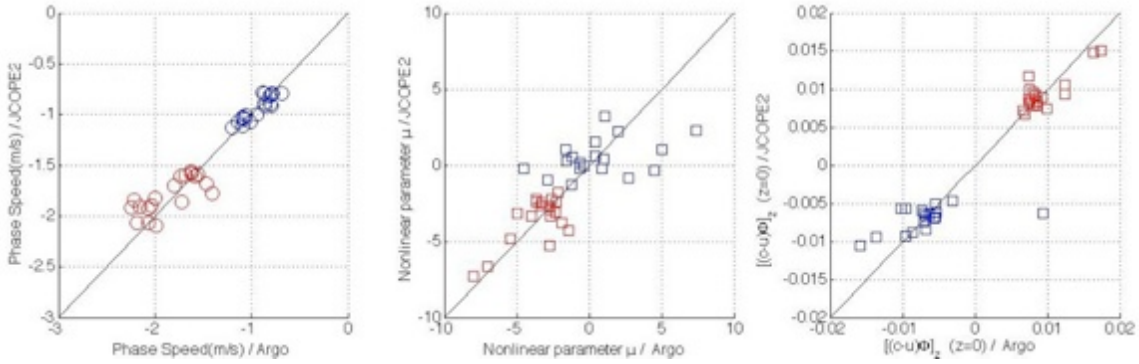

Figure 3.18 Comparison of the estimated baroclinic phase speed(left), nonlinear coefficient μ' (center) and dispersion coefficient $[(c-u_o)\phi(z)]_z$ (right) by solving the eigen value problem with density profile of Argo and JCOPE2. Mode-1 and mode-2 are shown in red and blue symbols.

3.2.3 Criticality of each Mode and Effect of Tidal Flow

Since phase speed of baroclinic waves can be well estimated by ocean reanalysis data, daily fluctuation was further analyzed with JCOPE2 to determine which mode was trapped. The mean velocity of the Kuroshio axis at 139E longitude and the intensity of vertical shear $du_{o(z)}/dz$ were calculated and found that SAR images were obtained when both of the values are relatively large (Figure 3.19, left). On the other hands, there is no such a tendency for phase speed (Figure 3.19, right). The phase speed is calculated by including background shear flow. A black line in the Figure 3.19(right) indicates the situation of exactly critical and the figure tells that mode-1 is far from critical but the mode-2 is likely to be critical.

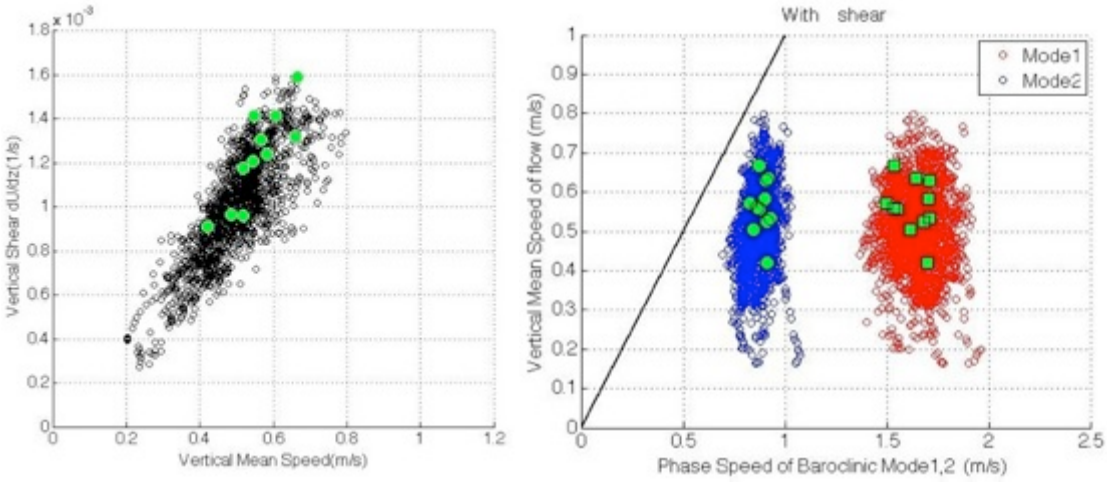

Figure 3.19 Scatter plot of the vertical mean speed of the Kuroshio axis and the intensity of its shear (left). Scatter plot of propagating speed of each mode from the observer moving with vertically averaged background flow speed and the vertical mean speed of flow(right). The black line in the right panel shows the critical situation.

To investigate how the Froude Number changes with location around the island and evaluate influence of tidal flow, we referred to the higher resolution reanalysis data named sbPOM (Sil, et al. 2013). Tide is resolved by using tidal model NAO99 (Matsumoto, 2000). Since the simulation period is from June 2011 to July 2012, it is not overlapped with the period of PALSAR, so the data cannot provides the oceanic information when the PALSAR obtained the SAR images. However, we can estimate how the Froude Number changes with position and tidal flow.

We chose July 2012 for the analysis because Kuroshio had approached Miyake and Mikura Islands (Figure 3.20). The Kuroshio axis past the two locations, (139.00E, 33.80N) and (139.40E, 34.00N), the flow direction is east-northeast. Since the direction of the tidal flow changes with time, we focus on the component of the velocity parallel to east-northeast. The component V_{ENE} is simply calculated as follows.

$$V_{ENE} = u * \cos(\pi/6) + v * \sin(\pi/6)$$

where u and v are eastward and northward velocity.

We checked effect of topography with the monthly mean profile of V_{ENE} for 6 positions upstream Kuroshio shown in Figure 3.22. Although the tidal flow may create the residual current, monthly averaging should filter out the dominant component of the tidal flow and

only the component of the Kuroshio can be left. We name each location with station 1 to 6 from west to east. As the flow approaches the island, velocity tends to decrease at each depth but the difference is subtle until the flow past the station 4. Table 3.6 shows the vertical mean velocity value and the phase speed for mode-1 and 2 calculated by using the monthly averaged density profile and velocity profile at each Station. Density profile did not change between Stations within a month, but bottom depth decreases after passing the Station 4, so phase speed of each mode decreases. This is consistent to the observational fact that trapped internal wave signatures were detected around the island with shallow topography.

Table 3.6 Verical mean velocity of the flow and the phase speed of internal waves calculated by solving the eigen value problem at each station.

Station	1	2	3	4	5	6
Vertical Mean Velocity	0.453	0.470	0.446	0.383	0.563	0.457
Phase speed of mode−1	−1.541	−1.547	−1.522	−1.505	−1.203	−1.085
Phase speed of mode−2	−0.874	−0.872	−0.865	−0.866	−0.697	−0.621

Next, the effect of tidal flow was checked. Since the tide was included in the ocean reanalysis data sbPOM, velocity distribution changed within a day (Figure 3.21). We chose the station 4 and 6 shown in blue and red mark in Figure 3.21 to evaluate the effect of tidal flow further. Figure 3.22 shows the temporal variations of V_{ENE} at the two locations and surface velocity varied much larger than ones for vertical mean. This means that surface tide did not only changes the vertical mean velocity but also created baroclinic component because of the topography around the island.

Although the data record was only for a month and number of data was small (248 data for the July 2012), we conducted Discrete Fourier Transformation and found that semidiurnal variation was dominant. The amplitude of the surface velocity variation was almost double compared to the one for vertical mean velocity as shown in Figure 3.22(bottom). The results of Fourier analysis showed that amplitude of the fluctuation was at most 0.2m/s, so the contribution from tide to the east-northeastward velocity was roughly half of Kuroshio. However, tidal flow changes from neap to spring tide and the contribution of Tide to the velocity was comparable in the spring tide period in July 2012 (Figure 3.23, top).

We calculated the propagating speed of the each mode and found that the mode-2 becomes critical near the island when the Tidal flow accelerated the velocity (Figure 3.24). The sbPOM itself did not show the trapped internal mode and the reason should be mainly still insufficient grid resolution for internal waves.

To support the analysis of the tidal gauge data introduced in the subsection 3.1.4, we checked the relation between sea surface height and the velocity V_{ENE}. Time series of vertically averaged V_{ENE} and sea surface height clearly showed negative correlation shown in Figure 3.25 and the correlation value was -0.569. The SAR images containing parabola signature were sometimes obtained when tidal gauge records showed minimal values, so tidal

flow might assist the generation and trapping of the internal wave especially for the spring tide period.

Table 3.7 An overview of the sbPOM ocean reanalysis data.

Numerical Domain	(136E, 30.0N)- (142E, 36.0N)
Simulation Period	2011/6-2012/7
Wind forcing	NCEP
Tidal forcing	NAO99. (Matsumoto et al, 2000.)

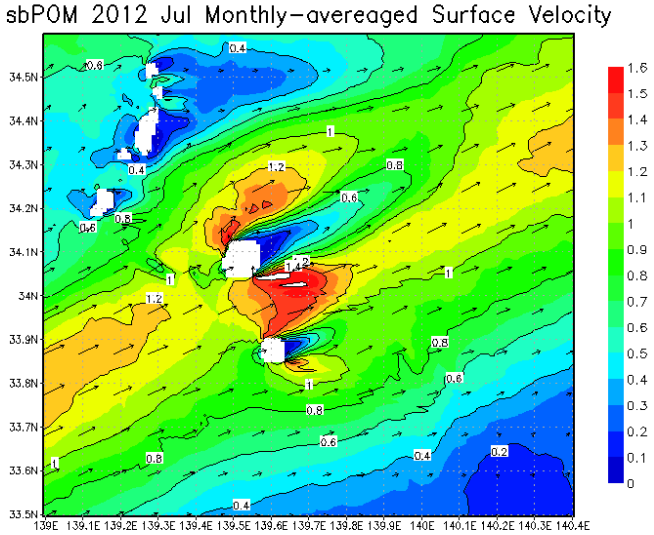

Figure 3.20 Monthly averaged surface velocity distribution around the Miyake Island and the Mikura Island for July 2012.

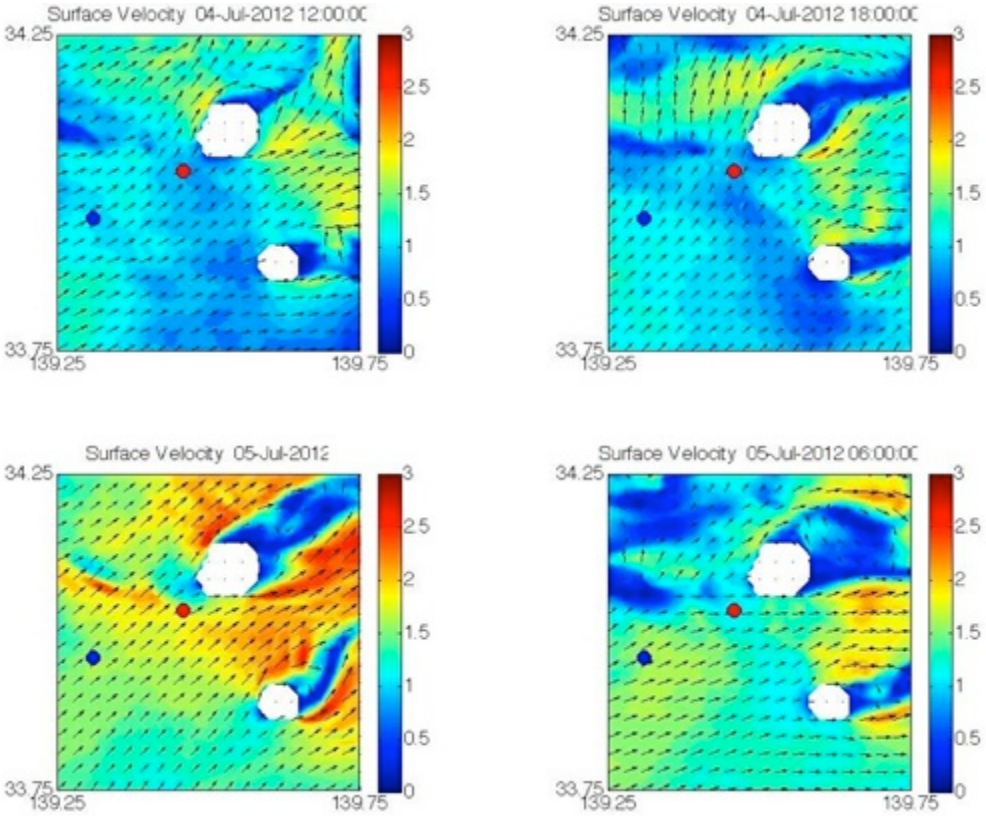

Figure 3.21 Temporal evolution of the surface velocity field in the spring tide period.

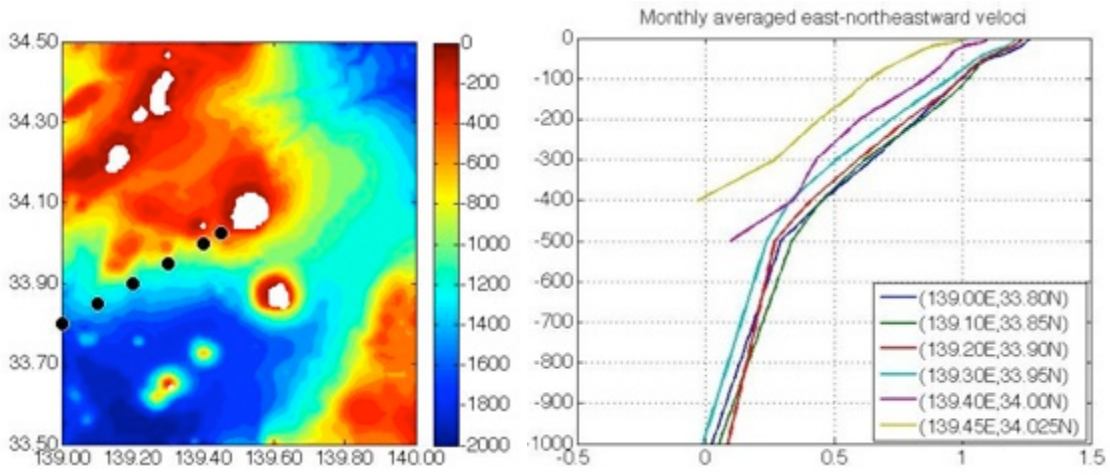

Figure 3.22 Topography around the Miyake Island and black circles are locations chosen for analysis (left). Monthly mean vertical profiles of east-northeast velocity at the locations (right).

Table 3.8 Effect of tide for the vertically averaged V_{ENE} at each station.

Station	1	2	3	4	5	6
Monthly Mean	0.453	0.470	0.446	0.383	0.563	0.457
Maximum value	0.676	0.701	0.674	0.622	0.948	0.887
Standard Deviation	0.108	0.100	0.107	0.094	0.144	0.143

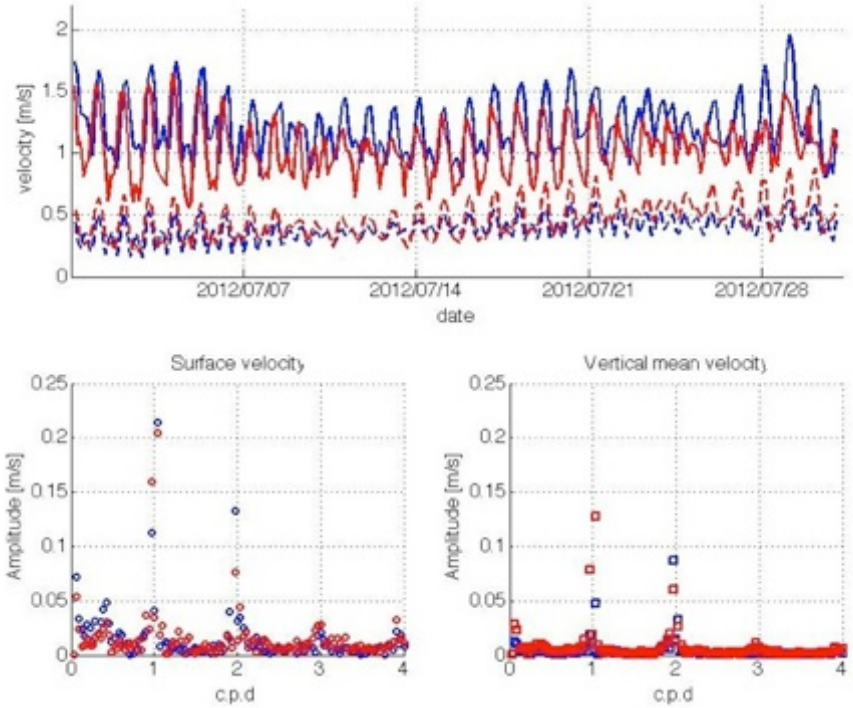

Figure 3.23 Top panel shows time series of the surface (solid line) and vertical mean values of east-northeast velocity component V_{ENE}. Red lines and blue lines are for locations (139.30E, 33.95N) and (139.45E, 34.025N), respectively. Bottom panel shows the amplitude spectral of the surface (left) and vertical mean velocity (right).

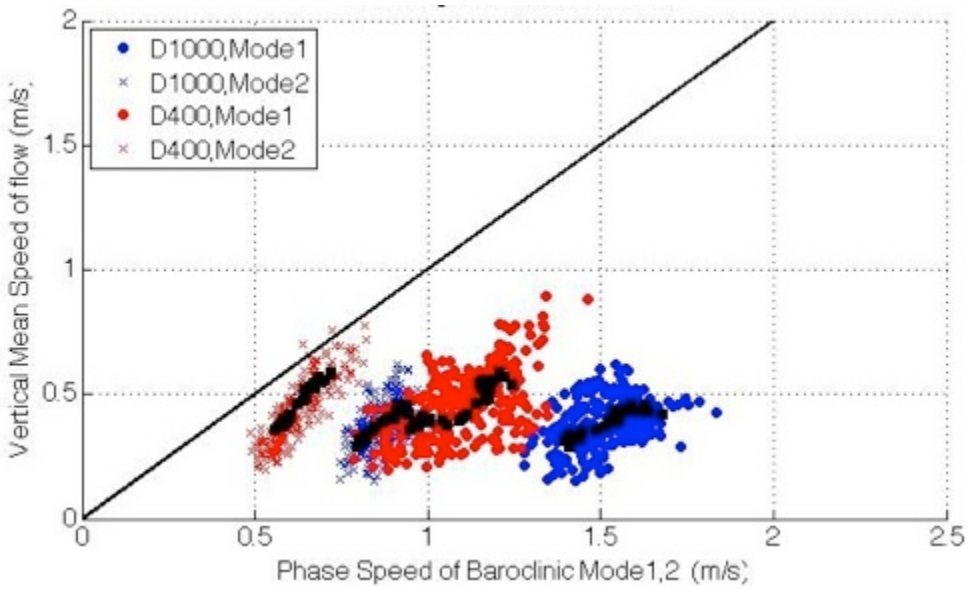

Figure 3.24　Scatter plot for phase speed in the frame of the reference of the observer moving with the speed of background vertical mean flow and the vertical mean flow speed for station 4 (red marks) and station 6 (blue marks). Black points are solutions of the daily averaged vertical profile.

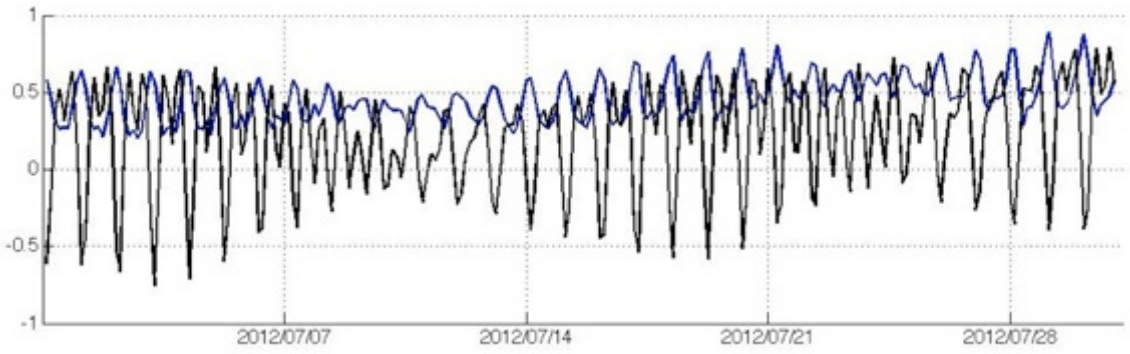

Figure 3.25　Time series for vertically averaged V_{ENE} [m/s] (blue line) and sea surface height [m] (black) at (139.45E, 34.025N) near Miyake Island.

3.3　Field Observation around the Izu-Islands

One of the SAR images including parabola pattern was obtained just before our field observation around the Miyake Island conducted from 30th in August 2010 to 2nd in September. Vertical profile of the flow was continuously acquired by Acoustic Doppler Current Profiler (ADCP) during the observation. In addition to the water velocity, vertical profiles of temperature and salinity were acquired with Conductivity Temperature Depth (CTD) profiler at 11 locations in total. The ship routes of ADCP observation and CTD cast points are shown in Figure 3.26.

The result of ADCP observation was described in Kodaira et al (2013) in detail, but here one thing should be pointed out in the context of the comparison between the field observation results and flow field reproduced in JCOPE2 data reanalysis. The ADCP (Teledyne RDI

Workhorse 300 kHz) was mounted on the side of a fishing boat hull and measured a velocity profile from the surface to 100-m depth at 4-minute intervals. The Global Positioning System (GPS) was used to estimate the absolute ship speed. The 2.5-s sampling rate corresponds to about 5 m in horizontal resolution with a constant ground speed of 2.5 m/s; the actual distance depends on both current speed and direction.

A 30-s moving average was applied on the collected data to remove the noises due to ship motion. In addition, the data were averaged for 0.02° by 0.02° bins each day. Typically, each bin contains 20 records. We conducted the measurement in the area west to the Miyake Island for first two days. The measured horizontal velocity distribution showed the large surface velocity that indicates approach of the Kuroshio during the observation period. As described in Kodaira et al (2013), forecast of the JCOPE2 and time series of the sea surface height support the approach of the Kuroshio. The velocity field near surface in each day had considerable difference. The surface velocity reached 2.5m/s in the second day, while the velocity was at most 1.5m/s in the first day (Figure 3.27). This significant variation is not resolved in JCOPE2 (Figure 3.28). The cause of the variation is not clear whether the tidal flow or the daily variation of the Kuroshio itself. However, it is clear that there was significant daily variation in velocity field around the Miyake Island.

The CTD measurement was made from the surface to about 100m below sea level. The CTD samples were taken while both ascending and descending. First, whole records were averaged in every 2m and a 6m moving point average was applied. Although the rope was 100m long, the observed maximum depth was shallower than 100m because of current-induce drift of the sensor. Locations of the measurement and the obtained profiles of density are shown in Figure 3.29.

Results of the measurement revealed density changes significantly only in the 100m below sea surface and seasonal thermoclines located around -40m were observed in several profiles. Compared to the profiles obtained in the lee side of the island (Figure 3.29, left bottom), ones obtained in the upstream side differs from each other. In addition, density profiles in the lee side indicates that interface was lifted up as the flow past over the topography around the Miyake Island. This implies that density structure of the stratified shear flow past the Izu-islands significantly depends on the path to approaches the island.

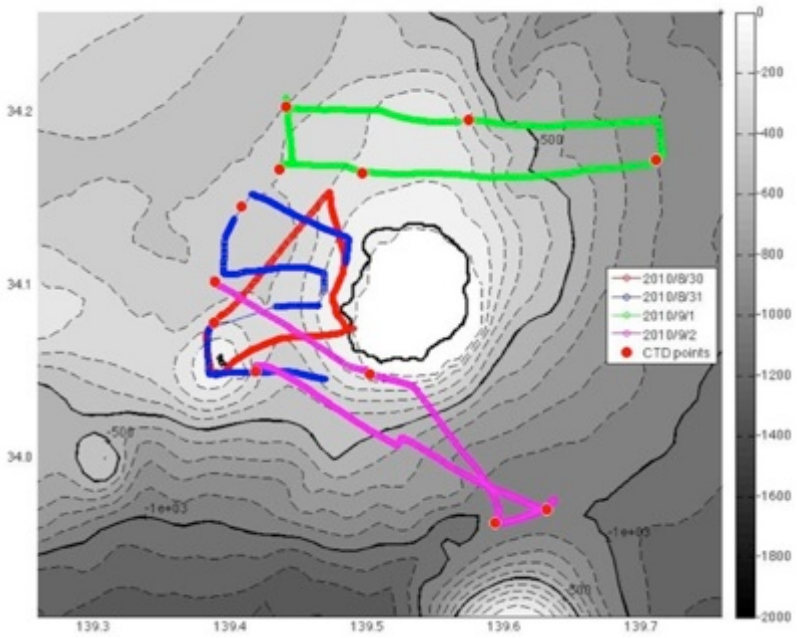

Figure 3.26　Ship routes of ADCP observation and CTD cast points.

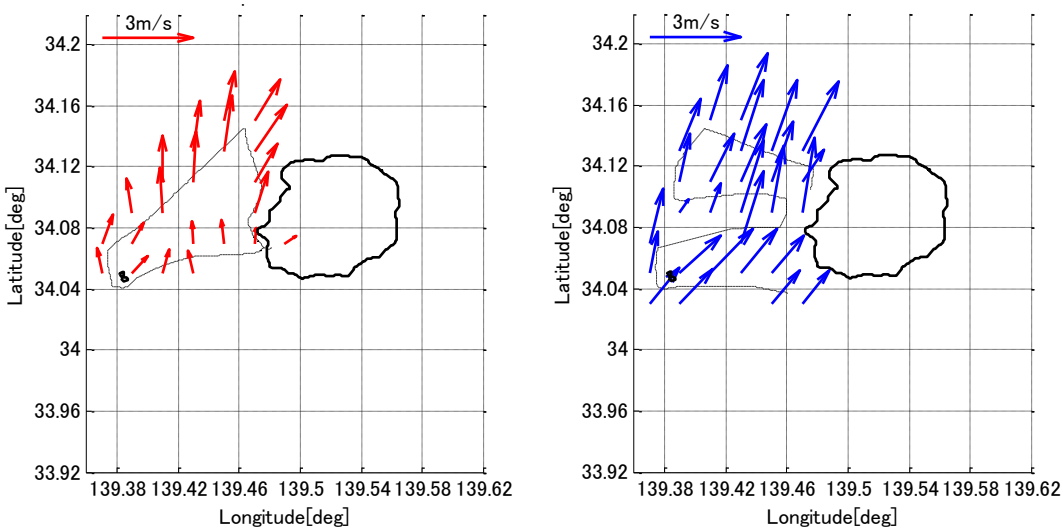

Figure 3.27　Horizontal velocity distribution at -7.2m depth as a results of observation of 30th.Aug.2010 (left) and 31st.Aug.2010 (right).

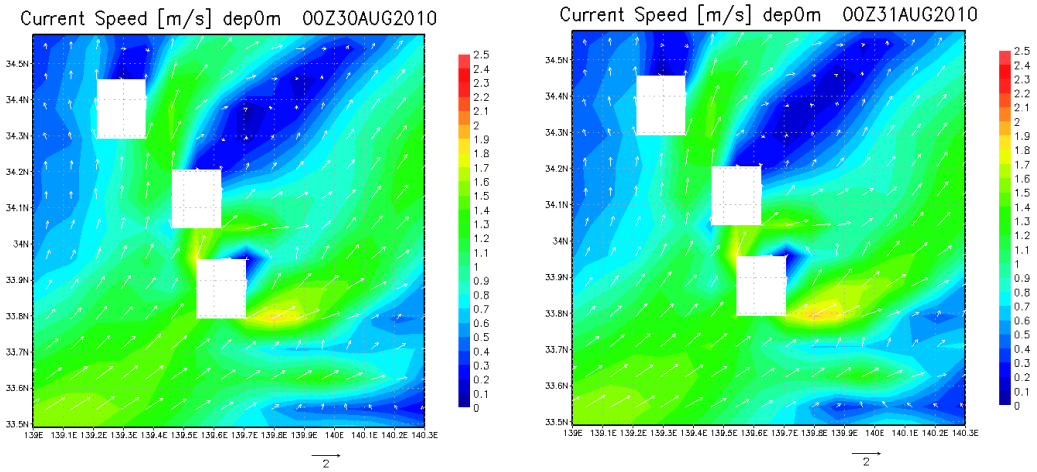

Figure 3.28　Surface velocity distribution around the Miyake Island reproduced in JCOPE2.

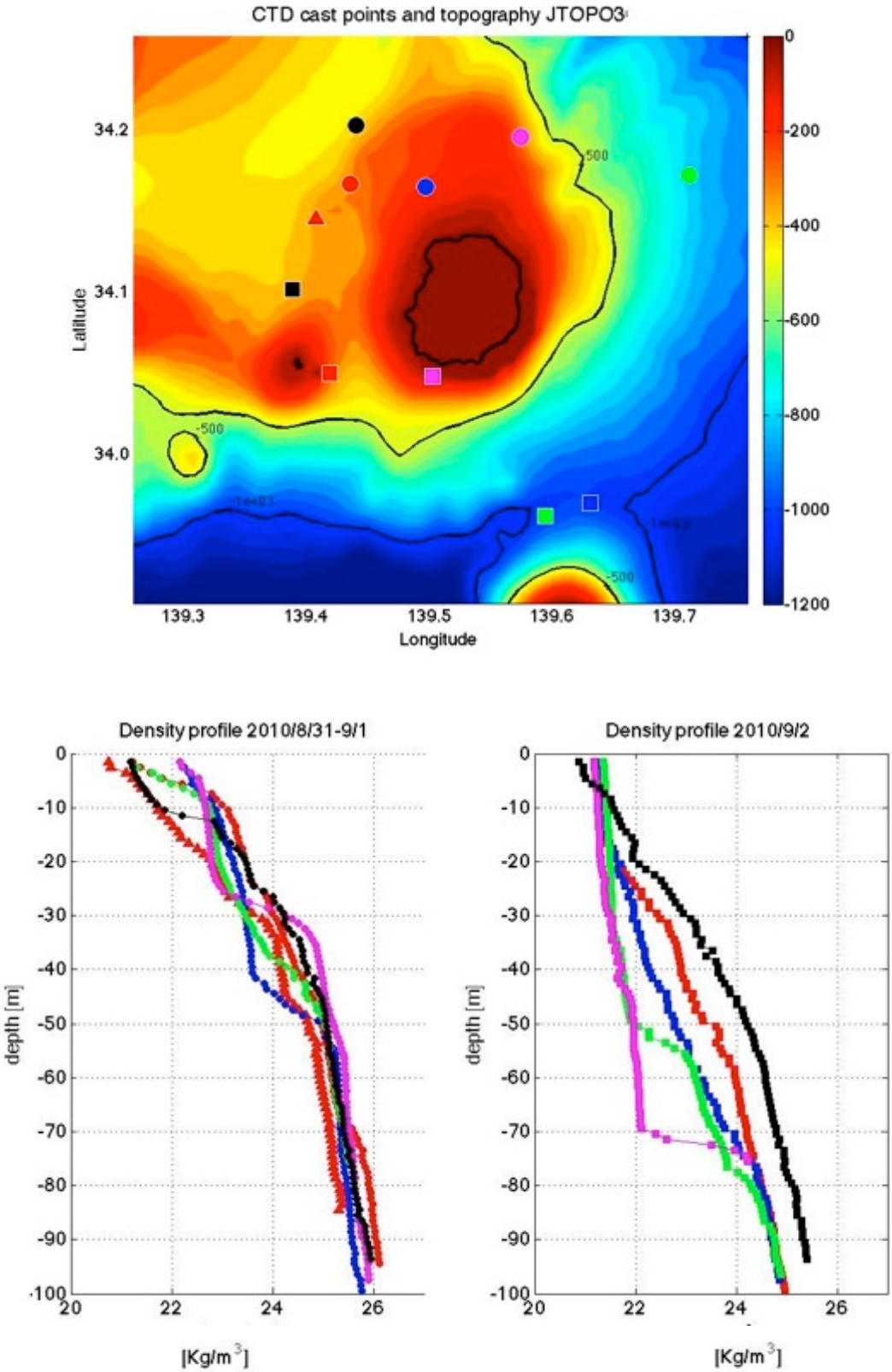

Figure 3.29 Topography around Miyake Island and CTD cast points (top). Obtained vertical profiles are shown in the bottom two panels with marks related to the measurement points.

3.4 Discussion and Summary

We collected SAR images with parabolic patterns off the Miyake and Mikura Islands. The patterns were visible in 13 of the 138 days in images published from 2006 to 2011. Images were taken which fit two criteria: (1) when the Kuroshio approached the island based on the distance between the Miyake Island and the Kuroshio axis as reported by QBOC, and (2) when the in situ wind measurements showed a small value (no more than 8m/s). For some cases, the picture was taken when the tidal gauge record was at a minimum value, but this condition was not necessary. These results indicated that the Kuroshio is central in creating the parabolic surface signatures around the islands that are detected by SAR.

The historical fact that the parabolic patterns were detected only when the Kuroshio approached suggests that these patterns are a manifestation of the internal waves trapped by the Kuroshio. Since almost all of the SAR images with parabolic patterns were taken in the summer season, seasonal variability of internal waves can be related to the detection of the parabolic patterns by SAR. To validate this idea, seasonal variation of the internal wave properties at the Kuroshio axis along 139° E is examined with JCOPE2 ocean reanalysis data. As a result, absolute values of $[(c-u_o)\phi(z)]_z$ and μ' were maximal in the summer season. This indicates that internal waves likely to induce large magnitude of surface velocity convergence in the summer. The lines showing critical situation in Figure 3.15 indicate that trapping of internal wave does not strongly depend on the season. This implies that internal waves are trapped around the island all the year, but they are not detected by SAR in winter because of the smaller surface convergence induced by internal waves and relatively strong wind.

The area-averaged statistical dataset from JODC for temperature and salinity profile made from a large number of observations were also used to estimate the internal wave properties around the islands. The distributions of each internal wave property were similar to those calculated with JCOPE2 data, which indicates that monthly variation was larger than spatial variation around the Izu-ridge. The comparison between the properties calculated with JCOPE2 data and Argo float data was also conducted to evaluate the accuracy of the estimation in daily profile reproduced in JCOPE2. The results showed that internal wave properties were well estimated with JCOPE2 data except for the value of μ' for mode-2 internal waves.

Since the estimated phase speed from the ocean reanalysis data was reliable, criticality of each mode around the island was estimated by analyzing sbPOM ocean reanalysis data. The attention was focused on the velocity field during July 2012 when the Kuroshio was around the Miyake and Mikura Island. The results showed that mode-2 waves become critical with tidal flow at the location where bottom depth is -400 m. The tidal flow induced considerable temporal variation of the flow velocity around the Island, and, at a maximum, doubles the daily mean value flow speed. The field observations also clarified that daily variation of the flow field is significant. Since the density profile changes significantly around the island and the daily variation of the flow field is large, the critical situation for mode-1 internal waves is not denied and warrants further observational studies.

Chapter 4 Numerical Simulation of Stratified Shear Flow past the Izu-Islands.

The results of data analysis in previous sections imply the presence of oceanic internal waves trapped by the Kuroshio around the Izu-Islands. In this chapter, we reproduce the trapped internal waves by numerical simulation. Downscaling of the JCOPE2 is possible, but our interest is mainly in the dynamics of the flow around the islands and possible three-dimensional nonlinear internal waves. Therefore we make simplifications regarding the flow of the Kuroshio past the Izu-Islands and investigate the dynamics.

4.1 Numerical Model MITgcm and Simulation Method

Numerical simulation was carried out using the Massachusetts Institute of Technology General Circulation Model (MITgcm, Marshall et al., 1997). Since hydrostatic approximation precludes wave dispersion and cannot reproduce internal solitary wave correctly, we make use of the non-hydrostatic capacity of MITgcm.

The governing equations are given by (4.1)-(4.6) with incompressibility and Boussinesq approximations applied.

$$\frac{D\boldsymbol{u}}{Dt} + (2\boldsymbol{\Omega}\times\boldsymbol{u})_h + \frac{1}{\rho_c}\nabla_h p = A_h\boldsymbol{\nabla_h}^2\boldsymbol{u} + A_z\frac{\partial^2\boldsymbol{u}}{\partial z^2} \tag{4.1}$$

$$\frac{Dw}{Dt} + (2\boldsymbol{\Omega}\times w) + \frac{1}{\rho_c}\frac{\partial p}{\partial z} + \frac{g}{\rho_c}(\rho-\rho_c) = A_h\boldsymbol{\nabla_h}^2 w + A_z\frac{\partial^2 w}{\partial z^2} \tag{4.2}$$

$$\boldsymbol{\nabla_h}\boldsymbol{u} + \frac{\partial w}{\partial z} = 0 \tag{4.3}$$

$$\frac{D\theta}{Dt} = K_h\boldsymbol{\nabla_h}^2\theta + K_z\frac{\partial^2\theta}{\partial z^2} \tag{4.4}$$

$$\frac{DS}{Dt} = K_h\boldsymbol{\nabla_h}^2 S + K_z\frac{\partial^2 S}{\partial z^2} \tag{4.5}$$

$$\rho = \rho(\theta, S, z) \tag{4.6}$$

where $\boldsymbol{u}$ is horizontal velocity vector, $\boldsymbol{\Omega}$ is background rotation vector, p is pressure, w is vertical velocity, ρ is density perturbation , θ is potential temperature and S is salinity and $\boldsymbol{\nabla_h}$ is space derivative operator for horizontal direction. Other coefficients are set as described below. The first two equations (4.1)-(4.2) are momentum equations for horizontal and vertical velocity, respectively. The third equation (4.3) is continuity equation. The fourth (4.4) and fifth (4.5) are diffusion equation for potential temperature and salinity. The final equation (4.6) is the equation of state. For the equation of state, a modified UNESCO formula by Jackett and McDougall (1995) was used. Potential temperature was set as the input variable in the modified equation instead of in situ temperature.

The governing equations are solved numerically by using a finite volume method in space and second order Adams Bashforth scheme in time. The finite volume method enabled the model to include the effects of arbitrary topography and included shaved or lopped cells. In

addition, finite volume method used non-linear interpolation that enabled non-smooth solutions, such as shocks, to be produced in the numerical calculation.

For the grid arrangement, an Arakawa C grid was used (Arakawa and Lamb, 1977). The southwest corner of the numerical domain corresponds to the location of 139.5° E, 33.5° N. From the southwest to northeast, a numerical domain of 120 km by 120 km was constructed by interpolating JTOPO 30 topography dataset (Figure 4.1). Since the internal wave pattern was detected only in the shallow area around the islands, the topography is modified so that the minimum bathymetry is -1000 m. The horizontal grid spacing was about 200 m and the vertical grid spacing was 10 m for upper 200 m and 20 m for the rest.

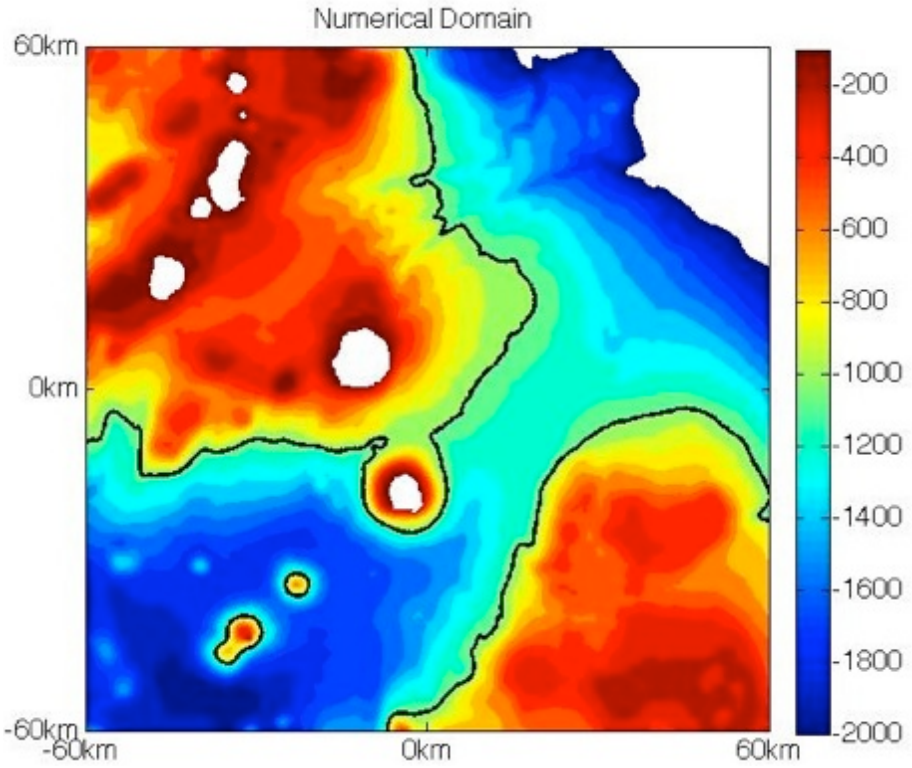

Figure 4.1 Numerical domain, black line shows -1000 m isobar. Lands and areas whose bottom depth is deeper that -2000 m are colored in white.

We simplified the Kuroshio as a stratified shear flow of 100 km width and neglected the Coriolis effect. Since the Coriolis parameter was set to zero, the background stratified shear flow did not have a thermal wind structure, so the temperature and salinity distributions for initial and boundary conditions were horizontally uniform. These were given by $\theta_{bc}(z)$ and $s_{bc}(z)$. On the other hand, velocity was only set within about 100 km width following equation.

$$u(r,z), v(r,z) = u_{bc}(z) * \sin(\pi/4) * \left(1 - \tanh\left(\frac{|r| - 50 * 10^3}{15 * 10^3}\right)\right)/2 \quad (4.7)$$

where conventionally $u(r,z)$, $v(r,z)$ are the velocity components for eastward and northward, respectively, $u_{bc}(z)$ is vertical profile for center of the set stratified shear flow, r is the distance from the diagonal line connecting south-western edge and north-eastern edge of the numerical domain. Therefore, we artificially set the stratified shear flow assuming the Kuroshio passed both of the Miyake and Mikura Islands. The vertical profiles of stratification

of $\theta_{bc}(z)$, $s_{bc}(z)$, and velocity, $u_{bc}(z)$, were the main controlling parameters in this numerical study. These profiles are described later.

The initial distribution of the vertical velocity, w, was specified to satisfy the continuity equation and created the large free surface disturbance. The disturbance remained for roughly half a day in the numerical domain. To avoid this disturbance, we applied rigid lid condition to top boundary for first 10 numerical time steps. This prohibited the surface gravity wave generation in the numerical model and composed potential flow like velocity field (Figure 4.2).

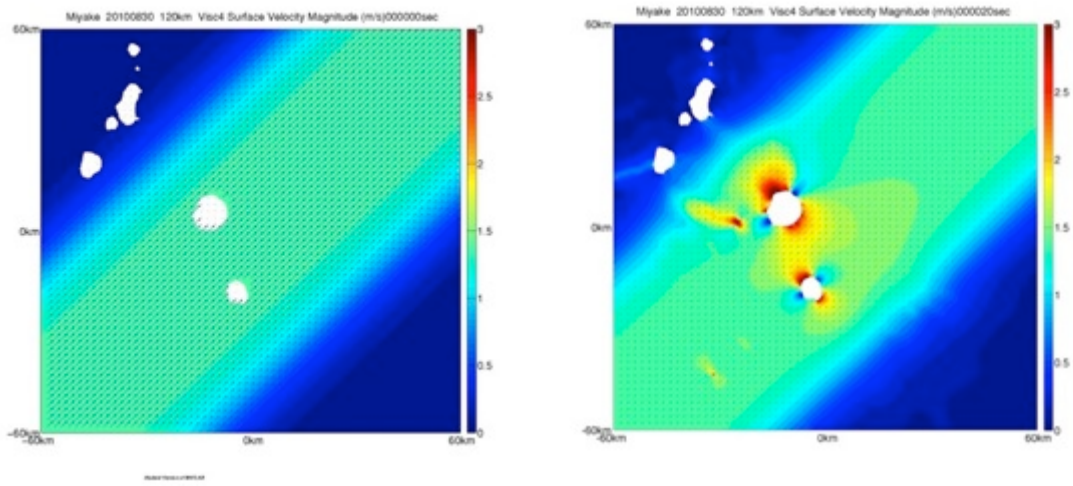

Figure 4.2 Surface velocity field for initial condition (left) and the one after 10 time steps numerically integrated (right). The vertical profiles for $t_{bc}(z)$, $s_{bc}(z)$, and $u_{bc}(z)$ were set from the Kuroshio axis resolved on August 30th, 2010 in the JCOPE2.

Sponge layers of 5 km were added to all the horizontal boundaries, so the variables were relaxed to the boundary values with a relaxation time scale that increases linearly with distance from the boundary

$$G_x = -\frac{x - \{(1-l)x_b + lx\}}{(1-l)\tau_b + l\tau_i}, \quad 0 < l < 1 \tag{4.8}$$

In equation (4.8), x is the model variables, x_b is the boundary value, and l is distance from the boundary normalized by sponge layer thickness. We can tune the relaxation by two parameters τ_i and τ_b, which define the relaxation time scale at the outterior and interior edge of the sponge layer, respectively. We set $\tau_i = 10^3$s and $\tau_b = 10^4$s.

Constant horizontal and Laplacian type vertical eddy viscosity coefficients ($A_h = 25\mathrm{m^2s^{-1}}$, $A_z = 5\times10^{-3}\mathrm{m^2s^{-1}}$) and diffusivity coefficients ($K_h = 2.5\times10^{-1}\mathrm{m^2s^{-1}}$, $K_h = 5\times10^{-4}\mathrm{m^2s^{-1}}$) are set. For the lowest boundary, bottom friction is set by a quadratic friction law with a constant drag coefficient $\mathrm{C_d} = 1\times10^{-3}$.

4.2 Simulation with JCOPE2

Results of the analysis on JCOPE2 data in previous section suggest that mode-2 internal waves are likely to be trapped around the island. Vertical profile of Kuroshio axis reproduced

by JCOPE2 ocean reanalysis data is used for numerical simulation to study oceanic state when SAR images with parabola patterns were obtained.

4.2.1 Selection of the Vertical Profiles for Numerical Simulations

To determine the initial and boundary condition of vertical profiles, we need to specify the $u_{bc}(z)$, $\theta_{bc}(z)$ *and* $s_{bc}(z)$ relevant to the ones for Kuroshio axis. All of the vertical profile for density and the velocity at the Kuroshio axis are shown in Figure 4.3. The density profiles are normalized as follows.

$$\rho_{n(z)} = \left(\rho_{(z)} - \rho_{(0)}\right)/\left(\rho_{(-1000)} - \rho_{(0)}\right) \quad -1000 < z < 0 \tag{4.9}$$

This normalization shows the structure of density profile, which strongly influences on the structure of eigenvalue as described in subsection 2.3.4. Thick lines with various colors in Figure 4.3 show the profiles when SAR images with parabolic pattern were obtained. Days were chosen for numerical simulation from the following viewpoints: a day with (1) the most rapidly changing density profile, (2) the largest vertical mean flow, and (3) the most gradually changing density profile. These three cases were determined to be on 30th/Aug/2010, 27th/Jul/2006, and 16th/Mar/2006, respectively. The density, velocity, temperature, and salinity profiles used for initial and boundary conditions for numerical simulations are shown in Figure 4.4.

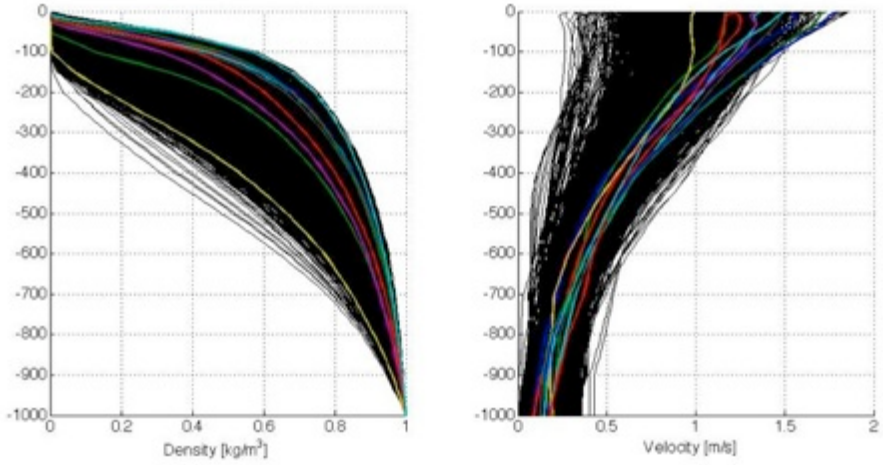

Figure 4.3 Vertical profiles of normalized density (left) and velocity (right) at the Kuroshio axis from JCOPE2 reanalysis. Black lines show profiles of the Kuroshio axis for whole period, while lines with various colors are profiles from the days when SAR images with parabolic patterns were captured.

Table 4.1 Internal wave properties calculated with density and velocity profiles of JCOPE2.

	Mean flow	Froude Number		Nonlinearity μ'		$[(\boldsymbol{c}-\boldsymbol{u_o})\boldsymbol{\phi}(\boldsymbol{z})]_z$	
Date		mode-1	mode-2	mode-1	mode-2	mode-1	mode-2
27th Jul 2006	0.67	0.430	0.760	-2.10	-0.17	0.0067	-0.0039
16th Mar 2008	0.50	0.310	0.595	-1.18	-0.59	0.0054	-0.0028
30th Aug 2010	0.58	0.387	0.700	-2.34	1.00	0.0073	-0.0054

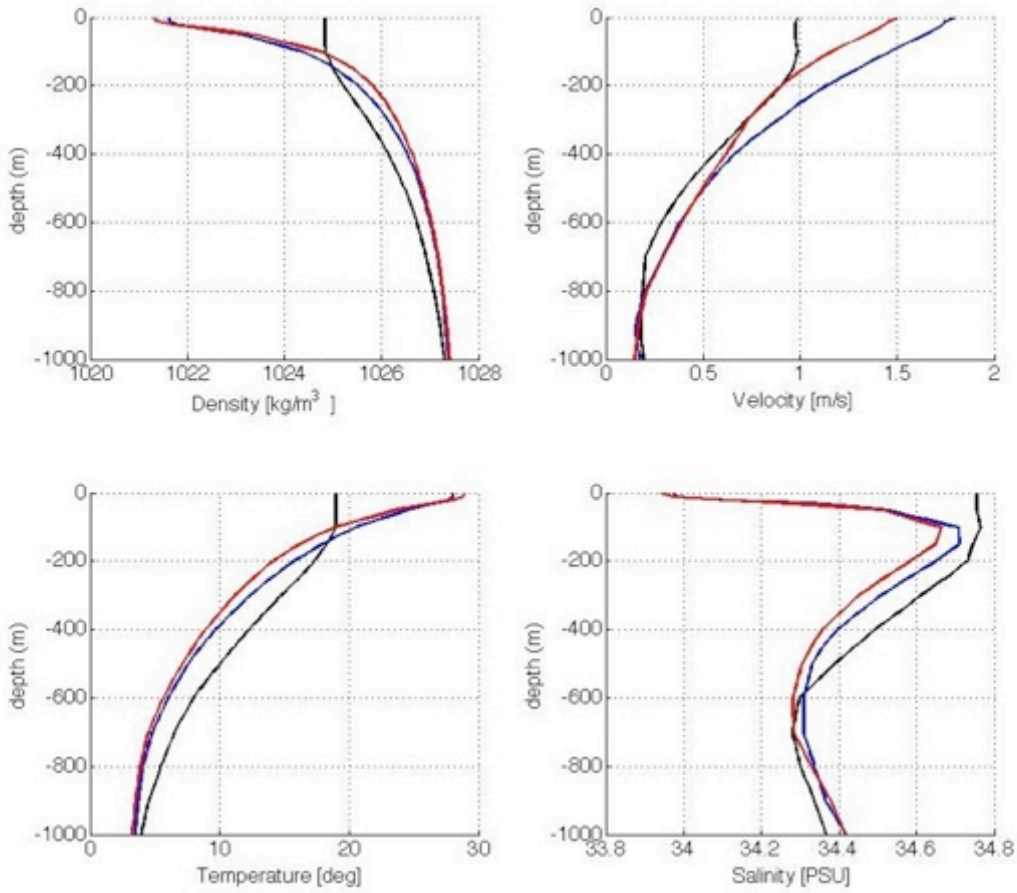

Figure 4.4 Selected vertical profiles for the numerical simulation for 30th/Aug/2010 (red), 27th/Jul/2006 (blue), and 16th/Mar/2008 (black).

4.2.2 Results of Stratified Shear Flow past Izu-islands

The results of numerical simulation with the Kuroshio axis profile on 30th/Aug/2010 showed a steady surface convergence area of parabolic shape upstream of the Kuroshio around the Miyake Island 10 hours after the numerical simulation started. Temporal development of the surface velocity and surface convergence field are shown in Figure 4.5. The surface convergence fields are frequently shown in this study because the values are related to the SAR images as described in subsection 1.1. After the numerical simulation started, the surface velocity forms a distribution similar to the steady irrotational flow around the cylinder in inviscid fluid, but flow separates from the side of the islands and, because of the horizontal no-slip boundary, wakes formed behind the islands.

While eddies were continuously formed and shed from the wakes of both islands, the upstream field changed slightly after 10 hours of time integration. The parabolic pattern remained until the numerical simulation finished after 40 hours. The upstream surface convergence field changed gradually and another parabolic pattern, although small, appeared around the small island west to the Miyake Island (Figure 4.5, bottom).

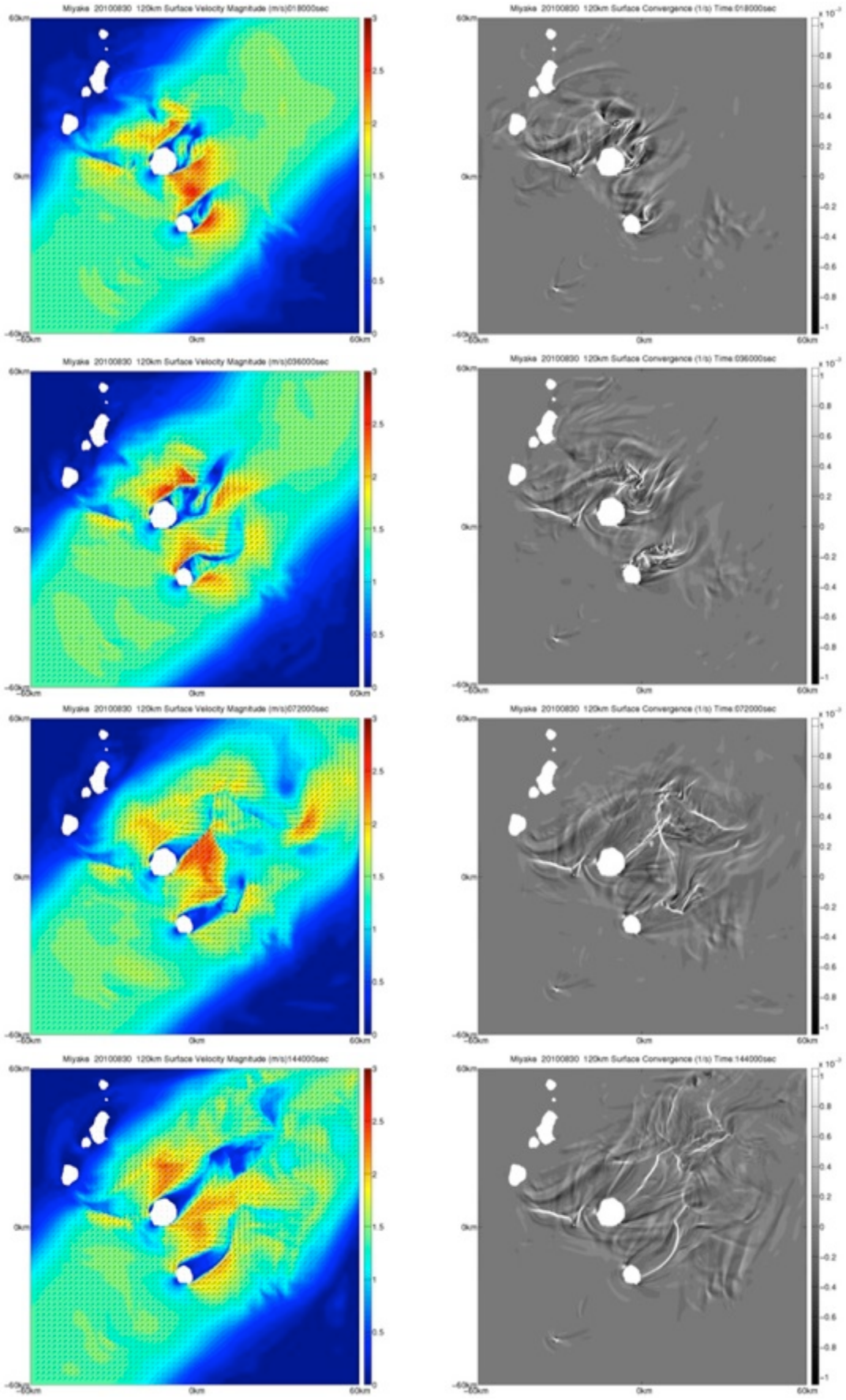

Figure 4.5 Surface distribution of velocity magnitude and convergence at 5, 10, 20 and 40 hours after the simulation started from top to bottom.

The vertical velocity distribution and temperature distribution on the vertical section parallel to the upstream flow showed a trapped mode-2 internal wave around the Miyake Island (Figure 4.6). A recent study (Guo et al, 2012) reported that mode-2 baroclinic internal wave was also manifested in the SAR images. According to their two-dimensional non-hydrostatic numerical simulation for nonlinear internal wave in Luzon strait driven by tidal flow, the surface convergence of order 10^{-4}-10^{-3} was responsible for the pattern shown in SAR images. Since our numerical simulation showed the surface velocity convergence field with same order of intensity, we could conclude that at least mode-2 internal waves were trapped and manifested in the SAR images around the Izu-Islands.

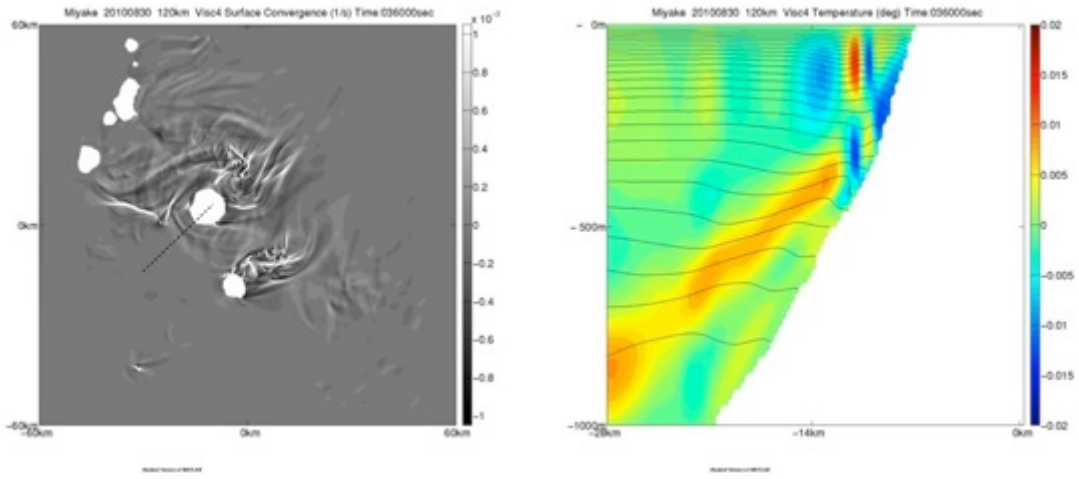

Figure 4.6 Surface convergence field (left) and vertical velocity and temperature distribution on the vertical section parallel to the upstream flow (right) after the 10hours simulation started for the case 30th August 2010.

Compared to the previous studies (Hanazaki,1994 and Vilenski and Johnson 2004) on the upstream propagating atmospheric nonlinear internal wave around a mountain, the internal wave shown in our numerical simulation was stationary. It did not seem to propagate in the upstream direction. The important difference between the previous study and our study was the background flow distribution. Since the topography was set to be finite but small in the previous study, the background velocity was almost constant and well modeled by the KP equation. In contrast, velocity distribution around the island in our configuration was one similar to the flow around the cylinder. If the nonlinear effect modulates the phase speed only slightly, the wave should not propagate upstream. The vertical profiles set to boundary conditions provides nonlinear coefficient μ' of 1.0 if the part of profile below to -500m was used to solve the eigenvalue problem. The modulation effect of phase speed can then be estimated by the Eq. (2.75) and the magnitude is only 0.01m/s if we assume the wave amplitude of 15m. The nonlinear effect for the trapped wave in this simulation is too small to make the wave propagate upstream.

We checked how the background velocity and the propagating speed of the baroclinic modes change with position along the vertical section (Figure 4.7). As the flow approached the Miyake Island, vertical mean speed decreased at first, but then increased as the depth

became shallow. The vertical mean speed and the absolute value of phase speed observed from the background mean current did not overlap, but values were quite close. Since the topography was not uniform, the phase speed was modified by the estimation of the eigenvalue problem, so it can be said that mode-2 internal waves are trapped around the Miyake Island.

In addition to the trapped internal solitary wave around the island, another steady wave was manifested by a bright line shown in the shallow region west of the Onoharajima (the small island located west of the Miyake Island). The vertical section intersecting the bright line from south to north (Figure 4.8) reveals a large amplitude lee wave behind the crest of the sill shaped topography. This suggests that not only tidal flow but also the Kuroshio creates large amplitude nonlinear internal waves in this shallow region. Although the situation was steady because of steady boundary conditions, once the stratified flow decreases velocity the large amplitude wave may propagate freely. This implies that mode-1 nonlinear internal waves can be generated in Izu-Islands region because of the Kuroshio.

The results for 26th/Jul/2006 and 18th/Mar/2008 exhibited trapped internal waves around the islands as shown in Figure 4.9 and Figure 4.10, respectively. Both of the trapped waves appeared roughly 10 hours after the beginning of the numerical simulation.

Even though all three cases of trapped waves were detected by the vertical velocity distribution and temperature distribution in the vertical section, there were significant differences in the horizontal distribution of surface convergence. This implies that mode-2 internal waves are likely to be trapped around the Miyake Island, but the surface manifestation depends on season because of the vertical structure of velocity induced by internal waves depends on the seasonal stratification. The result might be influenced not only by the stratification but also background velocity. However, the parabola pattern around the Miyake Island manifested in the surface convergence field of the case for 26th/Jul/2006 is not as clear as the result of the case for 30th/Aug/2010 even velocity profile with larger vertical mean velocity is applied to boundary and initial conditions.

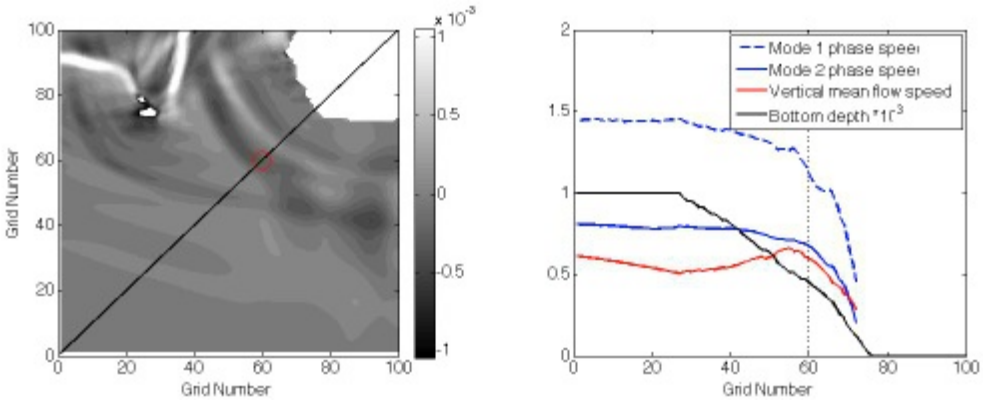

Figure 4.7 Surface convergence field around the Miyake Island with red circle indicating the position of the trapped internal wave along the black line (left). Spatial variation of the phase speeds for each mode, vertical mean flow speed and bottom depth along the black line shown in left panel (right). The black dashed line is located where red circle is put in the left panel.

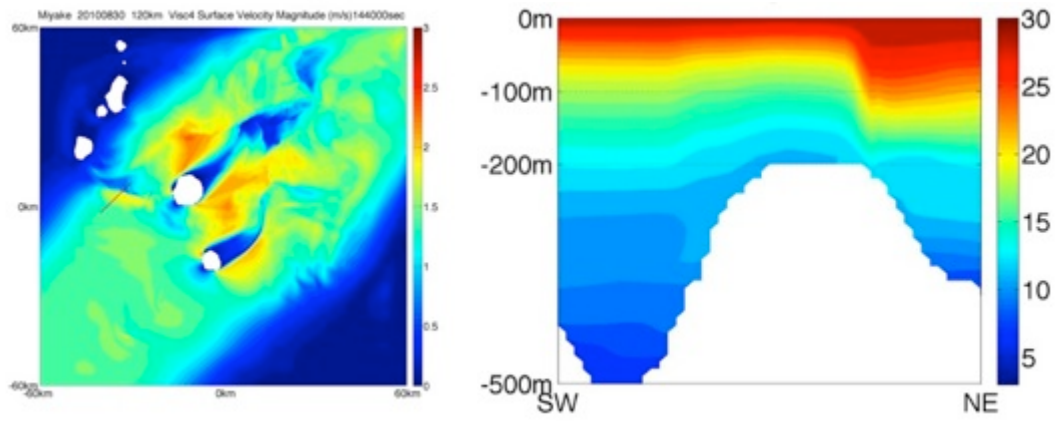

Figure 4.8 Surface velocity field (left) with a red line showing the position vertical section whose temperature distribution is shown in right panel.

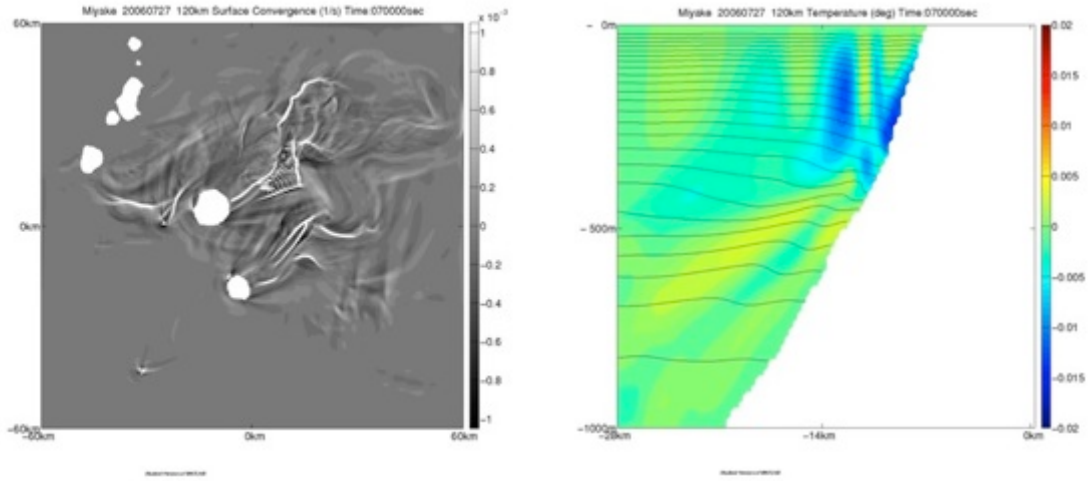

Figure 4.9 Surface convergence field (left) and vertical velocity and temperature distribution on the vertical section parallel to the upstream flow (right) after the 10hours simulation started for the case 26th/Jul/2006.

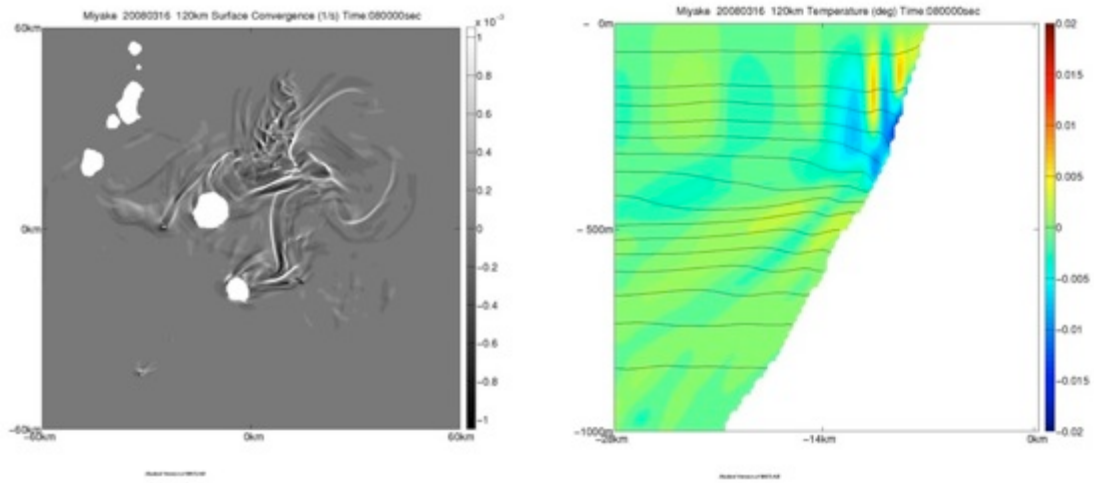

Figure 4.10 Surface convergence field (left) and vertical velocity and temperature distribution on the vertical section parallel to the upstream flow (right) after the 10hours simulation started for the case 18th/Mar/2008

To clarify the relationship between the seasonal density profiles and the parabolic patterns which appeared in SAR images, we also conducted a numerical simulation with monthly averaged density profiles from JCOPE2. This was used for analysis of seasonal variation of the internal wave properties in subsection 3.2.1. We selected monthly averaged profiles of February and August for the comparison. The velocity profiles were modified by multiplying a constant 0.6 m/s vertical mean velocity at the boundary, and the calculated internal wave properties are shown in Table 4.2. The same conclusion as described above came from these new results (Figure 4.11). Mode-2 internal waves are trapped even in February but the induced surface velocity was weaker than that of August. Therefore, the seasonal dependency of the parabolic patterns did not necessarily imply a seasonal dependence on the existence of internal waves.

Table 4.2 Internal wave properties calculated with monthly averaged data of JCOPE2.

	Froude Number		Nonlinearity μ'		$[(c-u_o)\phi(z)]_z$	
Month	mode-1	mode-2	mode-1	mode-2	mode-1	mode-2
February	0.370	0.700	-1.25	-0.40	0.0056	-0.0031
August	0.373	0.662	-2.34	0.738	0.0078	-0.0058

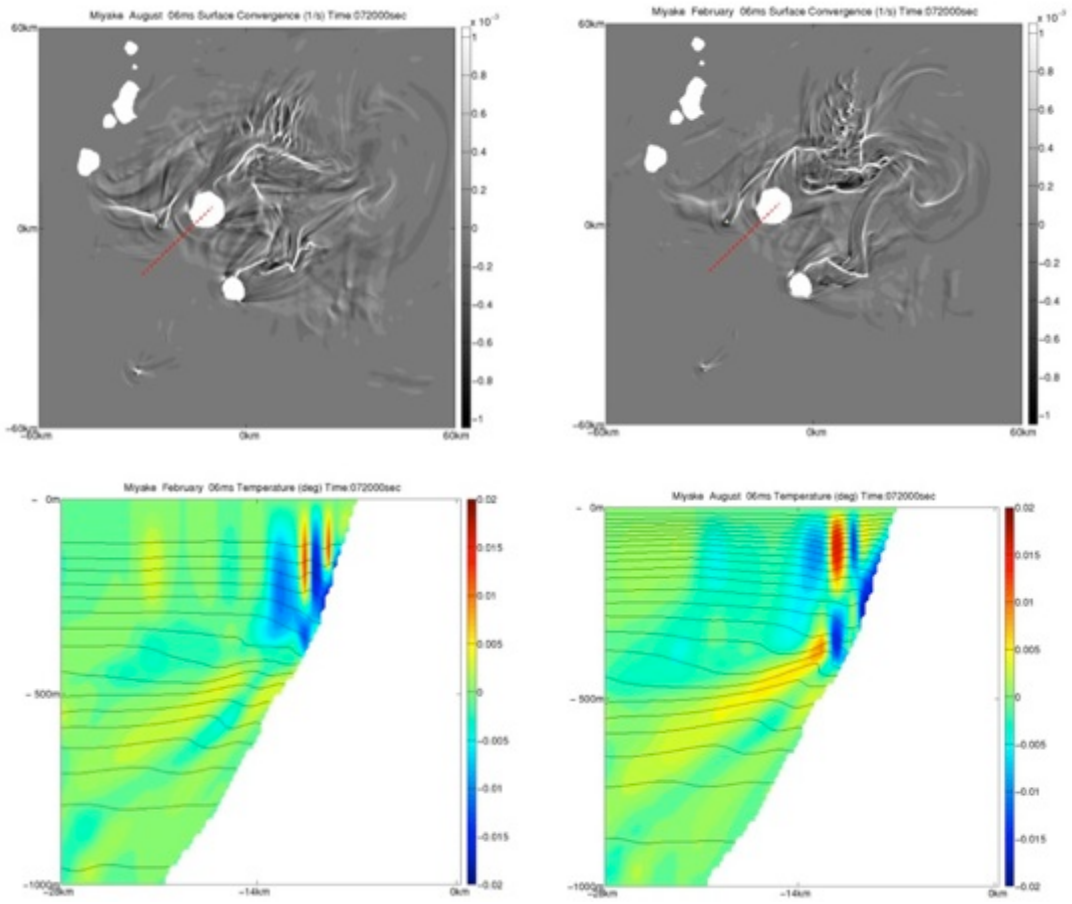

Figure 4.11 Surface convergence field (top) and vertical velocity and temperature distribution (bottom) for the case of February(left) and August(right).

To conduct numerical simulation, we tried different numerical eddy viscosity coefficients. The cases shown above have large surface convergence and divergence area in the lee side of the islands. These were diminished when we applied the larger numerical eddy viscosity. However, they even suppress the evolution of internal waves in front of the islands (Figure 4.12). Since our interest is the internal wave in front of the island, we set the eddy viscosity as small as possible to make the internal wave develop freely.

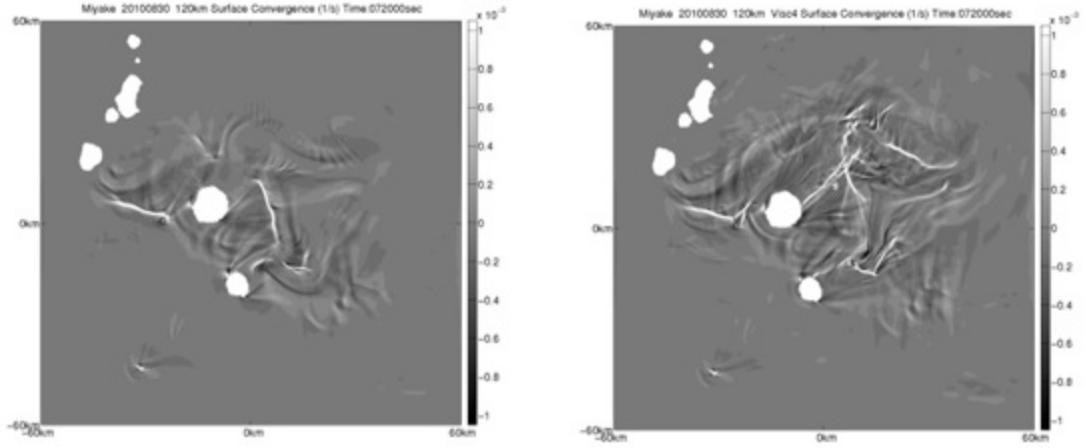

Figure 4.12 Surface convergence field after the 20hours integrated. The numerical vertical eddy viscosity is $A_z = 5\times10^{-2}\mathrm{m}^2\mathrm{s}^{-1}$(left) and $A_z = 5\times10^{-3}\mathrm{m}^2\mathrm{s}^{-1}$ (right).

4.3 Nonlinear Internal Wave Generation around the Izu-Islands

In the previous subsection, vertical profiles at the Kuroshio axis reproduced in JCOPE2 reanalysis data were used as initial and boundary conditions, but the results did not show large amplitude internal waves trapped around the islands. In particular, parabolic patterns did not appear around the Mikura Island in the surface velocity convergence field, while one of the SAR images shows clear parabolic pattern (Figure 1.5).

It should be too early to conclude that parabolic patterns which appeared in SAR images are not manifestations of oceanic nonlinear internal waves, because it is also possible that our boundary conditions did not sufficiently reproduce the real situation. Actually, the JCOPE2 dataset did not include daily variations, such as tidal flow, which may roughly double velocity near the island. It was also possible that the density profile from JCOPE2 did not well reproduce the actual situation. The thermal wind structure of the Kuroshio had a density profile which changed normal to the flow direction. Density profiles are more sharply changed in northern part of the Kuroshio compared to its axis (Figure 4.13). Although the velocity decreased as away from the core, the situation depended not only velocity but also the density profile. Possibly, the numerical diffusion for the vertical density profile might have excluded the thin thermocline that encourages the generation of oceanic nonlinear internal wave as shown in 2.3.4.

We could go further by trying a numerical simulation that applied the vertical profile not exactly at, but near, the Kuroshio axis. It is even possible that the conditions which enable the

appearance of nonlinear internal waves around islands were not included in JCOPE2. The purpose of this study is not only to reproduce the trapped internal waves with ocean reanalysis data, but also to study the conditions responsible for these trapped waves around the islands. Therefore, instead of relying on JCOPE2 reanalysis data, it is better to modify the boundary conditions and investigate the possible nonlinear internal wave generation around islands. We selected a numerical simulation configuration for 30th/Aug/2010, which was studied in the previous section, as referential case, but the density and velocity profiles are modified as described in the next subsection. The periodic forcing of the surface long wave was also included to study the effect of tidal flow around the islands.

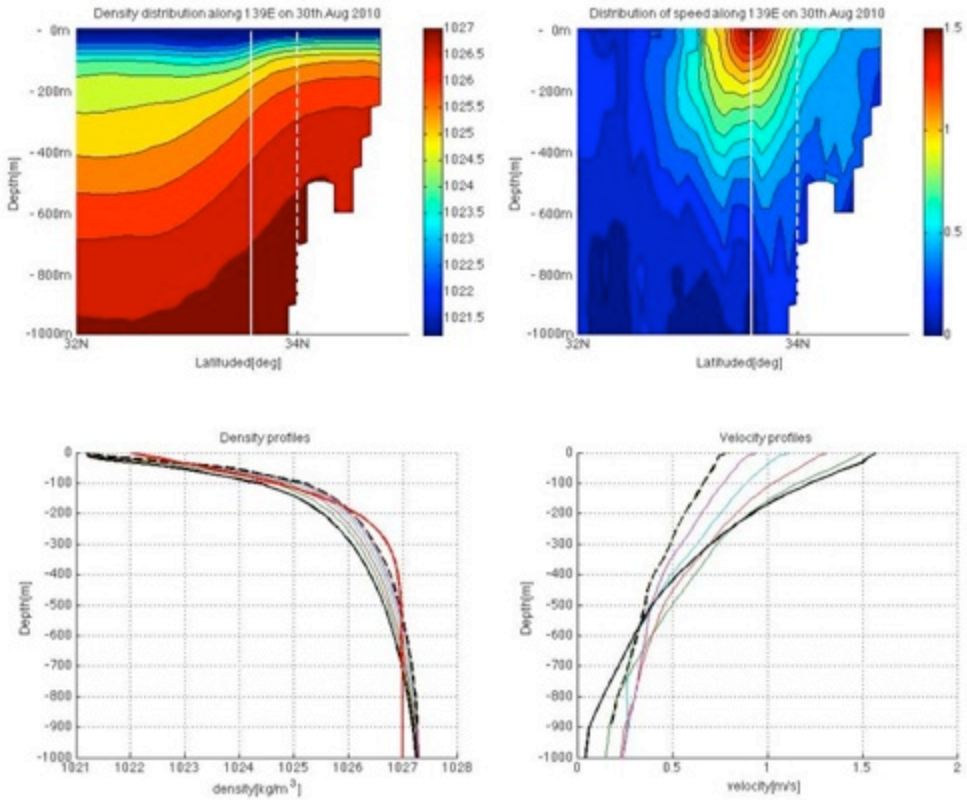

Figure 4.13 Density and velocity structure of Kuroshio core(top panels) and the vertical profiles (bottom panels) from its core (white dashed line in top panels) to the 1/3degree north (white dashed line in top panels) on 30th August 2010 from the JCOPE2 reanalysis data.

4.3.1 Numerical Simulation with Modified Density and Velocity Profile

Following idealized density profile is chosen as the a model of stratification in summer.

$$\rho_{o(z)} = \rho_s - \Delta\rho \tanh(z/1000 * cf) \qquad -1000 < z < 0 \tag{4.10}$$

With a controlling parameter cf, we can systematically control the situation. A larger cf makes the internal wave slower, the nonlinear coefficient larger, and the induced velocity at surface larger as shown in Figure 4.14. This indicates that surface manifestation of internal waves can be strong with increased cf. The density at the surface ρ_s, is not important because the Brunt-Vaisalla frequency was independent of ρ_s.

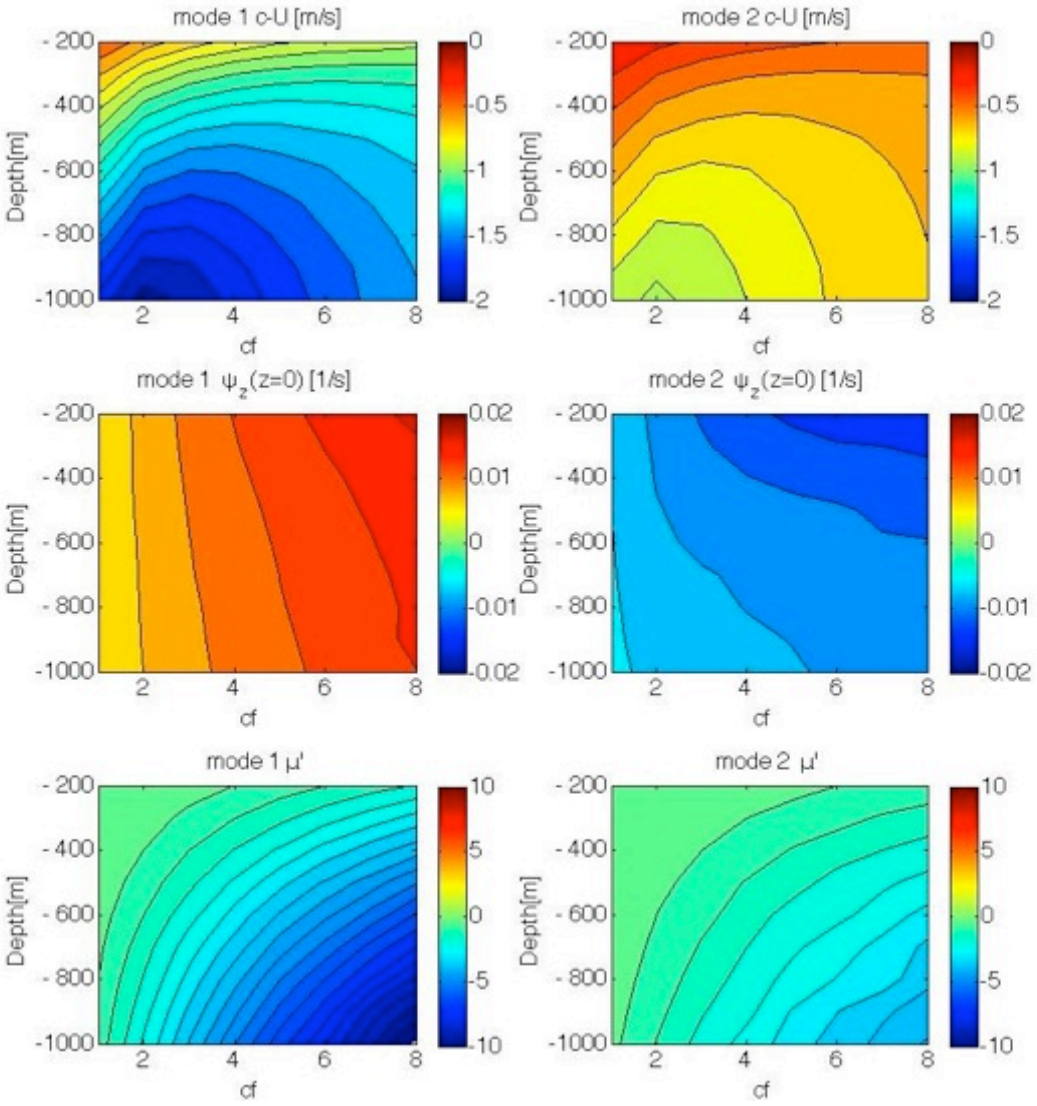

Figure 4.14　Internal wave parameters for density profiles determined by hyperbolic tangent with parameter cf.

To determine the range of cf, we conducted the fitting of density profiles to the function given by (4.10). The ρ_s was directly given as the surface value of data used and the two parameters of $\Delta\rho$ and cf were determined by an iterative least square method. The JCOPE2 reanalysis data and in situ measurement data archived in Japan Oceanographic Data Center (JODC) were used for the fitting process. The in situ temperature and salinity measurement data were acquired from a southwestern area of the Miyake Island over 50 years from 1961 to 2011.The measurement positions of the data we used are shown in Figure 4.15. The data satisfy following conditions: (1) the data had a vertical profile lower than -400 m, and (2) the data was acquired at the position whose sea bottom was deeper than -1000 m. We calculated density profiles from the data but sometimes salinity profiles were not obtained at the same time with temperature. We set salinity profile as constant of 34psu to calculate the density profile by EOS-80.

The results of the fitting were shown in Figure 4.16. Normally, density profiles acquired in the summer season produce larger values of cf and $\Delta\rho$ compared to the winter,

and the results show solutions were on the line with a positive inclination angle. Since the profile given by (4.10) was basically for the summer season, the fitting was not appropriate for the winter season and created another line in the bottom part of the Figure 4.16.

Compared to the JCOPE2 data we used, in situ measurement data was greatly varied. Although in situ measurements data may include the vertical profile far from the Kuroshio axis, the dynamical state for internal waves had a larger variability than the range of vertical profiles from JCOPE2 reanalysis which was considered in the previous section.

We determined the density profile given by (4.10) with $\rho_s = 1022,\ \Delta\rho = 5, \text{and}\ cf = 6$. To construct the density profile in the numerical model, the linear equation of state, set in the MITgcm, was used. The linear equation of state determines density $\rho(\theta, S, z)$ was as follows.

$$\rho(\theta, S, z) = \rho_c(1 + \alpha_t * \theta(z) + \beta_s * S(z)) \tag{4.11}$$

Where $\theta(z)$ and $S(z)$ were temperature and salinity, α_t was thermal expansion coefficient and β_s was haline expansion coefficient. The α_t was set to $2.0\times10^{-4} deg^{-1}$ and β_s was set to $7.4\times10^{-4} psu^{-1}$, and ρ_c was set to $1000 kg/m^3$ in this study and salinity was kept as a constant value of 34 psu over the whole domain.

Internal wave properties were calculated with the density profiles defined by (4.10) with $\rho_s = 1022,\ \Delta\rho = 5, \text{and}\ cf = 6$ and then compared to the original simulation(Figure 4.17). Vertical profiles were used either below to -500 m or -1000 m to evaluate how the properties changed with depth. The solutions obtained without including background flow showed that the idealized density profile had a smaller phase speed, larger magnitude of μ', and comparable value of $[(c - u_o)\phi(z)]_z$[1/s], so nonlinear internal wave generation may have been enhanced. However, once the background shear was included, the difference was not so obvious.

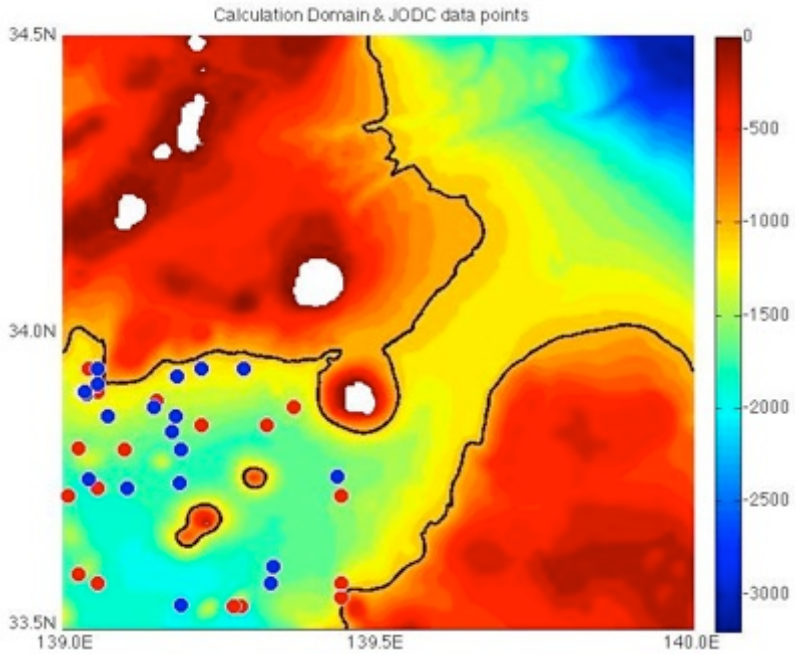

Figure 4.15　Numerical domain for the computation and the measurement points for temperature and salinity data collected in summer season from June to September (red points) and winter season from November to February (blue points) .

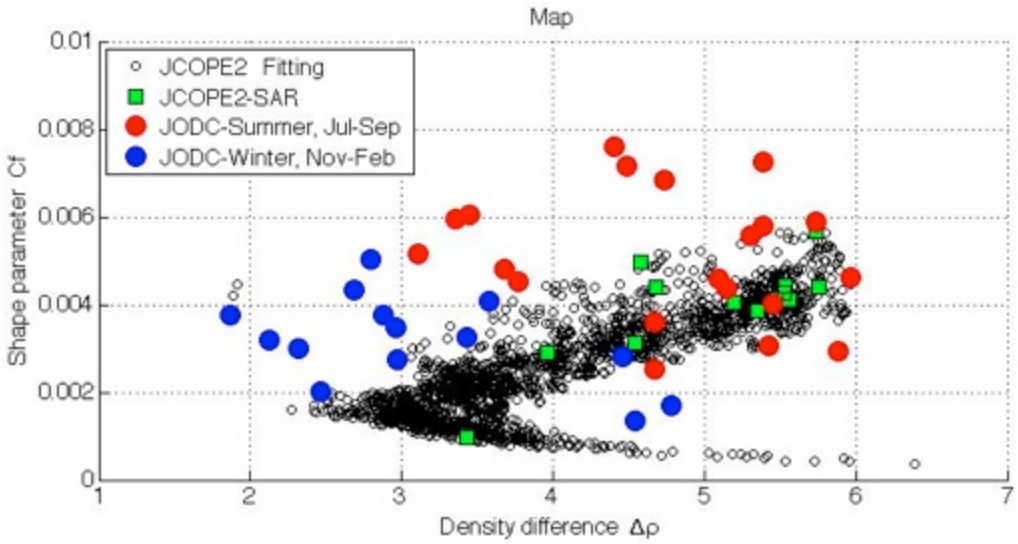

Figure 4.16 Results of the fitting of density profiles to hyperbolic tangent function.

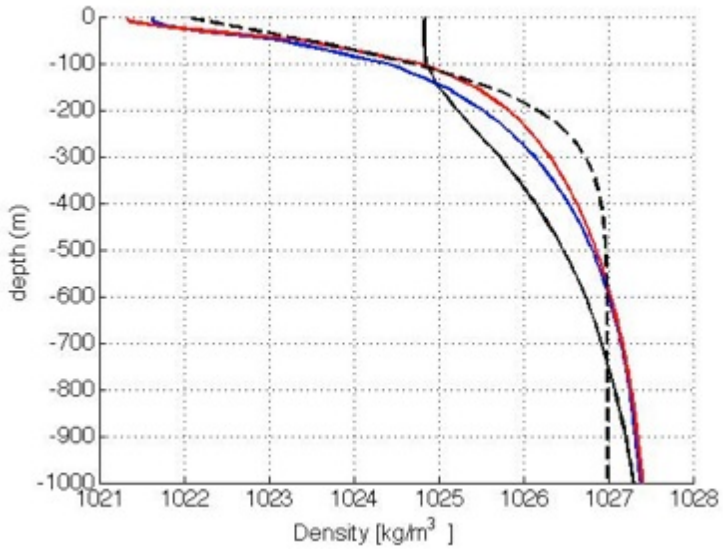

Figure 4.17 Idealized density profile (black, dashed line) and vertical profiles for the numerical simulation for 30th/Aug/2010(red), 27th/Jul/2006/(blue) and 15th/Mar/2008 (black).

Table 4.3 Internal wave properties calculated with density profile of JCOPE2 and with idealized density profile. The background shear is not included to obtain the properties.

	Phase Speed [m/s]		Nonlinearity μ'		$[(c-u_o)\phi(z)]_z$[1/s]	
Case	mode-1	mode-2	mode-1	mode-2	mode-1	mode-2
30th Aug 2010 /1000m	-1.777	-1.01	-5.29	1.71	0.0127	-0.0104
30th Aug 2010 /500m	-1.43	-0.7397	-4.45	0.157	0.0172	-0.0115
tanh / 1000m	-1.74	-0.765	-7.60	-3.29	0.0140	-0.0092
tanh / 500m	-1.48	-0.683	-3.57	-1.59	0.015	-0.0111

Table 4.4 Internal wave properties calculated with density profile of JCOPE2 and with idealized density profile. The background shear is included to obtain the properties.

	Froude Number		Nonlinearity μ'		$[(c-u_o)\phi(z)]_z$[1/s]	
Case	mode-1	mode-2	mode-1	mode-2	mode-1	mode-2
30th Aug 2010 /1000m	0.387	0.700	-2.34	1.00	0.0073	-0.0054
30th Aug 2010 /500m	0.741	1.28	-2.39	1.03	0.0112	-0.0072
tanh / 1000m	0.472	1.37	-8.17	-0.359	0.0098	-0.00023
tanh / 500m	0.698	1.46	-3.00	-1.15	0.0112	-0.0050

Two configurations of the velocity boundary conditions were tested. One configuration was conducted with the original JCOPE2 data, and in the other configuration velocity was magnified by 0.2 m/s at all the depths. The latter case was examined because the vertical mean flow speed of the Kuroshio axis takes nearly 0.8m/s at a maximum (Figure 3.19). The increased velocity was equivalent to making the Froude number 1.34 times larger at the boundary. The Froude Number changes from 0.47 to 0.64 for mode-1 and from 1.37 to 1.84 for mode-2.

As a result of the first case, the surface convergence field showed clear parabolic lines around the both of the Miyake and Mikura Islands (Figure 4.18). Distributions of the vertical velocity and temperature in vertical sections show that the parablic lines are composed by the internal wave. Both of the parabolic lines around Miyake Island and Mikura Islands consisted of mode-2 internal waves, but the one adjacent Mikura Islands propagated upstream. After 20 hours of simulation, mode-2 internal waves remained around Miyake Island but not Mikura Island. Instead, mode-3 appeares around the Mikura Island. This implied that multi modes may be trapped around the islands.

When the velocity was magnified, the generated internal waves were intensified. After the 10 hours of simulation, an initial shock consisting of a mode-1 internal wave propagated away from the islands. They showed a nonlinear internal wave train near Mikura Island. The wavy pattern shown in the surface velocity convergence field cannot be reproduced with the hydrostatic approximation. However, the mode-1 waves were likely to propagate away as time moved forward. The one from Miyake Island remained longer compared to the one from the Mikura Island because of the shallow topography.

On the other hand, a clear parabolic pattern appeared around Mikura Island. This was composed by a mode-2 internal wave as shown in Figure 4.19 (bottom). The parabolic patterns shown in the surface convergence field were quite similar to the SAR images. Both showed a clear parabolic pattern around the Mikura Island (Figure 1.5) though the color was opposite. This result indicates that oceanic nonlinear internal waves were possibly generated around the islands when the Kuroshio approached.

Not only the parabolic lines but also straight line similar to Kelvin ship wave appeared around small Inanba Island located southern-western part of the numerical domain. There is one more similar pattern in the lee side of Inanba Island and this is due to the seamount. Although the two V-shaped patterns are similar to Kelvin ship wave, these are composed by

weakly dispersive internal long waves, so they are dynamically similar to shock wave. The angle θ_{Mach} is callled Mach angle and it can be estimated by the following simple formula even the formula is only valid for the point source.

$$sin(\theta_{Mach}) = c/U \tag{4.12}$$

In the numerical simulation, the propagation speed of the wave was calculated to be 0.423 m/s and the vertically averaged background flow speed was 0.786 m/s, so the Mach angle, , was 32.56 degrees. The estimated 32.56 degree Mach angle was qualitatively consistent with the angle shown in surface convergence field, but more accurate estimation of the Mach angle or three-dimensional internal wave distribution requires the method of characteristics (Johnson and Vilenski 2004).

When compared to the simulations in which the initial and boundary conditions were set with vertical profiles of the Kuroshio axis reproduced in JCOPE2, internal wave generation and the surface manifestation was enhanced. The trapping only appears nearby islands where the background flow speed had decreased. This may indicate that the density profile basically determines the character of the trapped internal wave around the islands.

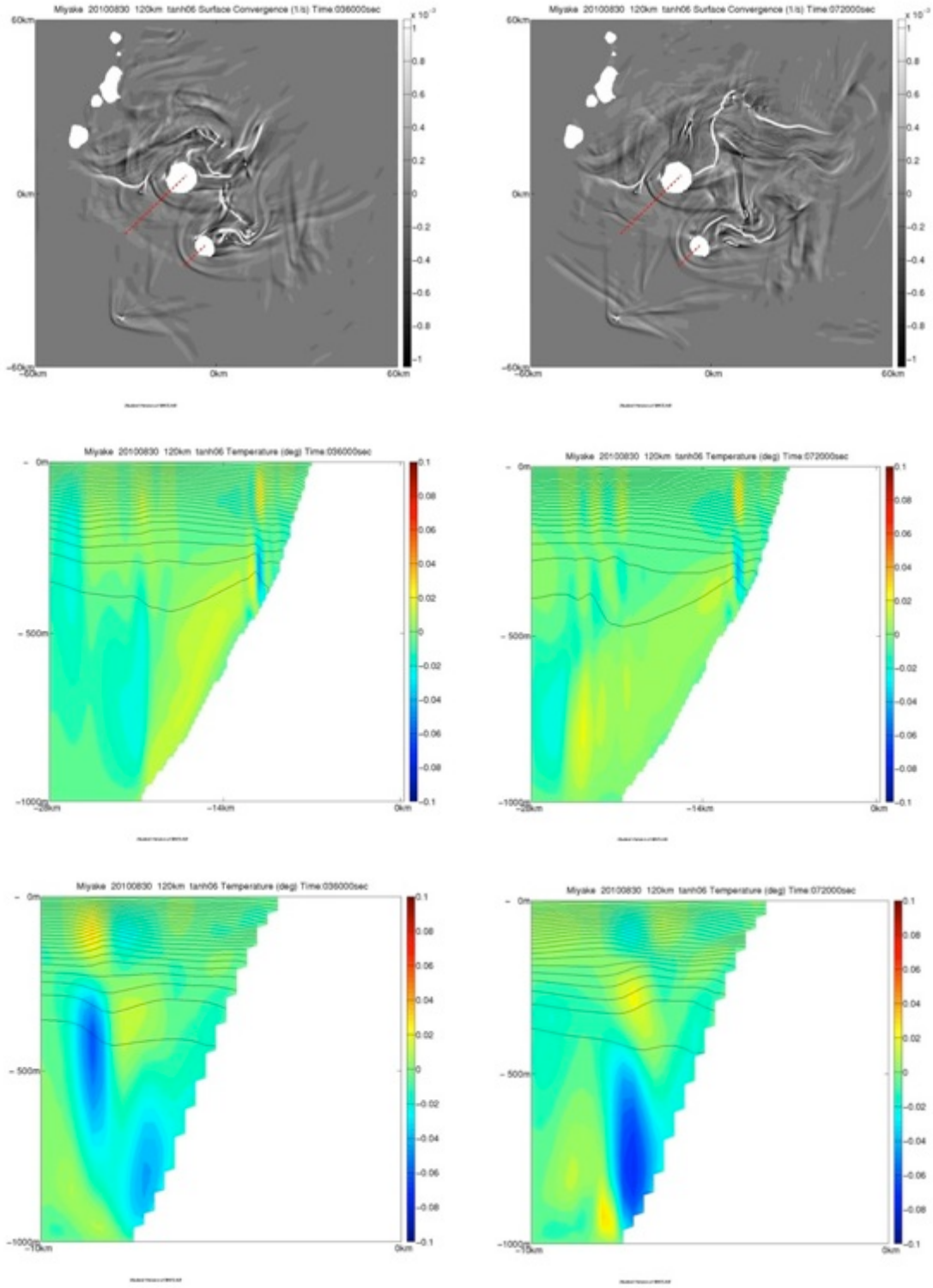

Figure 4.18　Numerically simulated surface convergence field (top), temperature (contour) and vertical velocity (color) distribution along the line intersecting the Miyake Island (middle) and Mikura Island (bottom). Left and right column shows the results after 10hours and 20hours respectively.

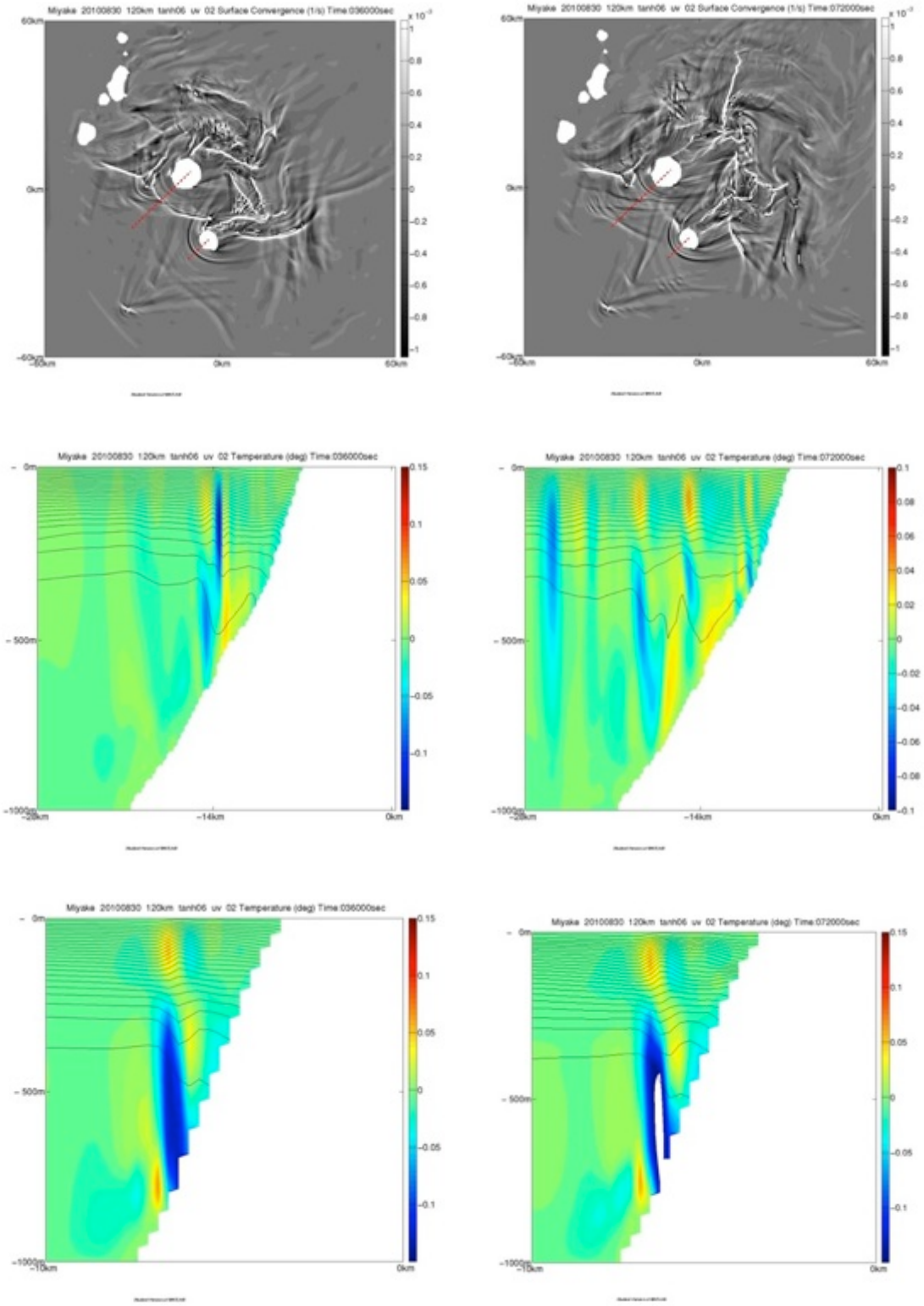

Figure 4.19　Same as the Figure 4.18 but the velocity profile for initial and boundary conditions are magnified with 0.2m/s constantly for whole domain.

4.3.2 Nonlinear Internal Wave and Periodic Forcing

The results of previous numerical simulation clarified that internal waves are trapped around the islands and induce surface velocity convergence field of parabola lines. The intensity of the convergence or divergence is in the range that modifies the wind wave field (Alpers, 1978). Another important factor influencing the phenomena in the ocean is tidal flow. Tidal flow changes semidiurnal period around the Izu islands and it should be studied whether the period is enough long to induce nonlinear internal wave by making transition between subcritical and supercritical state. It must be possible that SAR detects the parabola pattern when the tidal flow assists the Kuroshio to create critical situation.

We examine the effect of tidal flow by adding the periodic forcing to the horizontal boundary conditions. A periodic velocity is given

$$\frac{u_{tide}}{\sqrt{2}} * sin\left(\frac{2\pi t}{T_{tide}} + \alpha * \left(\frac{x+y}{\sqrt{2}}\right)\right) \tag{4.13}$$

and is added to $u_{o(z)}$ that is applied to boundary conditions. The constants T_{tide} is set to 24hours and u_{tide} is set to 0.1m/s. From the linear theory, the former and the latter case induce the surface elevation displacement of 1m with the water depth of 1000m. The α is the phase difference between southwestern corner and northeastern corner of the numerical domain. Here, the component of the wave propagates to exactly southwestward is considered. Since the surface long wave propagates with speed $\sqrt{gh}$ where g is gravitational constant and h is water depth and the value is typically 1000m in our numerical domain, so the phase speed is nearly 100m/s. The phase difference can be calculated with $\alpha = 2\pi/(T_{tide} * 100)$ with assumption that phase linearly changes in space. With this configuration, velocity at the boundary take its maximum value, $u_{o(z)} + u_{tide}$, at the time $T_{tide}/4$ after the simulation started. Again, two configurations of the velocity boundary conditions were tested. One configuration was conducted with the original JCOPE2 data, and in the other configuration velocity was magnified by 0.2 m/s at all the depths.

Numerical domain is also modified to simulate the surface long wave propagating parallel to background stratified shear flow. The modification is conducted by following equation that change the depth gradually approaching the value of -1000m at the boundary.

$$d_{mod}(boundary, r) = d(boundary, r) * a + (-1000) * (1 - a), \qquad a = (r/w)^2 \tag{4.14}$$

The variable $boundary$ is selected from north, east, south or west, the r is distance from the boundary and the w is the width of area where the modification is implemented. The w is set to be 16km and the modified topography is shown in Figure 4.20. Time integration is conducted for 3days.

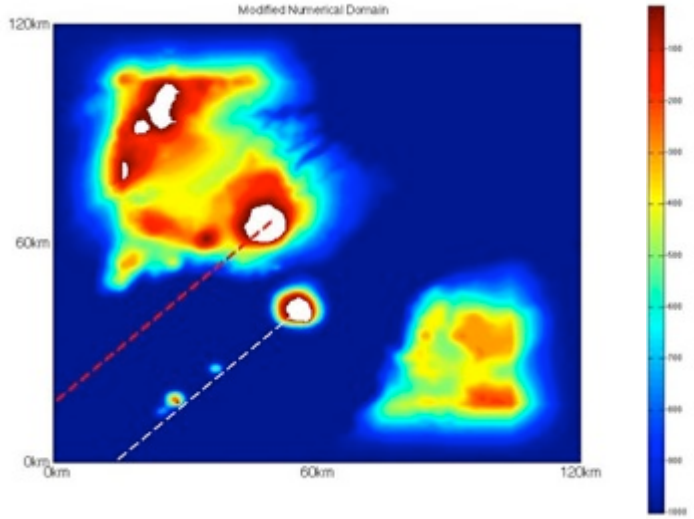

Figure 4.20　Modified numerical domain. Dashed lines shows the location of the vertical sections used in the analysis.

We first describe the extreme case since the situation is more prominent. The velocity profile for the 30th August 2010 reproduced in JCOPE2 data was magnified by 0.2 m/s at all the depths. As the simulation begun, an initial disturbance around the island developed and tried to propagate upstream. However, as the time approaches to $1/4T_{tide}$, flow around the island intensified and prevented the excited waves from propagating away. The surface velocity decreased around the Miyake Island because of the velocity induced by trapped internal wave of mode-1 (Figure 4.21, top). As the velocity induced by the surface long wave decreased and changed its direction, mode-1 internal waves began to propagate (Figure 4.21, middle and bottom) like as the lee wave generation mechanism (Maxworthy, 1979). As the mode-1 internal waves continued propagating southwestward, surface convergence was intensified. The evolution of the mode-1 internal wave along the red dashed line is shown in Figure 4.20. Along this line, internal solitary wave trains were evident (Figure 4.24). The wave height was roughly 50m and this was also examined from the temperature distribution on the vertical section. The solitary wave train exhibits the larger nonlinearity of mode-1 wave than mode-2 as shown in the values of μ' (Table 4.4). As the wave approached to the western and southern boundaries of numerical domain, the amplitude decreased. The reason for the decrease is not clear. This may be due to flow relaxation scheme at the boundary which starts to absorb the wave or the evolution of the nonlinear internal wave itself.　After one period of the forcing ended, the flow field around the island was, again, magnified by the surface long wave and the mode-1 internal wave appeared as shown in the surface convergence field around the Miyake Island (Figure 4.22, middle and bottom). The mode-1 internal wave propagated as it did during first period, but the amplitude was slightly smaller. This result indicates that nonlinear internal waves could be periodically evolved during the period when surface long wave accelerates the flow past the islands. On the other hand, mode-2 internal waves, shown as black parabolic lines around the both of the Miyake and Mikura Islands, did not propagate away. The wave profile, estimated by the orthogonal

relation, was contaminated by mode-1 waves only. This was because the background shear flow modified the vertical mode of the internal waves, and the propagation of the mode-2 internal waves was hardly evident. The temporal evolution of the temperature distribution (not shown) only showed the contraction and expansion of the width of the mode-2 internal waves and did not show its release

Although the mode-2 internal waves could not freely propagate away and were trapped around the islands, the magnitude of the surface convergence and the shape of parabola changed periodically. The convex shaped mode-2 nonlinear internal wave was shown in the temperature distribution on the vertical section along the red dashed line shown in Figure 4.20. As the surface long wave accelerated the flow past the islands, curvature of the parabola and the intensity of the surface divergence increased. The decrease of the curvature also appeared in the numerical simulation with steady boundary conditions (studied in the previous subsection), so the temporal change of the velocity induced by surface long wave may be considered as long as the wave is trapped over the whole period. The results showed mode-1 nonlinear internal wave can be also generated and released if the flow field changes with a time scale of 24hours. The important result from these numerical simulations was that tidal flow has long enough time scale to changes the flow field between subcritical and supercritical. This indicates that the detection of the oceanic nonlinear internal waves by SAR and the shape of parabola pattern are also influenced by tidal flow.

The other case without the additional uniform flow also produced periodic generation and the propagation of mode-1 internal wave, but the amplitude is smaller. It was not clearly seen in the surface convergence field (Figure 4.25 and Figure 4.26), but the component was propagating as the Figure 4.27 shows. The trapped modes were same as the steady case examined in the previous subsection. Mode-2 wave is trapped around the Miyake Island and the mode-3 wave is observed around the Mikura Island. Around the Mikura Island, an advection of the mode-2 internal wave is exhibited in Figure 4.27. Compared to the previous case with additional vertical uniform flow, the periodic change of the surface convergence field is more apparent because of the relative importance of the periodic forcing is larger in this case.

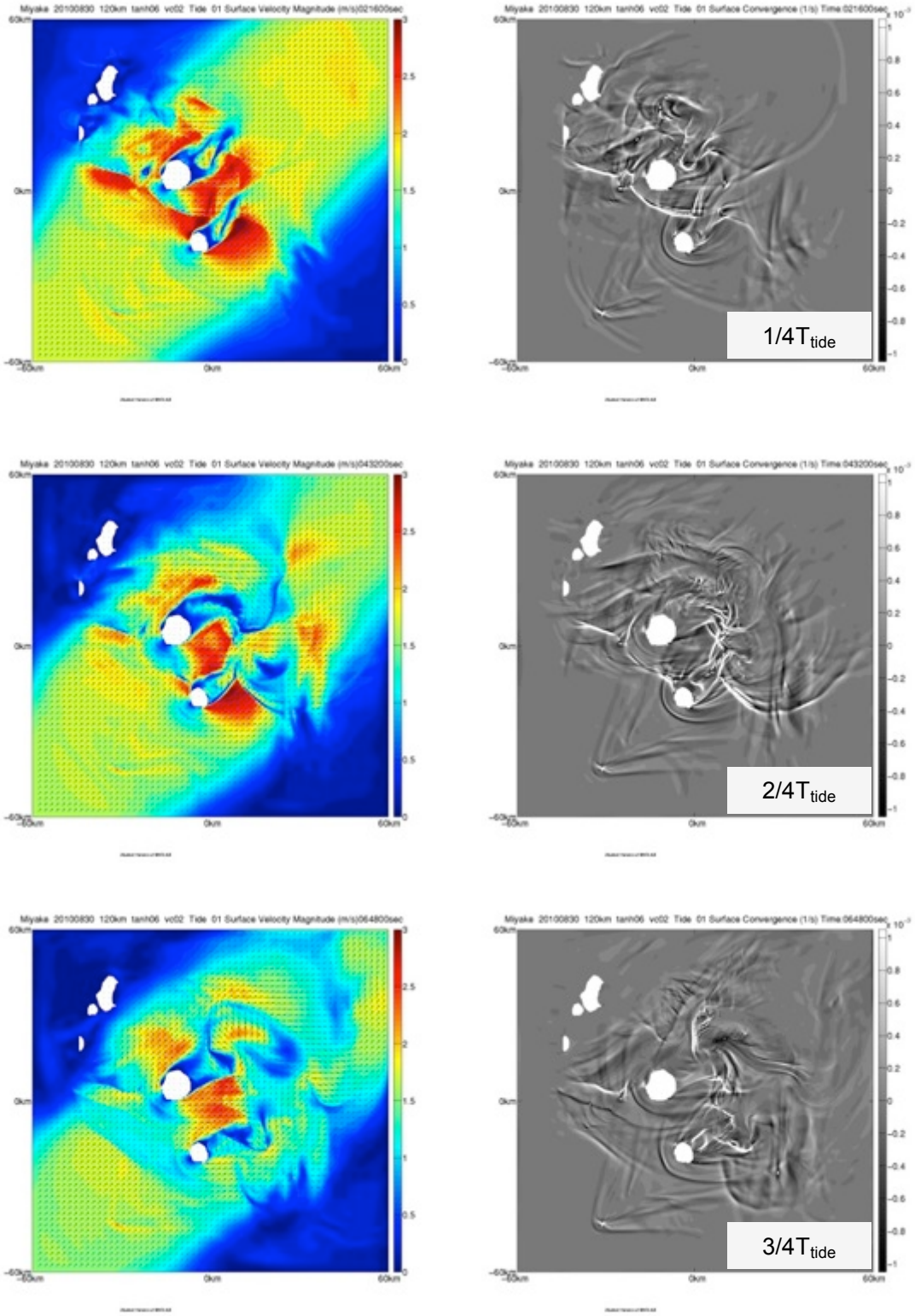

Figure 4.21 Surface distribution of velocity magnitude (left) and convergence (right) at $1/4T_{tide}$, $2/4T_{tide}$ and $3/4T_{tide}$ for the case that the velocity profile is uniformly magnified with 0.2m/s.

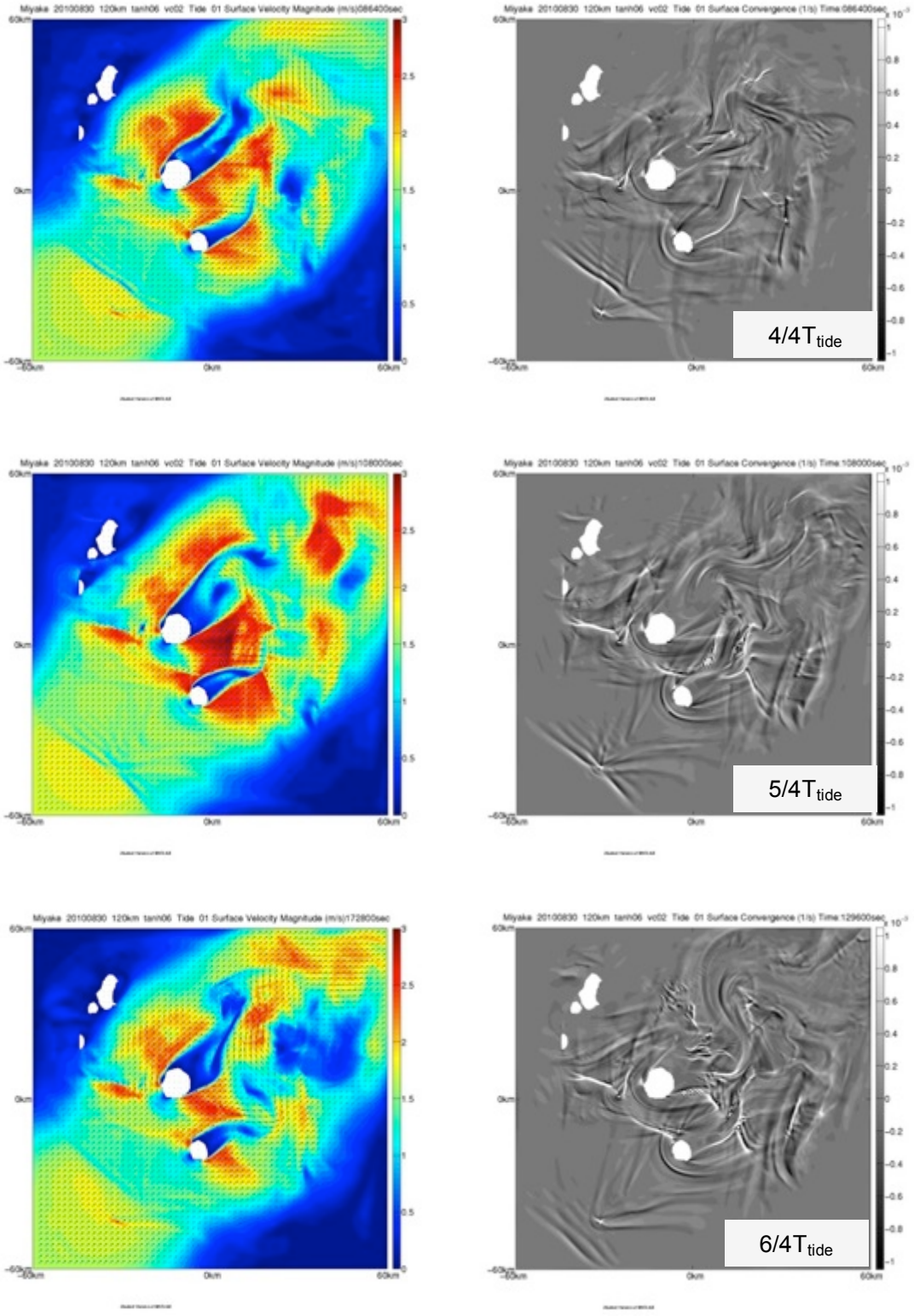

Figure 4.22 Same as Figure 4.21 but the time for $4/4T_{tide}$, $5/4T_{tide}$ and $6/4T_{tide}$.

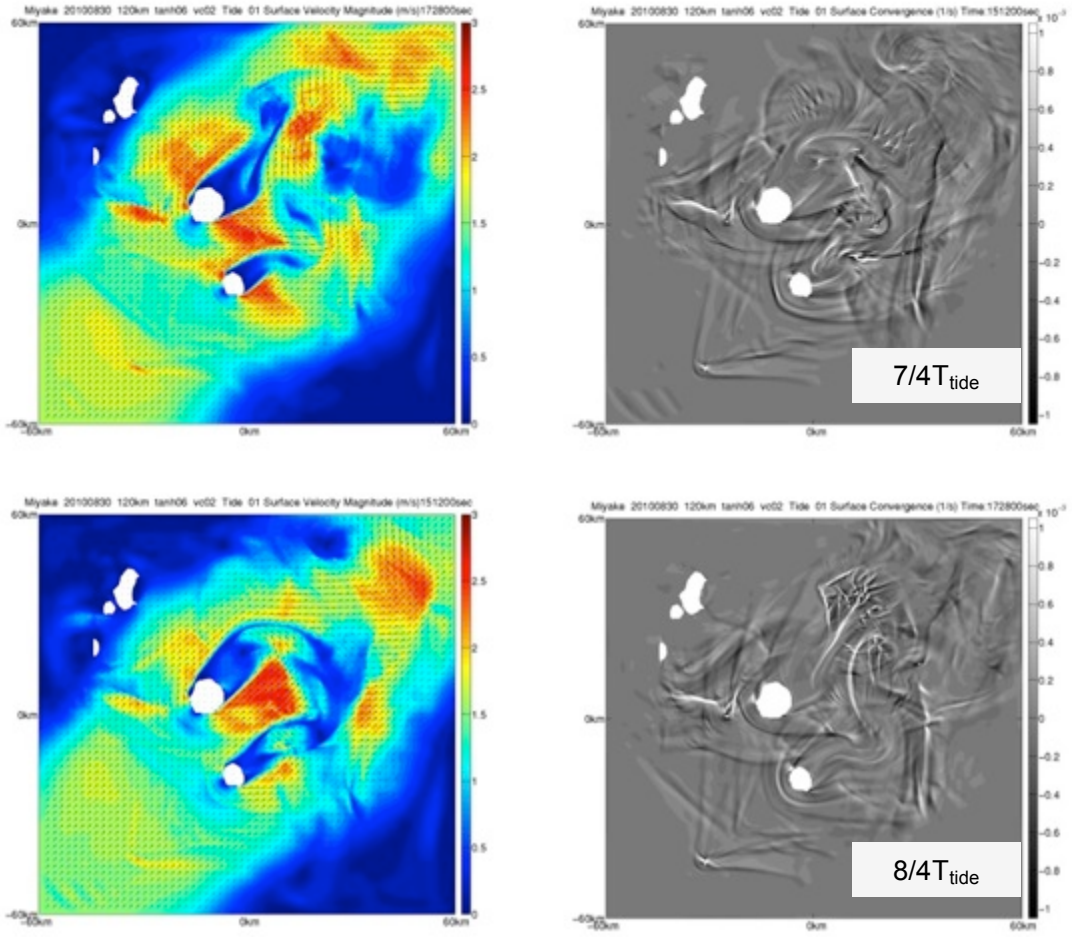

Figure 4.23　Same as Figure 4.21 but the time for $7/4T_{tide}$ and $8/4T_{tide}$.

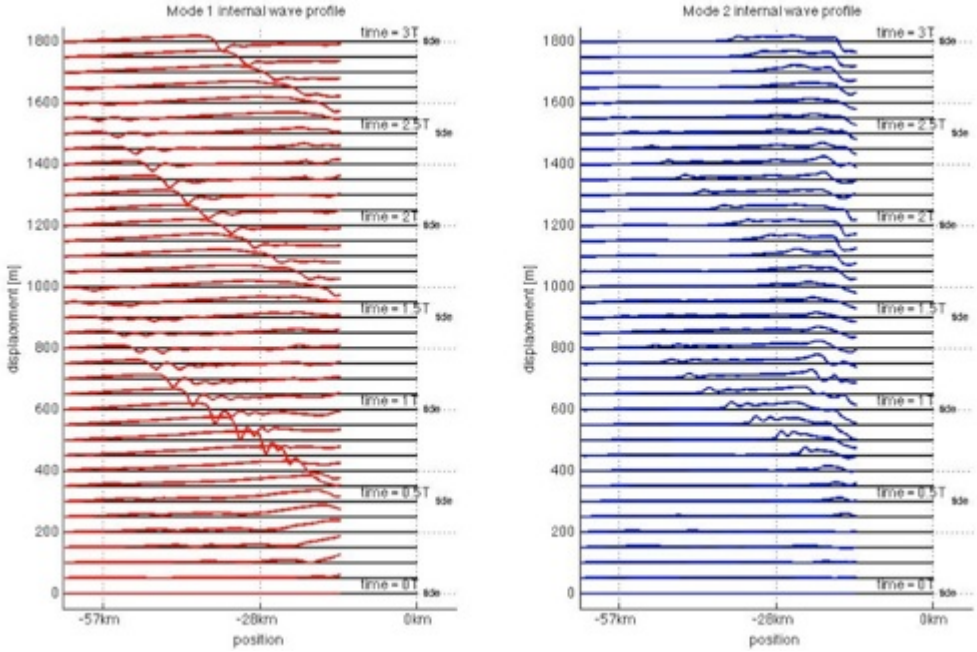

Figure 4.24　Wave profiles of mode 1 (left) and mode 2(right) internal waves along the red dashed line shown in Figure 4.20. The wave profiles are estimated by orthogonal relation for the modal function of velocity.

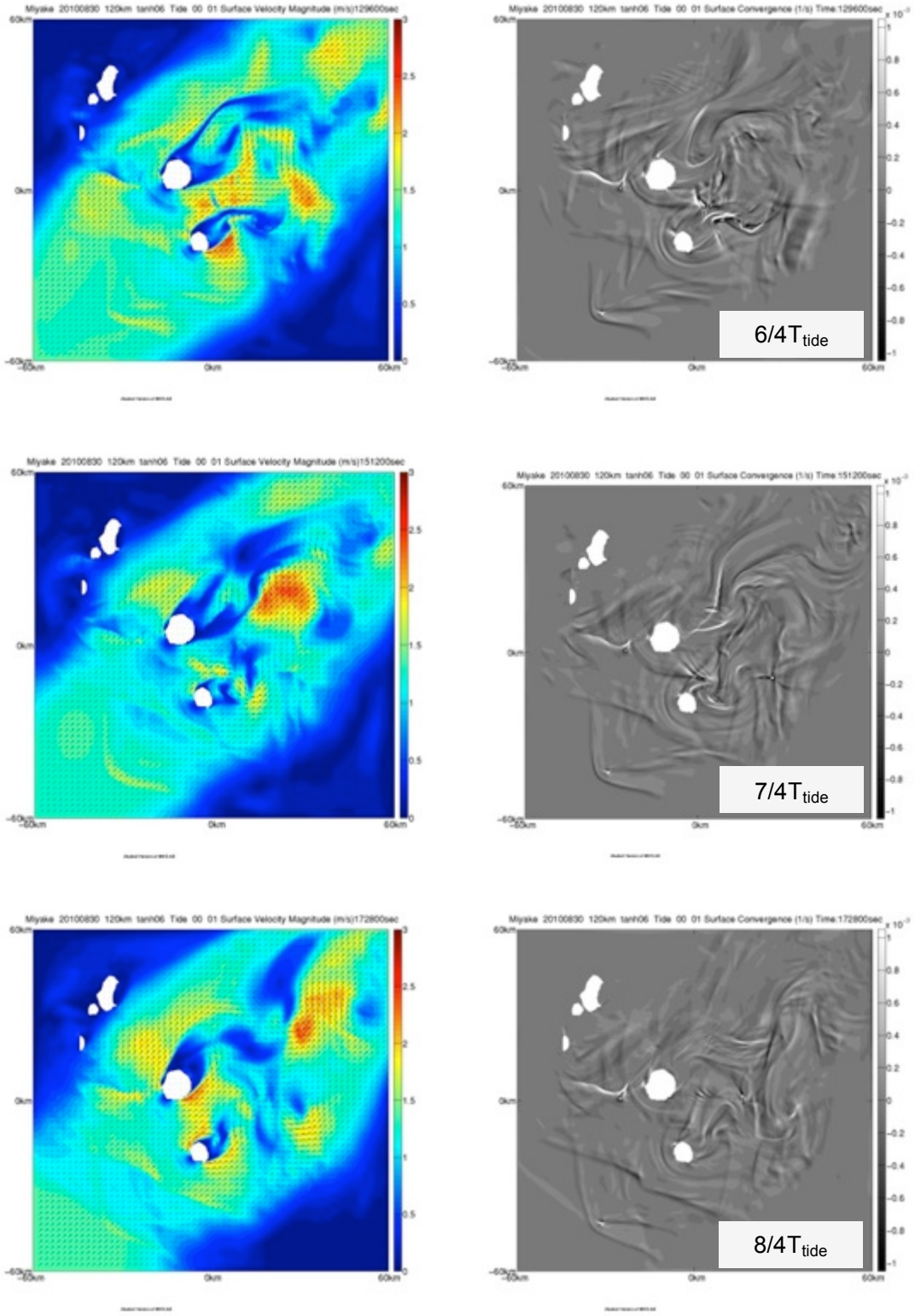

Figure 4.25　Surface distribution of velocity magnitude and convergence at $2/4T_{tide}$, $4/4T_{tide}$ and $6/4T_{tide}$ after the simulation started. The case does not have additional uniform flow of 0.2m/s.

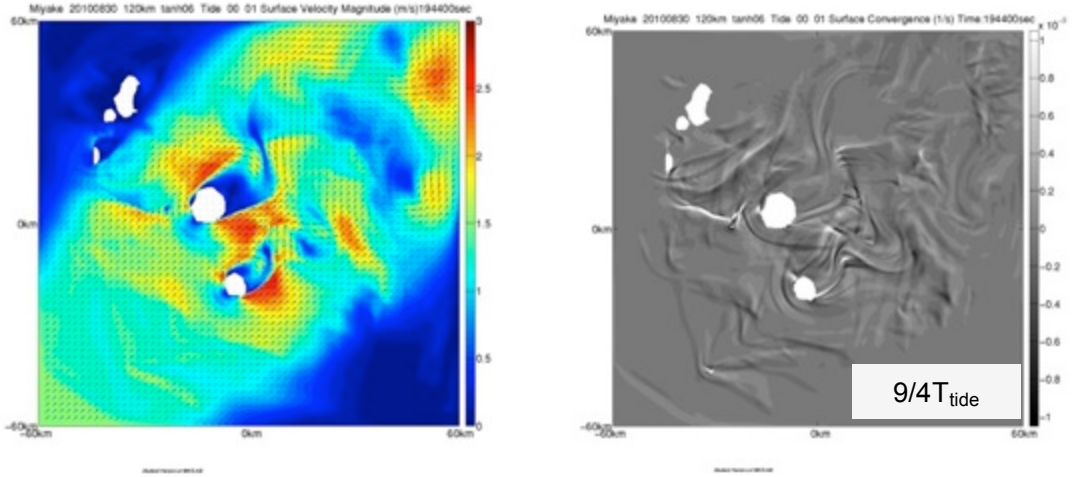

Figure 4.26　Surface distribution of velocity magnitude and convergence at $8/4T_{tide}$, after the simulation started. The case does not have additional uniform flow of 0.2m/s.

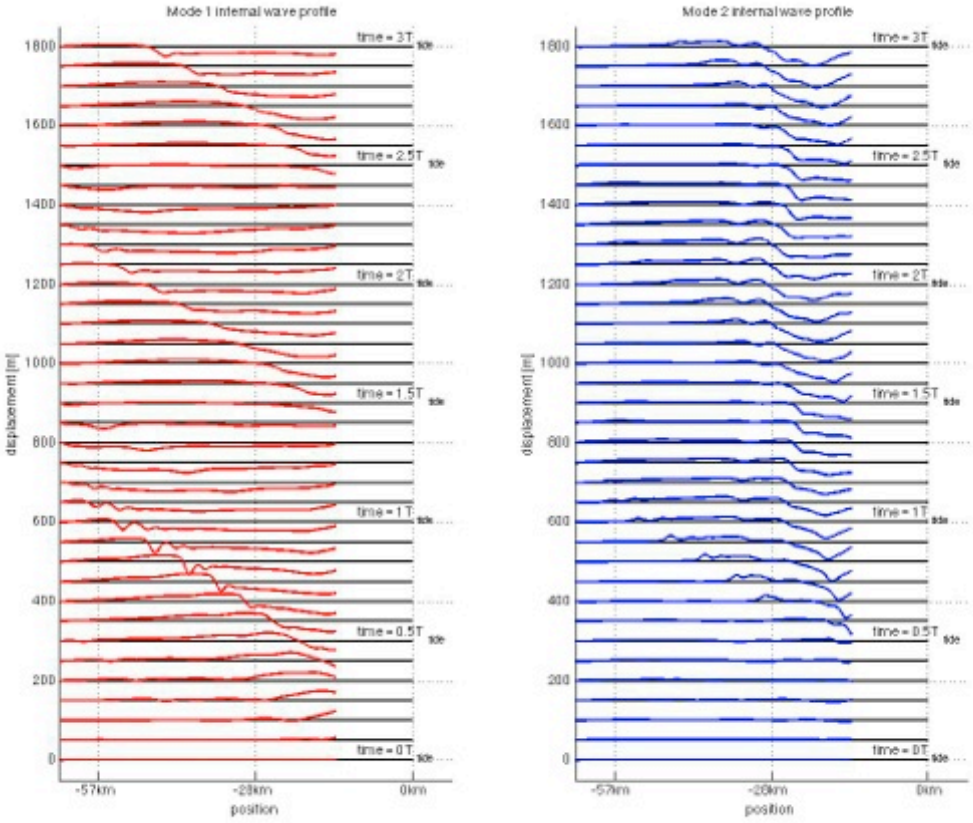

Figure 4.27　Wave profiles of mode-1 (left) and mode-2(right) internal waves along the red dashed line shown in Figure 4.20. The wave profiles are estimated by orthogonal relation for the modal function of velocity. The case does not have additional uniform flow of 0.2m/s.

4.4 Discussion and Summary

In this section, we conducted series of numerical simulation with boundary conditions applied from JCOPE2 data and idealized density profiles.

Results of the simulation with vertical profile of Kuroshio axis from JCOPE2 data revealed that mode-2 internal waves are trapped around the Miyake Island and one of the cases for 30th August 2010 has parabola line in surface convergence field that can be detected by SAR. However, the wave amplitude is at most 20m, so it is hard to call nonlinear. In addition, any of the cases did not reproduce the trapped internal wave signature in surface convergence field around the Mikura Island. This might imply that actual environmental conditions around the Izu-islands are not fully included in the JCOPE2 reanalysis data. Instead of trying the numerous cases with JCOPE2 data, idealized density profiles were used to study possible nonlinear internal wave generation around the Izu-islands. The result produced parabola patterns in surface convergence field around the both of the Miyake and Mikura Island. When the background velocity is magnified with, internal wave generation was enhanced. The series of numerical studies suggests that nonlinear internal wave generation around the island is possible since the modification of the density profile changed the numerical results significantly.

The effect of periodic forcing on the nonlinear internal wave around the island is further studied. The case with additional uniform flow $0.2m/s$ showed mode-1 internal solitary wave trains generated during the accelerated period and freely propagate after the velocity induced by surface long wave decreases and changes its flow direction. The generation was periodic with same frequency of the boundary forcing. On the other hand, mode-2 nonlinear internal waves are trapped during the whole period. However, mode-2 internal waves also can propagate freely because the trapping depends on the propagation speed and the background flow velocity. Our results of numerical simulation with periodic forcing suggests that tidal flow helps the generation of the nonlinear internal wave around the island and the tidal period is enough long for the internal waves to accumulate the energy to become finite amplitude internal waves.

Chapter 5 Three-dimensional Nonlinear Internal Wave Generation around Island Topography in Continuously Stratified Flow.

The resonant generation of the atmospheric three dimensional nonlinear internal wave around mountain topography was studied previously (Hanazaki, 1994 and Johnson and Vilenski, 2004). However, the oceanic analog around island topography has not yet been studied. To obtain a better understanding of nonlinear internal wave generation around the islands studied in the previous sections, we investigated the dynamics by focusing attention on background shear flow and the topography as a source of nonlinear internal waves. In this section we assess the effect of each by studying the following three situations: (1) linearly sheared flow past the circular cylinder, (2) vertically uniform flow over Gaussian bell topography, and (3) linearly sheared flow over the Gaussian bell topography.

5.1 Linearly Sheared Flow past the Circular Cylinder

5.1.1 Numerical Model Settings

A box domain of 40 km by 40 km in the horizontal and 500 m in the vertical was set, and a vertical circular cylinder of 3 km radius was located in the domain as shown in Figure 5.1. The cylinder was not a perfectly circular cylinder because the Cartesian grid was used. The grid spacing was 100 m in the horizontal and 10 m in the vertical. The aspect ratio of the depth and diameter of the cylinder is 1/12 to efficiently produce long waves around the cylinder.

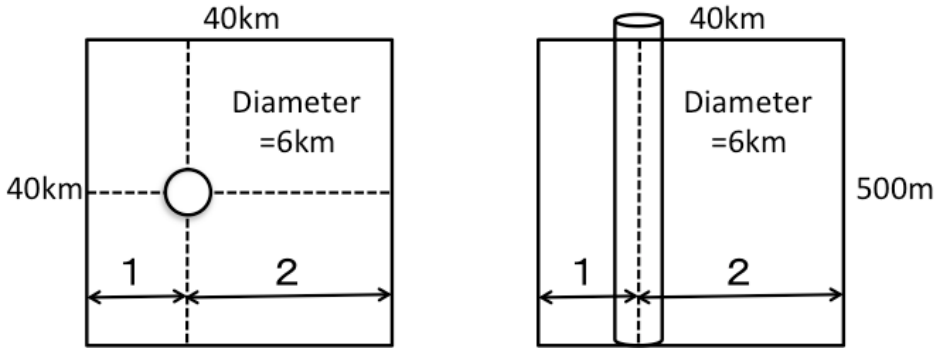

Figure 5.1 Numerical Domain, top view (left) and side view (right).

For initial conditions, a horizontally uniform stratification was set. The density profile only depended on the temperature, and the salinity was a constant of 34 psu, for simplicity. The following temperature profile was set.

$$\theta_{o(z)} = \theta_s + \frac{\Delta\rho}{\rho_c \alpha_t} \tanh\left(z/D * cf\right) \qquad -D < z < 0 \tag{5.1}$$

which determined the density profile by the linear equation of state as follows

$$\rho_{o(z)} = \rho_s - \Delta\rho \tanh(z/1000 * cf) \qquad -1000 < z < 0 \tag{5.2}$$

We set the upstream linearly sheared flow as follows.

$$u_{o(z)} = c_1 (1 + Sc + 2Sc * z/D) \qquad -D < z < 0 \tag{5.3}$$

Although the vertical shear flow changed the phase speed of the internal wave, the vertical mean of $u_{o(z)}$ was c_1, so the situation was near critical. The initial velocity field was set as irrotational flow around the cylinder at each depth given by

$$u_{r(r,\theta_{ang},z)} = u_{o(z)}\left(1 - \frac{a^2}{r^2}\right)cos\theta_{ang} \qquad -D < z < 0 \tag{5.4}$$

$$u_{\theta_{ang}(r,\theta_{ang},z)} = -u_{o(z)}\left(1 + \frac{a^2}{r^2}\right)sin\theta_{ang} \qquad -D < z < 0 \tag{5.5}$$

where u_r and $u_{\theta_{ang}}$ are velocity components in polar coordinate defined by distance r and angle θ.

Boundary conditions were steady for $u_{o(z)}$ and $\theta_{o(z)}$ but other variables were fixed at constant values: $v_{o(z)}$, $w_{o(z)} = 0$ and $S_{o(z)} = 34$. Sponge layers of 2 km were added to all horizontal boundaries and we set relaxation times of $\tau_i = 2 * 10^3$ s and $\tau_b = 2 * 10^2$ s. Constant viscosity coefficient of A_h and A_z were set to 1 m^2/s and 10^{-1} m^2/s, respectively, and diffusivity coefficients of K_h and K_z were set to 1×10^{-2} m^2/s and 1×10^{-4} m^2/s, respectively.

5.1.2 Referential Case

We first investigated an effect of background linearly sheared flow on nonlinear internal wave generation. We selected the Sc in (5.3) as the controlling parameter and set $cf = 3$ in (5.2) as the referential case. The phase speed and the nonlinear coefficient, μ', were calculated by solving the eigen value problem (Table 5.1).

Table 5.1 Phase speeds of internal wave and nonlinear coefficient μ' for each case.

Sc	0.0	0.5
$c_1^- - U$	-1.480	-1.250
μ'^-_1	-3.529	-2.779

The shape of internal wave was determined through following two methods. The first method made use of the orthogonal relation and linear theory as described in sub-subsection 2.3.1. The amplitude for each mode, $A_m(x - ct)$, was determined by the following formula:

$$A_m(x - ct) = \int_{-h}^{0} (u - u_o)\phi_{mz}dz \Big/ \int_{-h}^{0} c_m\phi_{mz}\phi_{mz}dz \tag{5.6}$$

The second method measured the displacement of the water at $z = z_m$, where z_m was the position where $\phi^{\pm}_{m(z)}$ took its maximum value. If several modes were not overlapped, both of the methods agree within an error of $O(\alpha A_m(x - ct))$. The orthogonal relation is not formally valid if there is a background shear flow, but we used the relation anyways because background flow was not uniform. The evolution of surface velocity field and temperature distribution for the case with Sc= 0.5 are shown in Figure 5.2 and Figure 5.3 In front of the cylinder, successive formation of the internal wave was apparent. The wave propagated in the upstream direction but also normal to the upstream in the form of parabolic patterns.

Since the velocity can be decomposed into each vertical mode, we decomposed the velocity

component u and found that those parabola patterns are created by mode-1 internal waves (Figure 5.4). Although those modes are modulated by the presence of the background shear current, $u_{o(z)}$, the decomposition worked well. The composition of the baroclinic modes-1, -2 and barotropic modes showed almost the same as the original field (Figure 5.5). We could see that not only mode-1 internal waves but also mode-2 internal waves emerged. These multi modal trapped internal waves have not been reported by the previous studies concerning atmospheric flow over a mountain.

To study the evolution of the internal wave further, time series of the displacement were measured from the temperature distribution (shown in dashed line in Figure 5.6) and by using the orthogonal relation (solid line in Figure 5.6). Although the background shear flow modulated the eigenvalue, both of the wave profiles agreed well except for the area very close to the cylinder. This exception was caused by a mode-2 internal wave as shown in Figure 5.4.

In Figure 5.6, the leading solitary waves were marked with red circles on its crest and the amplitudes are shown with typical value of 70 m. The non-dimensionalized amplitude a/D was 0.14 and the magnitude of quadratic nonlinear term in the KdV equation was estimated to be $\mu_1'^{-}(a/D) = 0.39$ where a is wave amplitude. So, the wave was certainly a nonlinear internal wave. The leading wave did not propagate at constant speed, so the ray-path was not straight. This was due to the background velocity field. The presence of the vertical cylinder required a stagnation point in front of it which makes the flow slow down as it approaches the cylinder. The wave continued to propagate upstream, but the propagation speed decreased as the wave propagated towards the upstream side. The wave did not exactly stop during the integration period, but it almost stopped at some point upstream.

According to linear theory, the phase speed was obtained by solving the eigenvalue problem which included background velocity. The upstream shear flow changed the linear long wave's propagation speed. The solution of eigenvalues showed that phase speed changed from 1.48 m/s to 1.25 m/s due to the effect of shear (Table 5.1). The nonlinearity increased, the speed and the magnitude was 0.159 m/s for leading wave by assuming the wave was a KdV solitary wave with amplitude of -70 m. In total, the wave propagated at 1.41 m/s. Since the upstream vertical mean velocity was 1.48 m/s, the wave could not propagate freely, but rather it was confined to the area where the background vertical mean velocity was less than the wave's propagating speed.

We wanted to see how the effect of wave dispersion in the simulation, so we conducted a hydrostatic simulation with same settings. Because of the nonlinear steeping effect, a shock like discontinuous line formed and the numerical dispersion became significant (Figure 5.7.). Therefore, the interfacial displacement around the discontinuity was not an real internal wave but just numerical noise. Although the finite volume method was used in the MITgcm, the nonlinear steepening effect of a large amplitude wave had a significant influence on the numerical calculation.

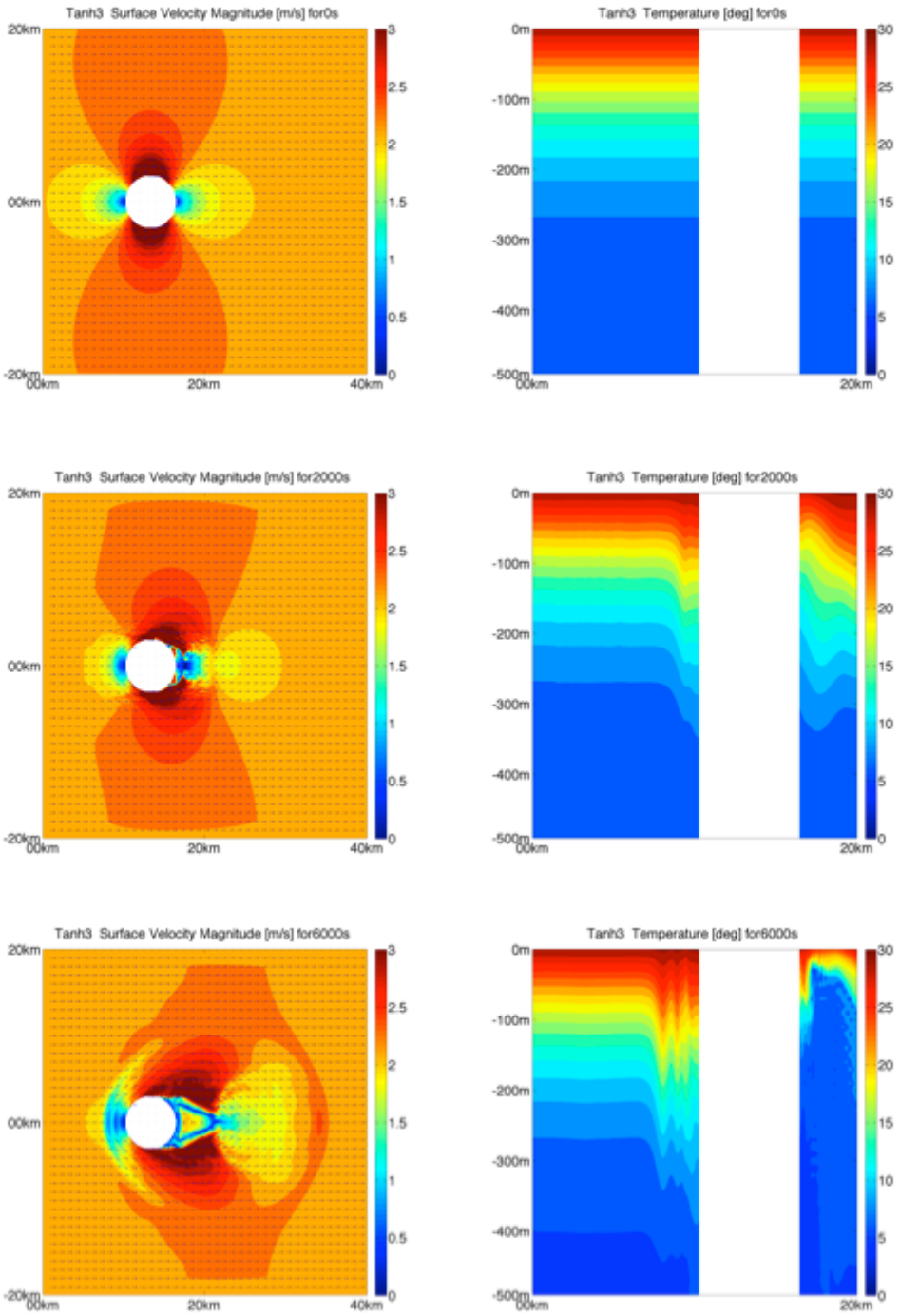

Figure 5.2 The time evolution of the velocity magnitude at surface (left) and temperature on a vertical section at y=0 (right) for the initial, 2000 s, 6000 s, and 10000 s.

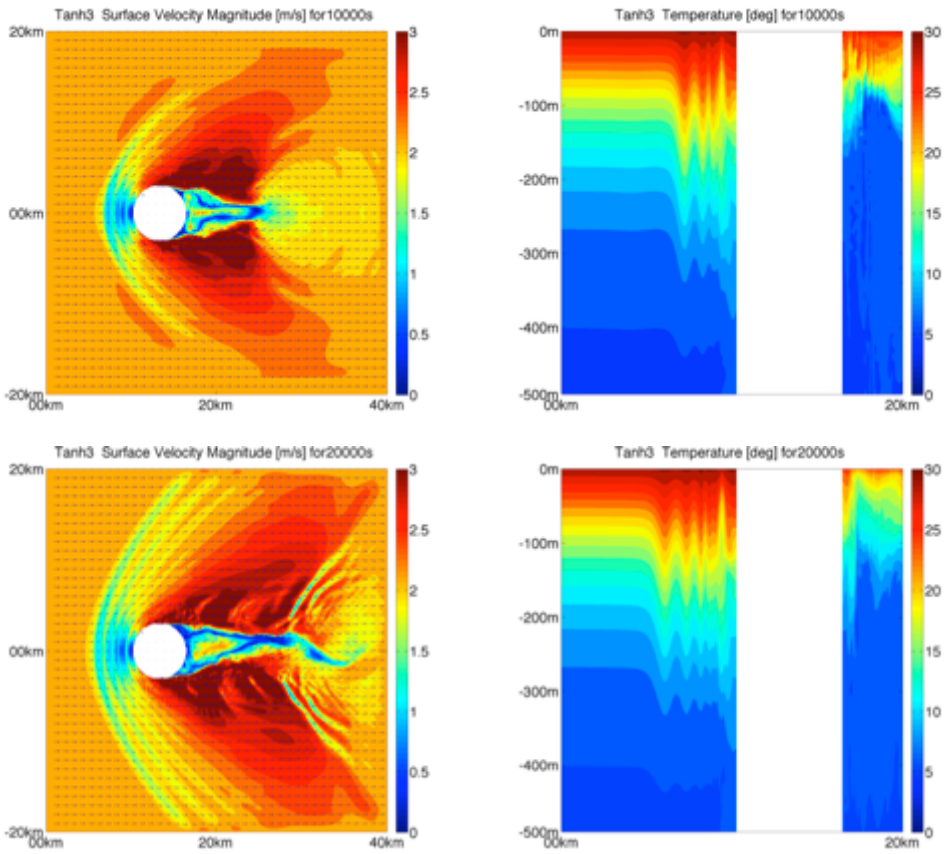

Figure 5.3 Same as Figure 5.2 but for the time of 10000s and 20000s after the simulation started.

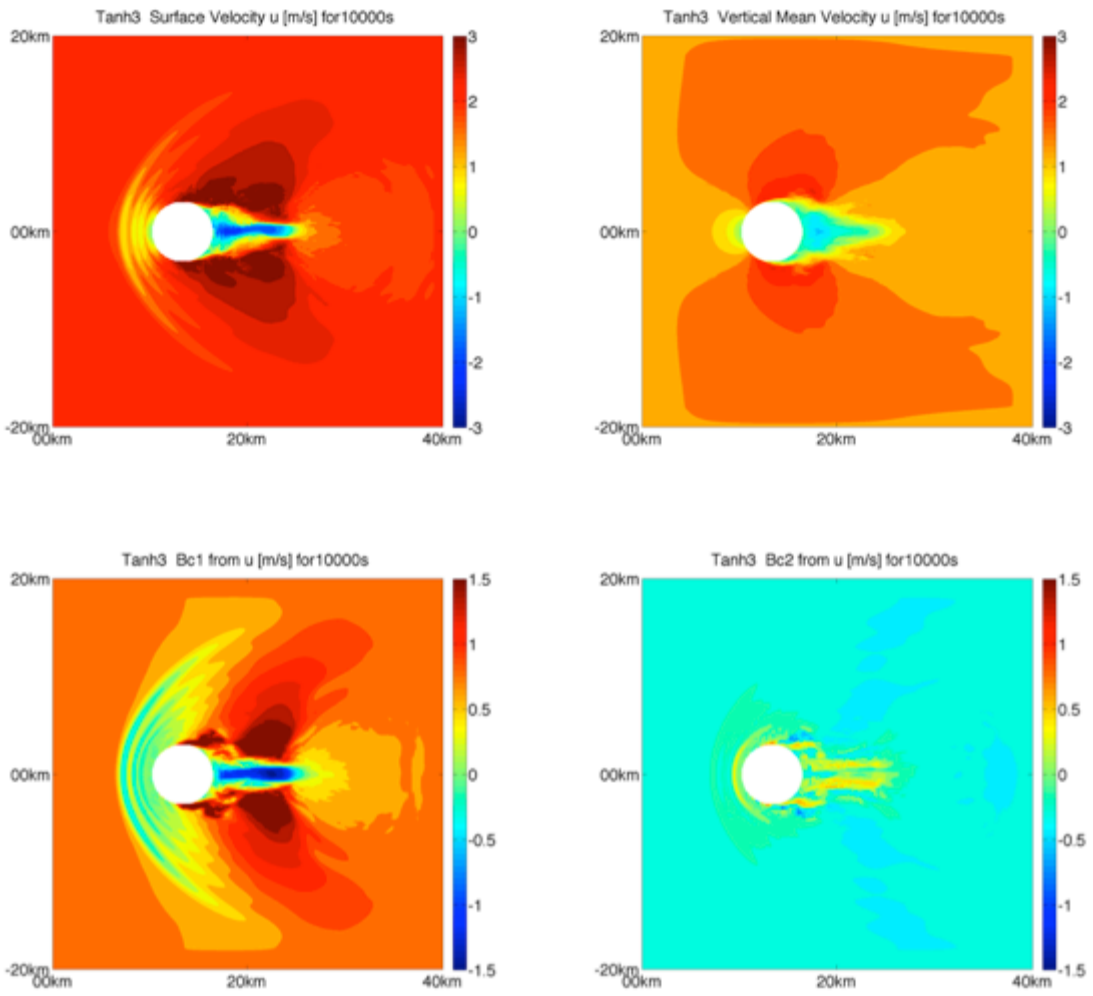

Figure 5.4 Surface velocity u and the contribution from each baroclinic modes.

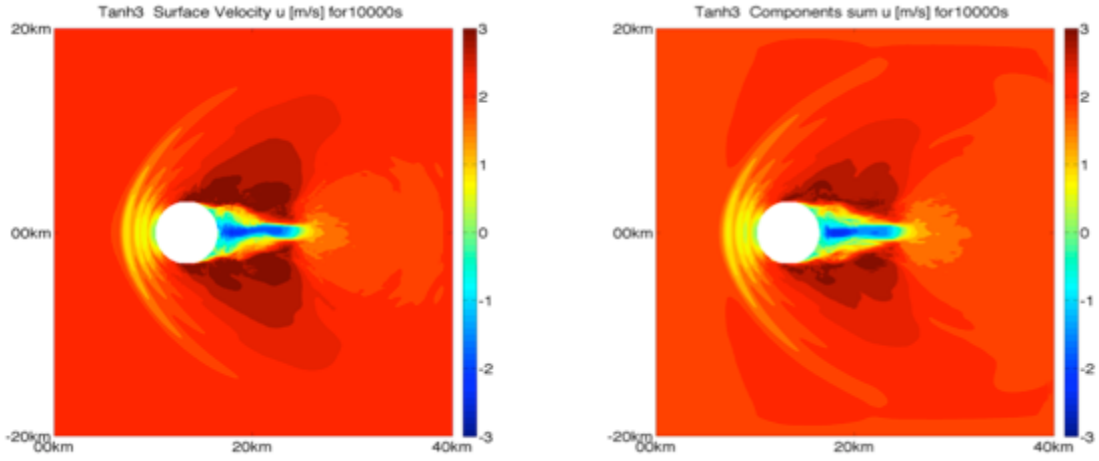

Figure 5.5 Surface velocity distribution of velocity component u (left) and the composition of the surface velocity u from barotropic mode, baroclinic mode-1 and baroclinic mode-2.

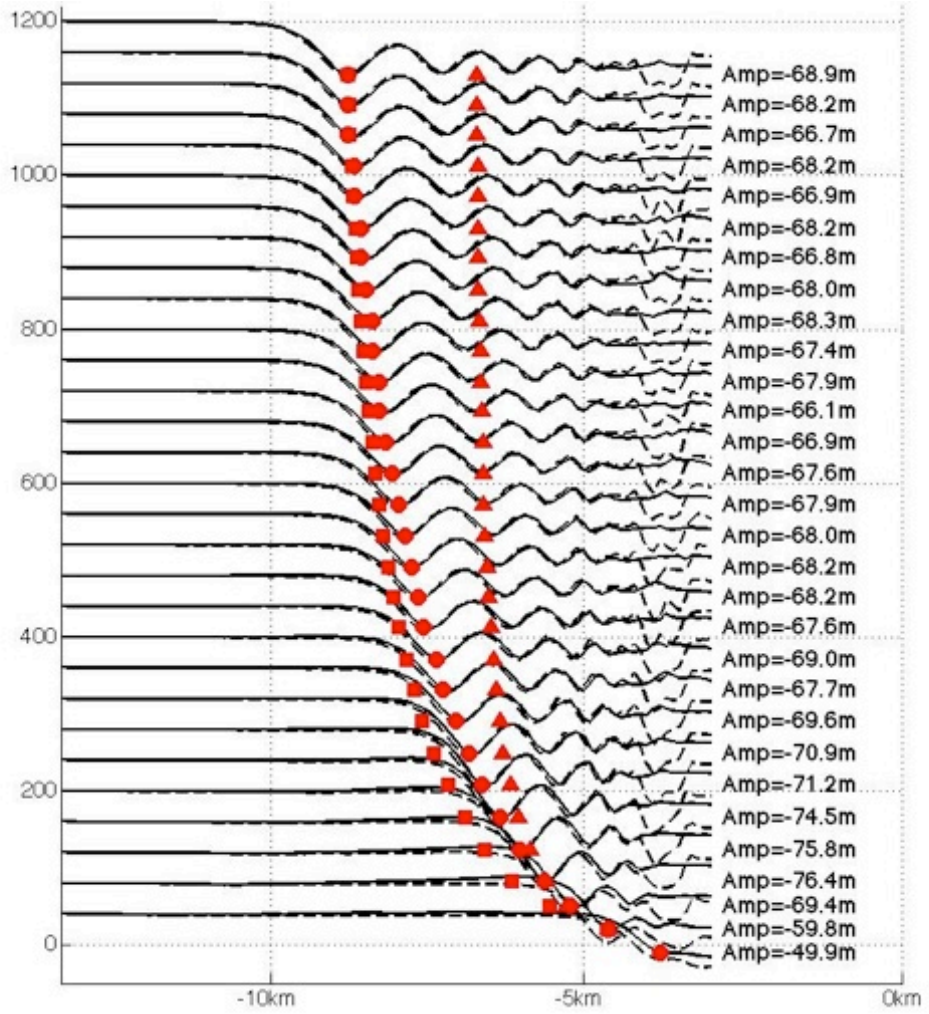

Figure 5.6 Maximum vertical displacement caused by baroclinic mode-1 estimated by linear relation from 2000s to 60000s (bottom to top) with interval 2000s. x-axis shows the position[km] and y-axis shows the wave displacement [m].

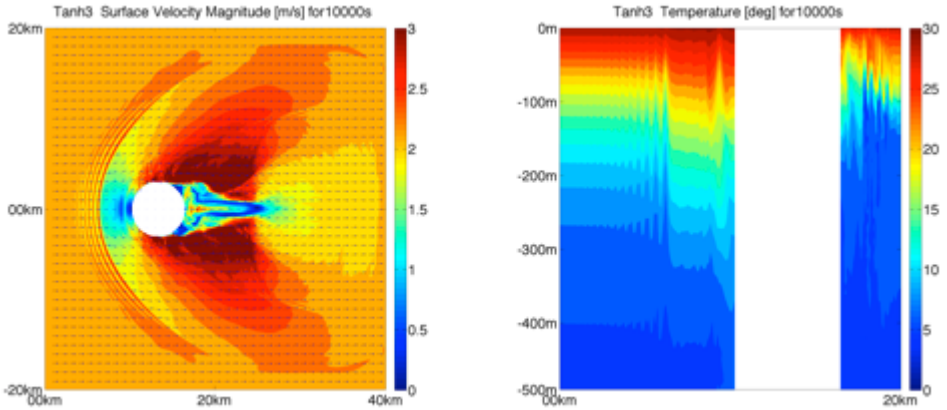

Figure 5.7 Results of hydrostatic simulation. The distribution velocity magnitude at surface (left) and temperature on a vertical section at y=0 (right) for the time 10000s.

5.1.3 Effect of Linearly Sheared Flow

5.1.3.1 Controlling Parameter and Internal Wave Properties

We tested the cases with Sc varying from zero to one with intervals of 0.2. As a result of previous subsection, the generated three-dimensional internal solitary wave reached the northern and southern boundary after 20000 s of simulation. Although the wave still propagated upstream, so we set a 30000 s integration time.

For the internal wave directed upstream, the properties are summarized in Table 5.2. As Sc increased, the phase speed increased. This is qualitatively explained by the formula for phase speed of internal waves for two-layer fluid case given by

$$c^{\pm} = \frac{u_2 d_1 + u_1 d_2}{d_1 + d_2} \pm \sqrt{\frac{d_1 d_2 (\Delta\rho g/\rho)}{(d_1 + d_2)} \left(1 - \frac{(u_1 - u_2)^2}{(\Delta\rho g/\rho)(d_1 + d_2)}\right)} \tag{5.1}$$

where u_1 and d_1 denote the upper layer fluid velocity and thickness, respectively, while u_2 and d_2 denote the lower layer fluid velocity and thickness. The $\Delta\rho$ is the density difference between the upper and lower layers, ρ is the referential density and g is the gravitational constant. In our case, the first term was positive and the second term decreased its magnitude with shear, $(u_1 - u_2)$, so the phase speed, c, for left propagating wave increased.

When Sc was larger than 0.6, the theory cannot be used because the eigenvalue problem became singular. The solution of the eigenvalue for the case $Sc = 0.6$ was significantly distorted as can be see in Figure 5.8. Nonlinear coefficient $\mu_1'^{-}$ decreased its value with Sc, while the dispersion coefficient λ' increased. This means that the background vertical shear flow decreased the nonlinearity and made the internal wave more dispersive.

Table 5.2 Internal wave properties for the each cases.

Sc	0.0	0.2	0.4	0.6	0.8	1.0
$c_1^- - U$	-1.480	-1.376	-1.290	-1.224	-1.221	-1.444
$\mu_1'^-$	-3.529	-3.407	-3.082	-2.317	0.390	-1.466
$\lambda_1'^-$	1.627	1.823	1.984	2.025	1.369	0.0066

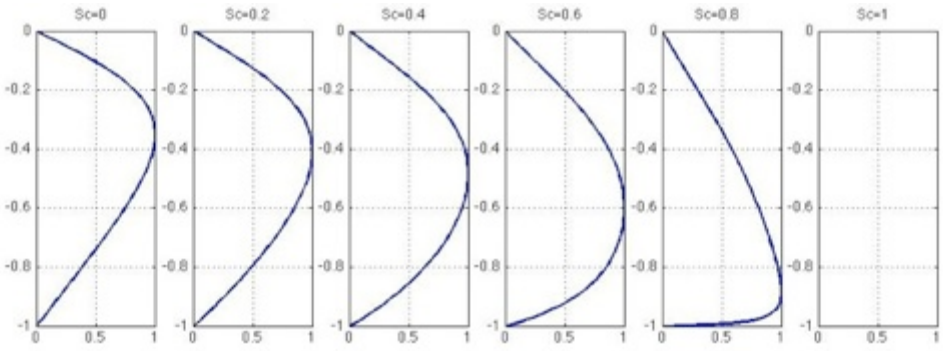

Figure 5.8 Vertical profile of the eigenvalue ϕ for each cases.

5.1.3.2 Results

When there was no vertical shear in the background flow, namely the case with Sc=0, no internal waves were generated on the upstream side until the end of numerical simulation. This can be interpreted as the vertically uniform flow only creates a barotropic disturbance

around the circular cylinder, and therefore no energy was transferred to a baroclinic mode.

Figure 5.9 shows the internal displacement profile for each case after 30000 s of simulation. As the Sc increased from 0.2 to 1.0, the amplitude of generated leading wave became larger. A relationship between upstream baroclinic component and the generated leading waves' amplitude was checked. The generated amplitude had magnitude close to the value of the upstream baroclinic component (Figure 5.10). Since the flow has to be stagnant at the cylinder, the baroclinic velocity component is required to be excited. Therefore, internal waves were generated and propagated to upstream.

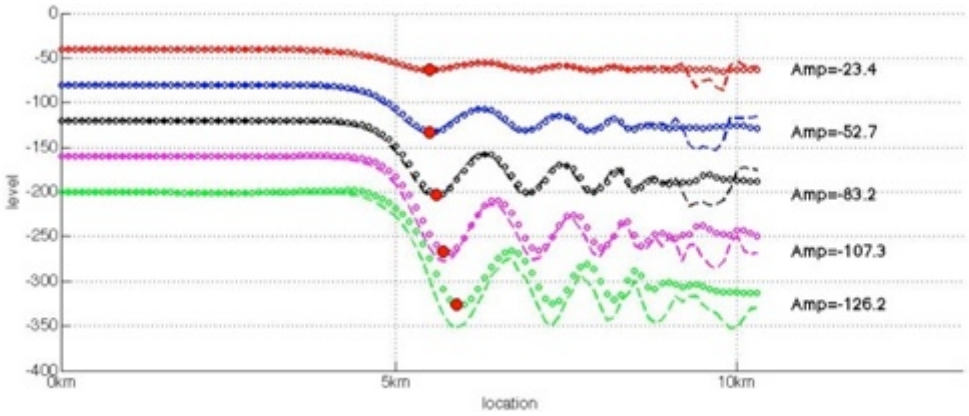

Figure 5.9 Internal displacement measured by temperature distibution (dashed line) and the mode-1 component (solid line) estimated by using orthogonal relation of eigenvalue. The color of the line changes for each case; red($Sc = 0.2$), blue ($Sc = 0.4$) , black ($Sc = 0.6$), masenda ($Sc = 0.8$) and green ($Sc = 1.0$).

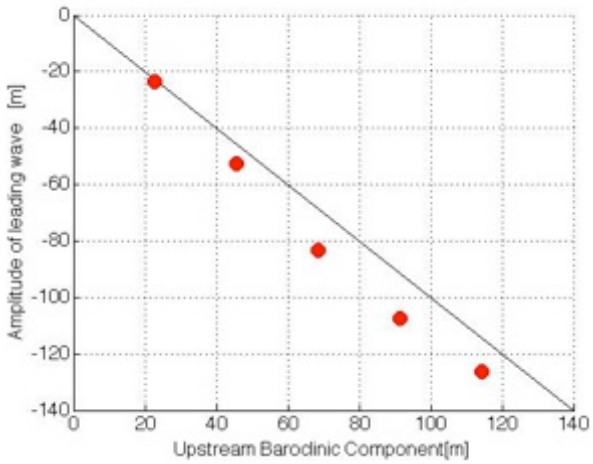

Figure 5.10 The relation between upstream baroclinic component and the generated amplitude. Upstream velocity profile is linear shear flow (red).

If the background density profile and velocity profile are same, weakly nonlinear theory for KdV solitary wave suggests that larger wave propagates faster. However, each case has different background flow and the larger wave does not necessarily propagate faster, rather the propagating speed is influenced by not only wave amplitude but also background shear flow. Figure 5.9 shows the larger amplitude wave propagates slower from the static frame of reference. If we apply the following formula to estimate phase speed for leading wave, each phase speed is estimated as shown in Table 5.3.

$$c_{KdV} = c + \frac{1}{3}\mu a \tag{5.2}$$

The values in Table 5.3 indicate that propagation speed decreases with Sc up to 0.6, but the difference between the values of the case for $Sc = 0.2$ and $Sc = 0.4$ was very small. Additionally, the numerical simulation showed that the two leading waves propagate with almost same speed. Compared to these two cases, the leading internal wave for the case $Sc = 0.6$ propagated more slowly. This result is qualitatively consistent with the estimated phase speeds shown in Table 5.3.

Table 5.3 Amplitude of the internal displacement induced by mode-1 internal wave estimated by using orthogonal relation and the propagating speed from the static frame of reference.

Sc	0.2	0.4	0.6	0.8	1.0
Amplitude	-23.4	-52.7	-83.2	-107	-
$c_1^- - U$	-1.48	-1.38	-1.29	-1.22	-
μ'^-_1	-3.53	-3.41	-3.08	-2.32	-
$c_{KdV} - U$	-1.45	-1.43	-1.38	-1.19	-
$\mu'^-_1 * (Amplitude/h)$	0.165	0.359	0.513	0.496	-

Figure 5.9 (right) shows the comparison between the numerical results of leading wave shape from the KdV solution with considering the background shear effect (dashed line) and without it (solid line). Since the polarity (sign of μ') was opposite when Sc = 0.8, and the solution was singular when Sc = 1.0, these two cases are not shown. Although the waves were three-dimensional solitary wave trains, both of the KdV solutions, with and without including background shear effects, fit well with the numerical results.

The case including background shear decreased the value of μ'^-_1/λ'^-_1 compared to the case without background shear. This indicates that background shear flow made the internal solitary wave broader. Choi and Camassa (1999) found that linearly sheared background flow changed not only the phase speed but also the shape of a large amplitude internal solitary wave in a two-layer system. The background vorticity created a solitary wave whose induced vorticity had the same sign as the background vorticity, and was smaller, wider, and slower, while the opposite was true when the solitary wave induced vorticity of the opposite sign. This nature was also reported for a numerical simulation of nonlinear internal waves in a continuously stratified shear flow by Statsna and Lamb (2002). The effect of background shear flow described in these previous studies was opposite to the KdV solitary wave solution in our findings. To explain this discrepancy, the effect of the background shear flow on the value of μ'^-_1/λ'^-_1 was checked. The density profile was close to that of the two-layer case. The density profile used was given by:

$$\rho_{(z)} = 1000 + 2.5 * \tanh\big((z + 100) * 0.04\big), \qquad -500 < z < 0$$

and the profile is shown in Figure 5.11. With the same background shear flow tested in this subsection, phase speeds and values of μ'^-_1/λ'^-_1 for each case were calculated as shown in Table 5.4. This result shows that the effect of background shear flow depended on the density

profile. For a sharp interface, well approximated to two layer case, the results of Choi and Camassa (1999) may be applied. On the other hand, if the density profile changes gradually, these results are not applicable. Since the density profile used in Statsna and Lamb (2002) was close to a two layer configuration, the effect of background shear flow on the internal solitary wave was consistent with Choi and Camassa (1999).

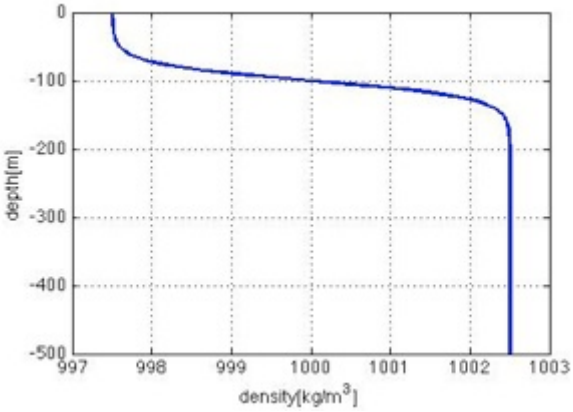

Figure 5.11 Density profile close to two-layer configuration.

Table 5.4 Effect of background shear flow on the internal wave in continuously stratified fluid close to two- layer configuration.

Sc	0	0.2	0.4	0.6	0.8	1.0
$c_1^- - U$	-1.84	-1.75	-1.67	-1.59	-1.50	-
$\mu_1'^-/\lambda_1'^-$	-4.51	-4.72	-4.89	-4.85	-4.93	–

When Sc was 0.8, weakly nonlinear theory predicted that the polarity changed and a depression type internal solitary wave should not have emerged. However, our numerical results showed depression type internal solitary waves. This means that weakly nonlinear theory was not valid for those large amplitude internal waves. Furthermore, both the density and velocity profiles were modified by both the internal displacement and the velocity induced by the internal wave. These modified profiles were far from the referential vertical profiles. Actually, the vertical profile of displacement at the trough of the leading internal wave differed from the shape of eigenfunction, and the difference was larger for the cases with larger Sc (Figure 5.13). The peak of the eigenfunction for the case of Sc = 0.8 was located at z = -460, but the numerical results showed the peak located at z = -220. This correction of the vertical profile of displacement was due to the higher order terms which were neglected in the linear theory. This correction is further studied in the next subsection.

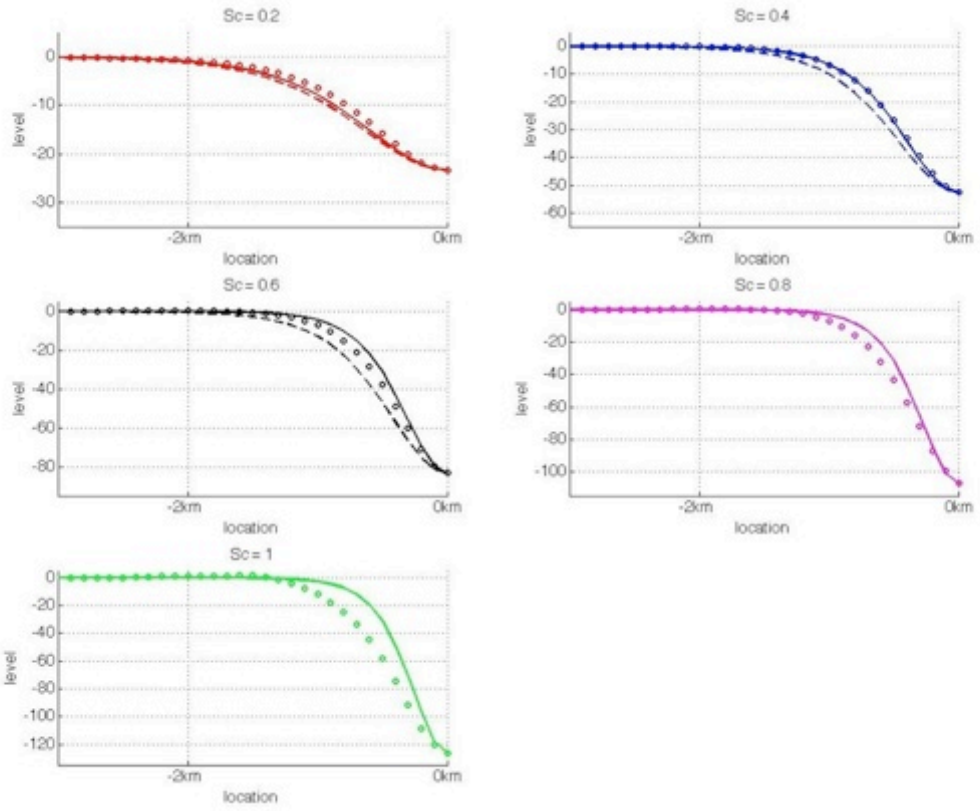

Figure 5.12 Shape of the leading internal wave calculated by using orthogonal relation (○) and the KdV solitary wave solution without background shear (solid line) and with bakcground shear flow (dashed line). The color of the line changes for each case which is consistent to the Figure 5.9; red($Sc = 0.2$), blue ($Sc = 0.4$) , black ($Sc = 0.6$), masenda ($Sc = 0.8$) and green ($Sc = 1.0$).

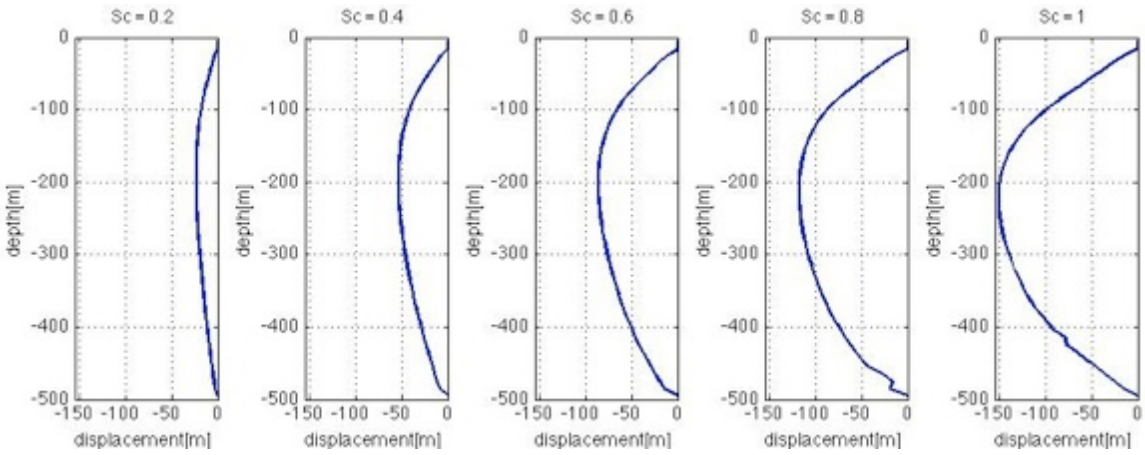

Figure 5.13 Vertical profiles of displacement at the trough of the leading internal waves.

5.1.4 Correction of the Vertical Mode with Large Amplitude

Since there were significant difference on the vertical modes between the ones predicted by linear theory and numerical simulation results, finite amplitude effect on the correction of the vertical mode is studied by conducting two-dimensional numerical simulation. The density profile is same as the one used in previous sub-subsection but there is no background

flow. Numerical domain is 32km wide in horizontal and 500m deep in vertical and periodic boundary condition is applied. There is no velocity at initial state and salinity is not considered in this simulation. Initial temperature distribution is created to compose KdV solitary wave solution determined by the following distribution of the displacement.

$$\zeta(x,z) = \eta_o \,\mathrm{sech}^2\left[\frac{x}{L_{KdV}}\right]\phi(z) \quad , \qquad L_{KdV} = \sqrt{\frac{12}{\eta_o}\frac{\lambda}{\mu}} \tag{5.3}$$

An example of this initial distribution of temperature is shown in Figure 5.14 (top). To evaluate the nonlinear effect, the cases with $\eta_o = -50, -100, -150, -200$ and -250 were tested.

The initial depression decomposed into two internal solitary waves which propagated left and right (Figure 5.14, bottom). After 5000 s of simulation, the emerged internal solitary wave became steady for every case. We analyzed the vertical profile of the displacement and velocity induced by the steady internal solitary wave. Since the situation was perfectly symmetric, only the left going internal solitary wave was analyzed.

The series of results show that the vertical profile of the induced displacement changed with internal solitary waves of larger amplitude, and the level of maximum displacement approached the top boundary (Figure 5.15, left). The nature of the nonlinearity was described by the results obtained in previous sub-subsection. The effect of background shear flow and the nonlinearity was opposite. So, the vertical profiles of displacement did not follow the linear theory and kept a profile close to one without background shear flow. Compared to the displacement profile, velocity was not influenced by finite amplitude effect (Figure 5.15, right).

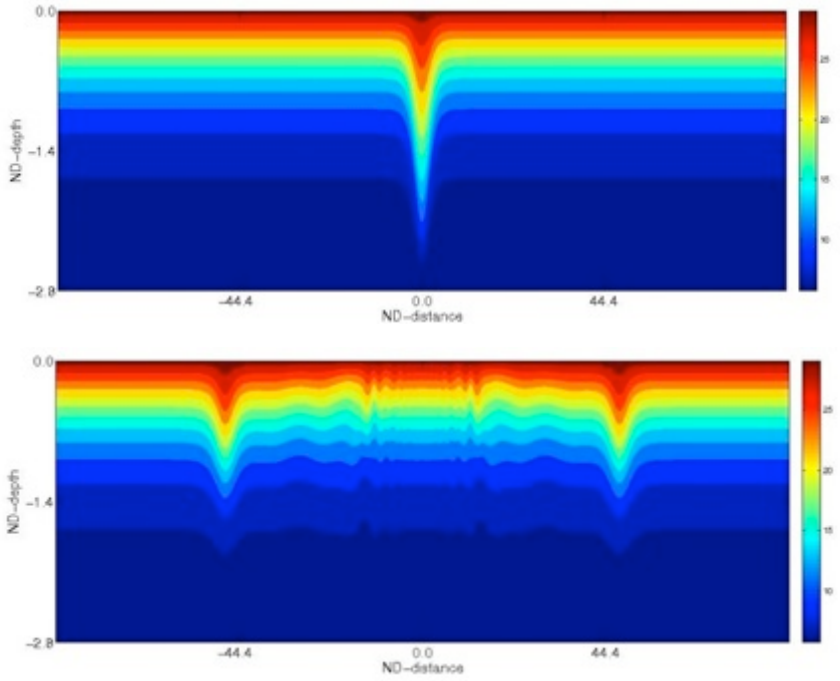

Figure 5.14 Initial distribution of the temperature (top) and the distribution after the time integration of 5000s.

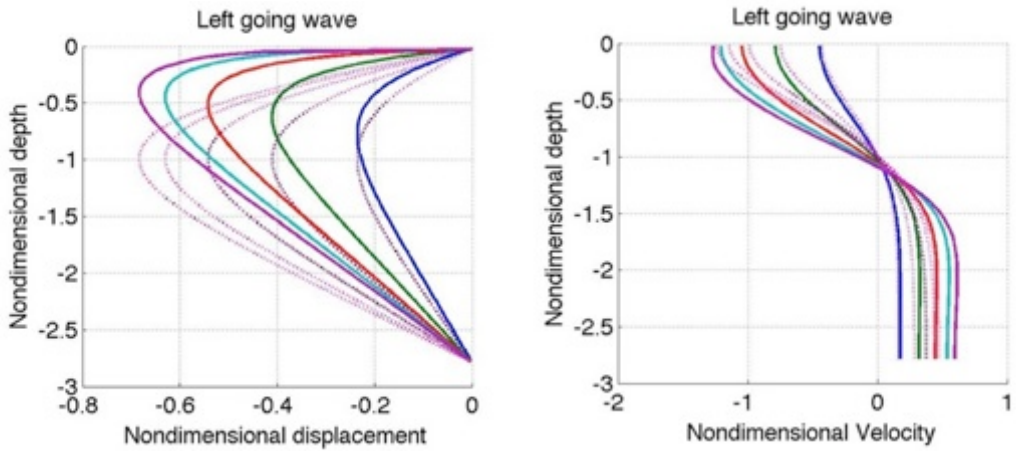

Figure 5.15 Vertical profiles of the displacement and velocity induced by internal solitary waves. Solid lines show the numerical results, while dashed line shows the vertical mode multiplied with the amplitude from numerical results. The color of the line changes for each case ; blue ($\eta_o = -50$), green ($\eta_o = -100$), red ($\eta_o = -150$), cyan($\eta_o = -200$) and purple ($\eta_o = -250$)

5.1.5 Exactly Critical Situation

Although there should be little difference, the exactly critical situation for the linear shear flow was also examined. To construct an exactly critical situation, background shear flow was given as follows for the eigenvalue problem.

$$u_{o(z)} = Lc(1 + 2 * z/D) \qquad -D < z < 0 \tag{5.4}$$

Then the solution of the eigenvalue, c, was subtracted from the background flow (5.4) as an additional vertical mean flow. As a result, the following velocity profile was obtained for construction of an exactly critical situation in the linear wave case.

$$u_{o(z)} = Lc(1 + 2 * z/D) - c \qquad -D < z < 0 \tag{5.5}$$

The following series of cases was studied: $Lc = 0.2, 0.4, 0.6, 0.8,$ and 1.0. Since the internal wave propagated further upstream, compared to the previous numerical simulations for supercritical cases, the cylinder was moved to the center of domain. The other numerical configurations were not changed.

Results again showed a series of internal solitary wave trains (Figure 5.16), and the leading wave was close to the KdV solitary wave solution (Figure 5.17).

Table 5.5 Internal wave properties for linearly sheared flow determined by Lc.

Lc	0.2	0.4	0.6	0.8	1.0
c_1^-	-1.4113	-1.341	-1.2876	-1.238	-1.216-
$\mu_1'^-$	-3.468	-3.309	-3.082	-2.654	-1.990

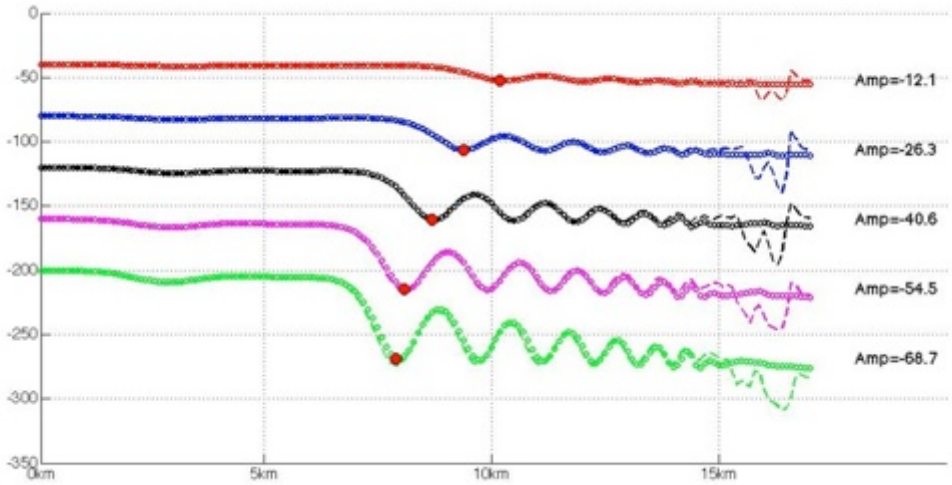

Figure 5.16　Internal displacement measured by temperature distibution (dashed line) and the internal displacement induced by mode-1 internal wave (solid line) estimated by using orthogonal relation of eigenvalue. The color of the line changes for each case ;　red($Lc = 0.2$), blue ($Lc = 0.4$) , black ($Lc = 0.6$), masenda ($Lc = 0.8$) and green ($Lc = 1.0$).

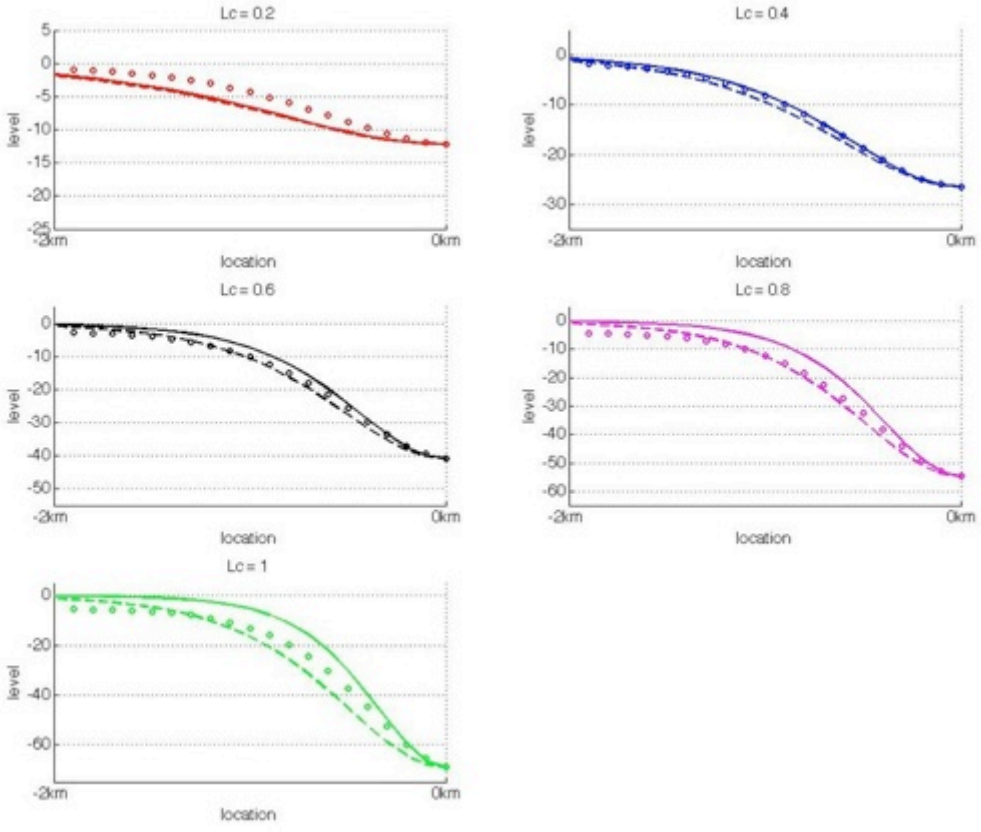

Figure 5.17　Shape of the leading internal wave calculated by using orthogonal relation (○) and the KdV solitary wave solution without background shear (solid line) and with bakcground shear flow (dashed line). The color of the line changes for each case which is consistent to the Figure 5.16; red($Lc = 0.2$), blue ($Lc = 0.4$) , black ($Lc = 0.6$), masenda ($Lc = 0.8$) and green ($Lc = 1.0$).

5.1.6 Bottom accelerated Vertical Linear Shear Flow

A series of numerical simulations showed that the vertical shear flow induced a mode-1 internal wave which propagated upstream. This begged the question: how does the situation change if a negative value of Lc is set for the numerical simulation? Since the nonlinear internal wave has polarity, the sign of Lc should influence the development of the nonlinear internal wave.

The exactly critical case, given by setting $Lc = -0.6$, was studied. The result showed no disturbance propagating upstream. Since the upstream shear flow moved the interface upward in this situation, the propagating speed of the mode-1 internal wave should have decreased. This is analogous to how internal waves in a two-fluid system change speed depending on the upper and lower layer thickness. Namely, the finite amplitude disturbance in this situation reduced its speed, while the nonlinear internal wave examined in previous sub-subsection increased its speed. The disturbance considered to be rarefaction or the negative wave: a disturbance whose leading part travels faster than the trailing part (Lawrence, 1993). This result implies that a perturbation induced by the background shear also has polarity much like the topographic forcing.

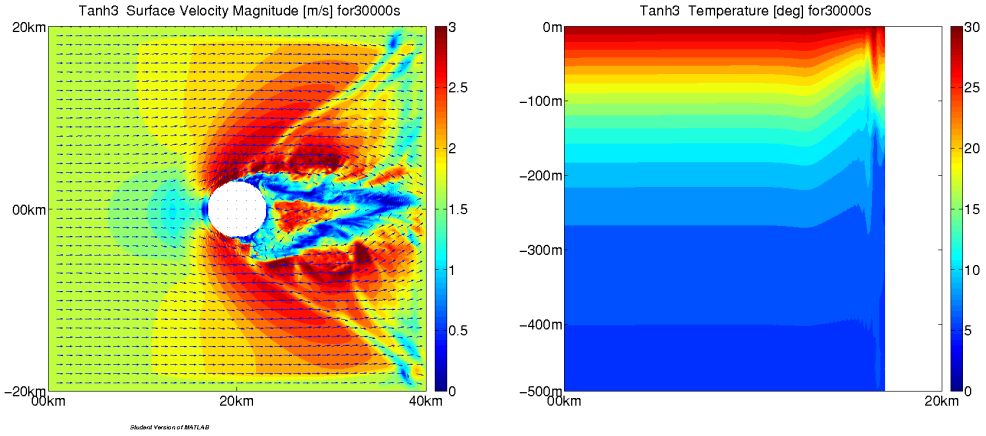

Figure 5.18 Results of numerical simulation with setting background shear flow speed to decrease with depth. The distribution of velocity magnitude at surface (left) and temperature on a vertical section at y=0 (right) for time = 30000 s.

5.1.7 Critical Situation for Mode-2 Wave

Exactly critical situation for mode-2 internal wave is also studied. The cases with $Lc = 0.2, 0.4,$ and 0.6 were tested.

Table 5.6 Internal wave properties for mode-2 waves with linearly sheared flow.

Lc	0	0.2	0.4	0.6
C	-0.69	-0.630	-0.603	-0.64
μ'^{-}_{2}	-1.59	-1.57	-1.07	0.929

The results were considerably different from the mode-1 wave cases examined above. Even in the most strongly sheared case (Lc = 0.6), the background shear flow induced only a small amplitude wave as shown in Figure 5.19. This indicates that the background shear flow has a structure that induces a small component of the mode-2 internal wave.

Although the mode-2 internal wave was hardly detected, the numerical simulation showed that the mode-1 internal wave changed the background density and velocity profiles as the mode-1 wave propagated upstream (Figure 5.19, top). The displacement remained after the passage of the mode-1 wave. This kind of disturbance is known as *columnar mode*. The columnar mode is a mode with a wavenumber of zero, so the phase does not vary with position. It can be recognized that the leading mode-1 internal solitary wave was a transient state from one steady situation to another steady situation. The dynamics were similar to the development of a bore described in Peregrine (1969) introduced in subsection 2.1.

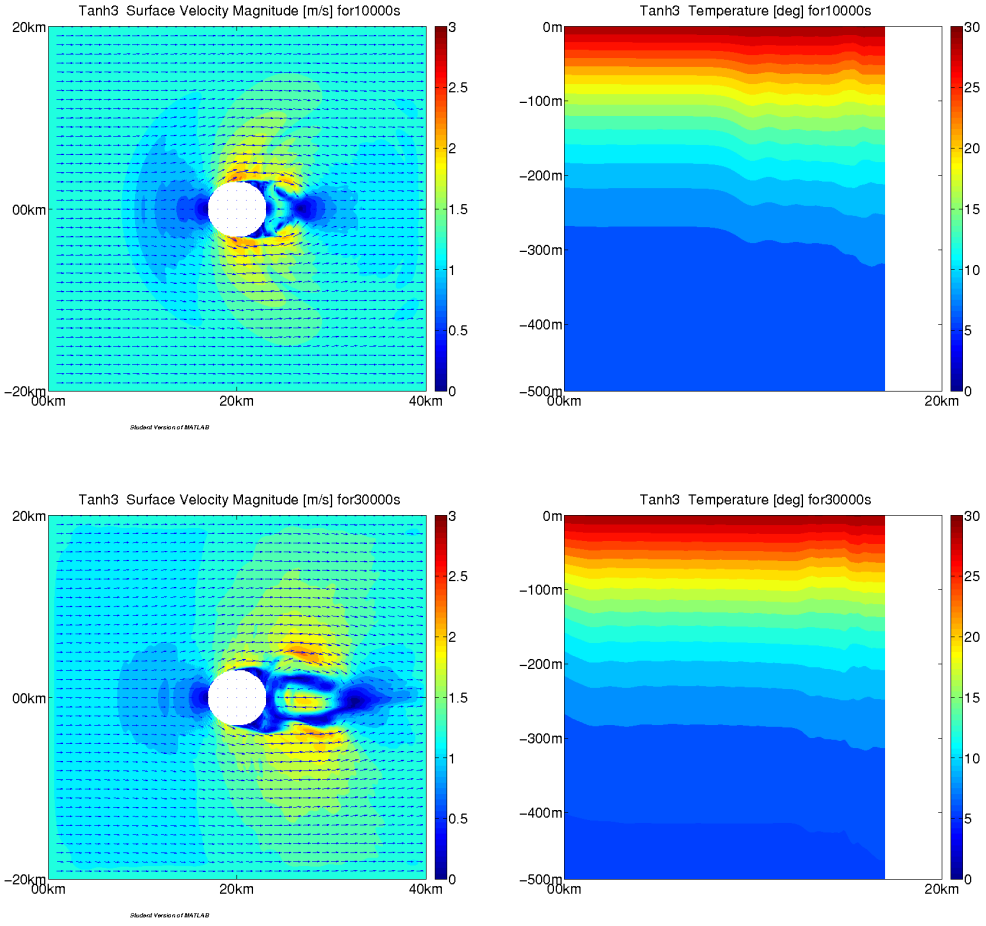

Figure 5.19 Results of exactly critical situation for mode-2 waves with setting Lc = 0.6. The distribution velocity magnitude at surface (left) and temperature on a vertical section at y = 0 (right) for the time at 10000 s (top) and 30000 s (bottom).

5.2 Vertically Uniform Flow over the Gaussian Bell Topography

5.2.1 Numerical Model Settings

We selected the following Gaussian Bell type topography as a representative of the island topography.

$$d(x,y) = -H + H * \exp\left(\frac{r_{surf}^2 - r^2}{\left(T_s * r_{surf}\right)^2}\right) \quad r > 0 \tag{5.6}$$

$$r = \sqrt{(x - x_c)^2 + (y - y_c)^2}$$

where x_c and y_c is the position for the center of the topography. We set $T_s = 4$ which makes the radius of topography about double at $z = -H/2$.

The background flow, $u_{o(z)}$, was vertically uniform and numerical experiments were conducted with $u_{o(z)}$ = 0.6 c, 0.8 c , and 1.0 c. For the initial conditions, a horizontally uniform temperature field was set. The velocity distribution was set as the analytical solution of steady irrotational flow around the cylinder. Brighton (1978) showed that when the situation was strongly stratified, flow field around the mountain topography of maximum height, h, was decomposed to an asymptotic series by expanding the small parameter, U/hN, where U was background flow speed and N was the Brunt-Vaissala frequency. In the physical limits of slow flow speed, strong stratification, and great mountain height, the flow could not go over the mountain but must pass around. Therefore, potential flow around a cylinder develops at each level. This theory was first developed by Drazin (1961) and then expanded by Brighton for the case of vertically changing U(z) and N(z). The value of U/hN was not so small in our configuration because the orders of the each variable are U = O(1), h = O(10^2), and N = (10^{-2}-10^{-3}). Therefore, the application of the theory of Brighton (1978) is not valid. However, the solution might reduce the initial disturbance of the barotropic wave. Horizontal boundary conditions were steady and a sponge layer of the 20 km was attached to all four boundaries.

To avoid the effect of the boundaries, the numerical domain was enlarged to be 60 km by 60 km in horizontal dimension. The topography was located at the center of domain. Numerical integration was conducted for 60000 s for every case.

5.2.2 Result of Critical Situation for Mode-1 Internal Wave Upstream

As the numerical simulation started, the interface were raised up in front of the Gaussian bell topography, and the surface velocity field in front of the topography showed acceleration. This acceleration created a parabolic pattern (Figure 5.20, top). After the first 10000 s of simulation, a perturbation with negative vertical velocity appeared, and the interface became vertical at t = 4000s (Figure 5.20, right panels). The disturbance was an excited mode-1 internal wave, and the situation was similar to an internal hydraulic jump with the sudden decrease of the surface velocity (Figure 5.20, bottom, left). However, the disturbance was advected downstream with time and eventually became unstable (Figure 5.21). Although the situation was critical at the upstream side, the Froude number changed with position because of the background velocity and topography.

On the other hand, there was another nonlinear internal wave generated from the side of the island topography. The nonlinear wave was clearly seen from the distribution on the surface velocity induced by a mode-1 internal wave (Figure 5.22). At first, there was only one wave, but as the time integration continued, a wave train appeared. The transformation seemed to be triggered by the internal wave generated in front of the island topography which was considered in the previous paragraph. The interaction between the nonlinear internal waves is an interesting topic, but further discussion is outside the scope of this thesis.

Other modes were not clearly shown in the results of numerical simulation. Since the fastest mode-1 internal wave was supercritical, other modes were also supercritical. It may be possible that some modes were confined around the island topography, but they could not be detected clearly in our numerical simulation.

It should be stressed that a depression type nonlinear internal wave appeared in front of the island topography, while weakly nonlinear theory predicts the topographic forcing encourages generation of elevation type internal waves. This indicates that the disturbance which was excited around island topography was too large for weakly nonlinear theory to be applicable.

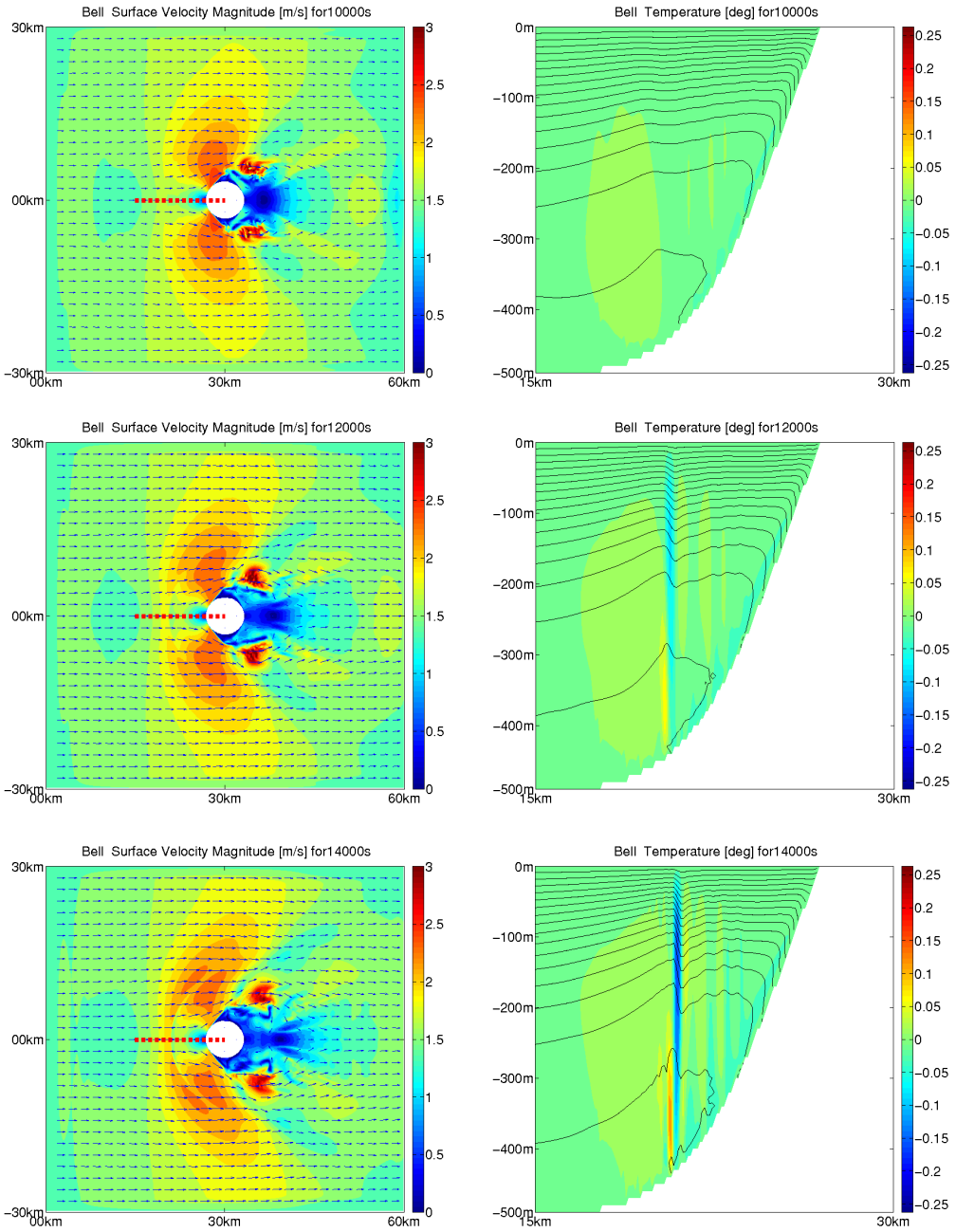

Figure 5.20 Surface velocity distribution (left column) and the distributions of temperature (contour) and vertical velocity (color) in the vertical section shown in red dashed line in left panels for the case Fr = 1.0. The panels are for times t = 10000 s (top), 12000 s (middle) and 140000 s (bottom) after the simulation started. Contour lines for temperature are shown every 1 degree.

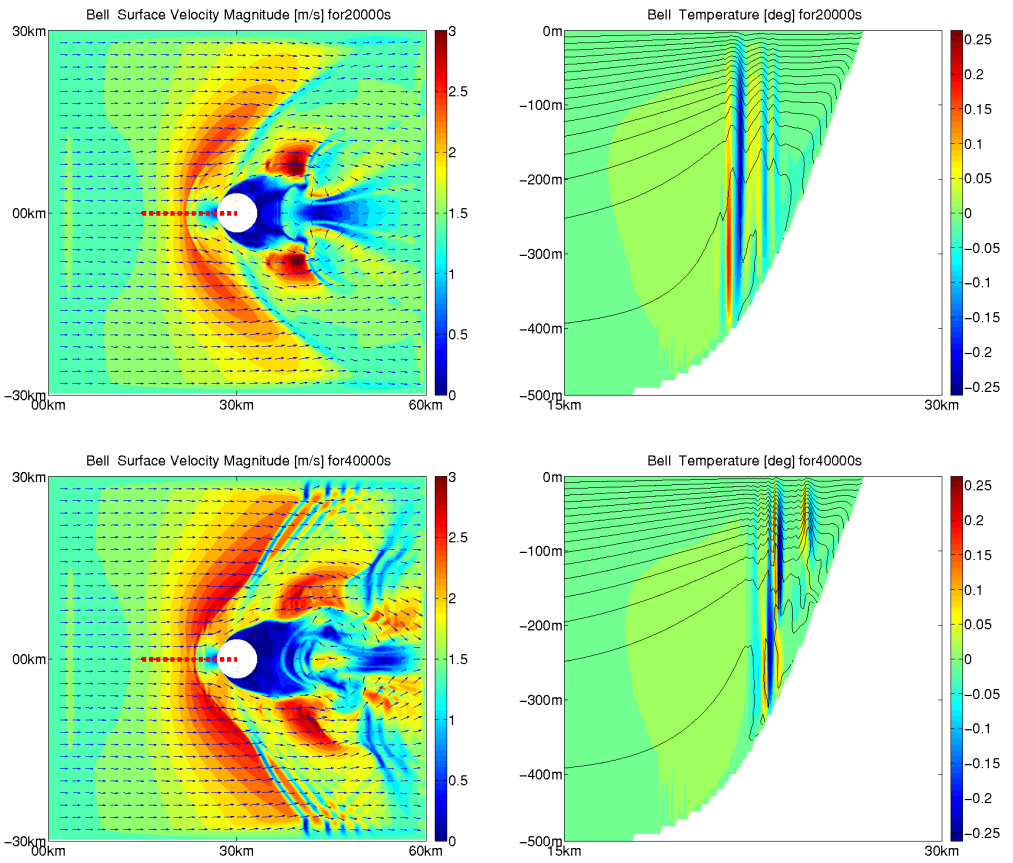

Figure 5.21 Same as Figure 5.20 but for the time of 20000s(top) and 40000s(bottom)

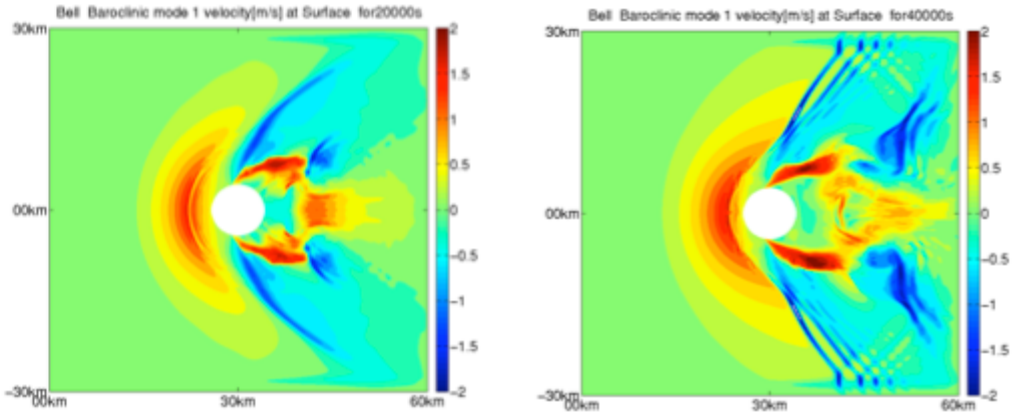

Figure 5.22 Surface velocity induced by mode-1 internal wave for the time of 20000s (left) and 40000s(right). The velocity distributions were calculated by using orthogonal relation. Since the topography changes, eigenvalues for initial stratification without considering background velocity at each depth were used.

5.2.3 Result of Subcritical Situations for Mode-1 Internal Wave Upstream.

Subcritical flow ($Fr = 0.6, 0.8$) was also examined, When the Froude Number was 0.6 at upstream, a mode-2 internal wave was generated in front of the topography at t = 20000 s, but the wave propagated downstream (Figure 5.23). Then, a mode-1 internal wave was generated in front of the topography at t = 40000 s. The mode-1 internal wave did not propagate and was amplified with time. The isothermal line became vertical as shock if the dispersive effect was absent. Since the numerical simulation was conducted without the hydrostatic approximation, an undular, bore-like disturbance emerged instead of the shock.

According to weakly nonlinear theory (fKdV), the topographic forcing effect for each mode depends on the first derivative of the sea bottom shape. Therefore, only the positive or negative anomaly was forced for each mode. For the mode-1 wave, the effect was in the opposite direction to the generated depression type nonlinear internal wave. However, the numerical simulation showed a depression type disturbance with negative vertical velocity. The discrepancy was resolved by induced mode-1 component of the velocity. The induced velocity might be responsible for the production of the depression type anomaly.

The result of the other subcritical situation (Fr = 0.6) showed a trapped mode-2 internal wave. The wave also increased its amplitude and produced a parabolic pattern in the surface velocity distribution (Figure 5.24). The setting of the Froude number to 0.6 was for the mode-1 internal wave, and the Froude number for mode-2 was 1.29 in the simulation, so the mode-2 was supercritical at upstream side.

The series of experiments showed that at least one of the trapped internal waves appeared . Formally, there are infinite numbers of baroclinic modes in ocean, so one of the modes can reach a critical value regardless of the background velocity. We showed that the trapped mode changed from mode-1 to -2 gradually as we decreased the background flow speed. This implies that some mode can be trapped off the Izu islands.

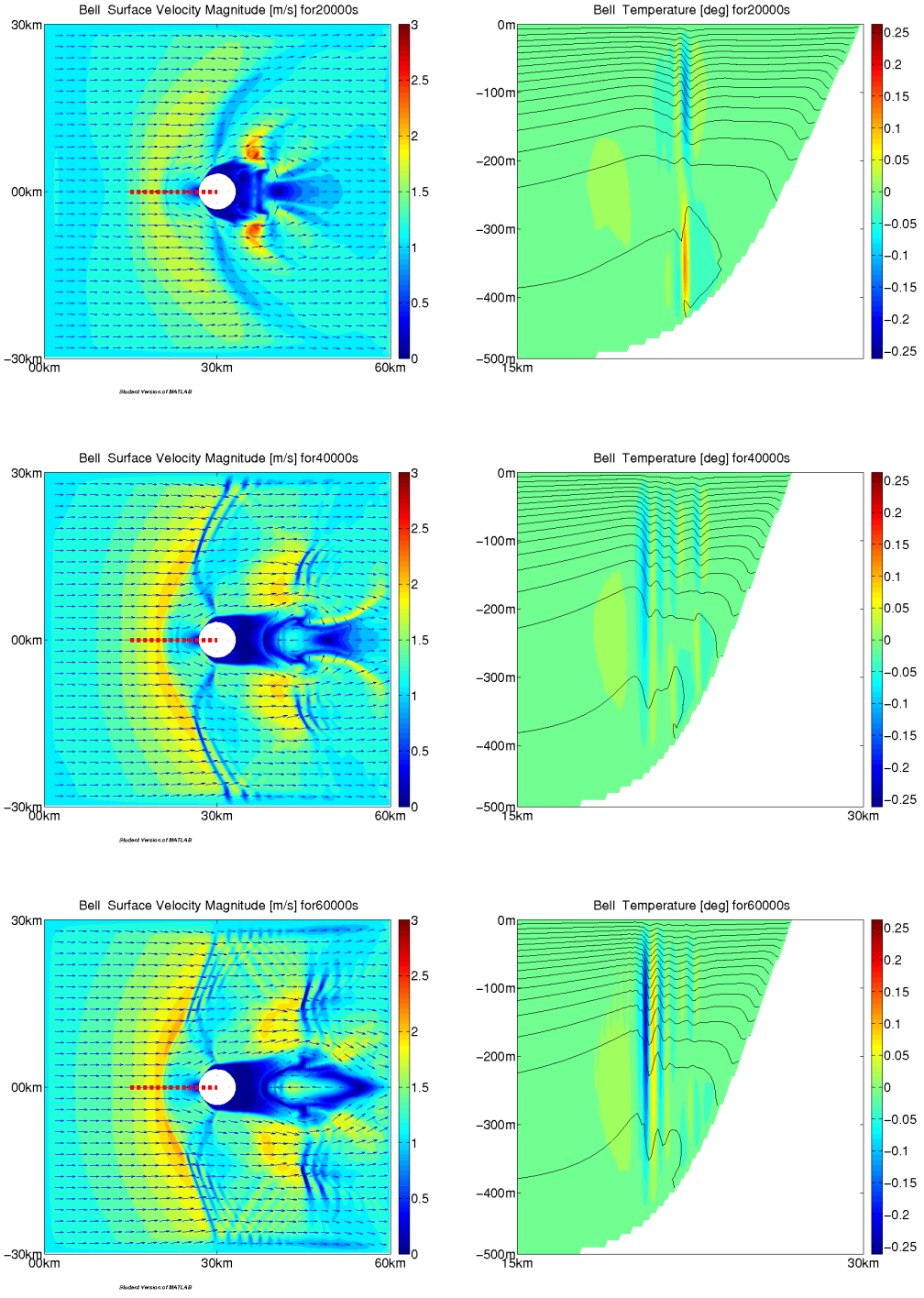

Figure 5.23　Surface velocity distribution (left column) and the distributions of temperature (contour) and vertical velocity (color) in the vertical section shown in red dashed line in left panels for the case Fr=0.8. The panels are for the time t=10000s(top), 12000s(middle) and 140000s(bottom) after the simulation started. Contour lines for temperature are shown with every 1 degree.

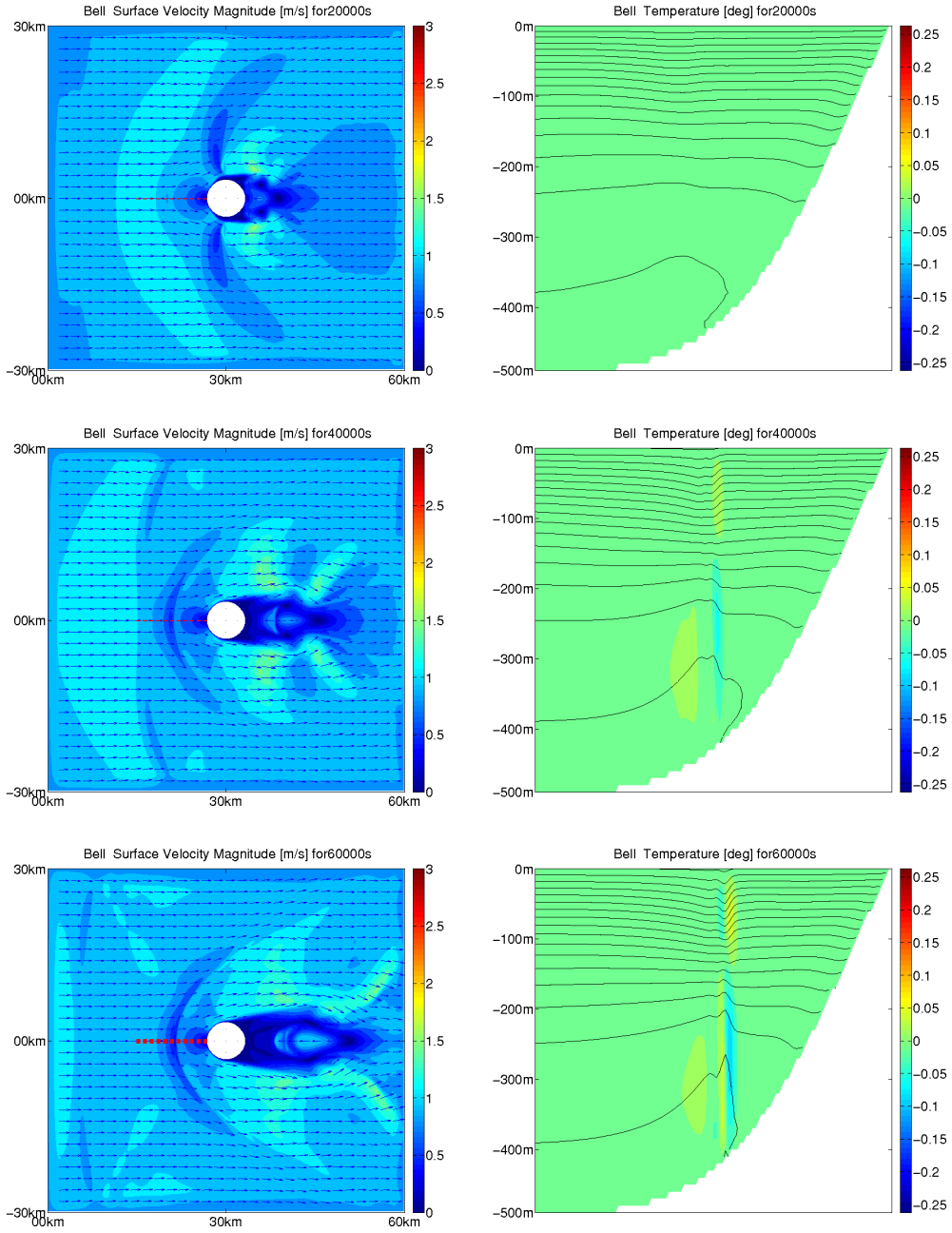

Figure 5.24　Surface velocity distribution(left column) and the distributions of temperature (contour) and vertical velocity (color) in the vertical section shown in red dashed line in left panels for the case Fr=0.6. The panels are for the time t=10000s(top), 12000s(middle) and 140000s(bottom) after the simulation started. Contour lines for temperature are shown with every 1 degree.

5.3 Linearly Sheared Flow Past the Islands Topography, the Case of Miyake and Mikura Islands

Results of numerical simulations in previous sections revealed that both the background shear flow and topography induced finite amplitude internal waves, and the near critical background flow trapped internal waves around the topography. Unlike the case of linearly sheared flow over Gaussian bell topography, the case of the Kuroshio past the Miyake and Mikura Islands has many parameters to be examined. We therefore focus our attention on the generation mechanism of the mode-2 nonlinear internal waves.

5.3.1 Numerical Model Settings

The numerical domain for the calculation was a square box of 60 km by 60 km in horizontal dimension and 1000 m deep. To model the island topography, we made the scatter plot of distance from the center of the island and sea bottom depth. The centers and area concerned are shown in Figure 5.25 (top). Gaussian bell topography was again used to model the two islands, and the topography was given by (5.6). Here, $T_s = 1$ and $T_s = 6$ for the model topography of Mikura and Miyake Islands, respectively. The shape of topography is shown in Figure 5.25 (bottom).

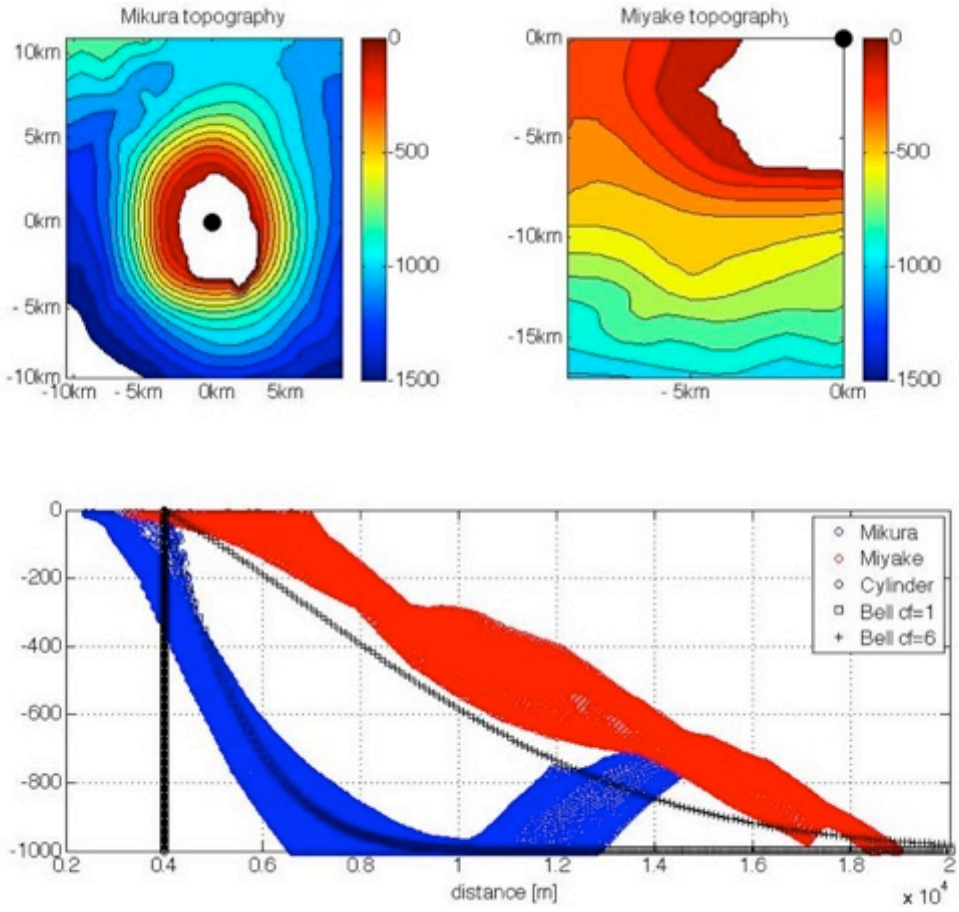

Figure 5.25 Topography around the Mikura and Miyake islands (top) with black circle indicating the center of the island defined to create model topography for the islands. Scatter plot of the distance from the center of topography and the sea bottom depth (bottom).

Since the SAR images with parabolic patterns were obtained when the vertical mean flow speed of the Kuroshio axis was large, the linearly sheared flow with vertical mean speed of 0.8 m/s was applied to the numerical simulations. The velocity changed linearly from 1.6 m/s at surface to 0 m/s at bottom. With this background shear flow, the density profile defined by (4.1) with $cf = 4$ was used for the boundary conditions. Internal wave properties for the density profile were calculated (Table 5.7). The density profiles composed super critical flow at the far upstream for mode-2 waves because the vertical mean speed of the flow was 0.8m/s

The initial and boundary condition was the same as the cases described in the previous subsection. The other numerical configuration was the same as the one used in the subsection 4.3.1. Numerical integration was conducted for 40000 s.

Table 5.7 Internal wave properties for the density profiles used in numerical simulation.

	Phase Speed [m/s]		Nonlinearity μ'^{-}		$[(c-u_o)\phi(z)]_z$[1/s]	
Case	mode-1	mode-2	mode-1	mode-2	mode-1	mode-2
cf=4 without shear	-1.99	-0.906	-4.94	-2.11	0.0120	-0.0084
cf=4 with shear	-1.71	-0.696	-5.00	-1.43	0.0102	-0.0036

5.3.2 Results

The result of the case with circular cylinder showed evolution of the mode-1, -2 and -3 internal waves around the island. The modal structure was shown in the vertical velocity distribution (Figure 5.26). The mode-1 was subcritical as expected and propagated upstream, while mode-2 and -3 internal waves were trapped around the circular cylinder. The development of the each modal component was calculated from the orthogonal relation. The amplitude of the leading wave was at most 30 m and 40 m for mode-1 and mode-2 waves, respectively. The nonlinearity of the mode-2 internal wave, estimated from values of μ'^{-} shown in Table 5.7 and an amplitude of 40 m, was 0.08 or 0.06. Although the nonlinearity was weak, trapped mode-2 and mode-3 internal waves were manifested in the surface convergence field, and the parabola created by the mode-3 wave had a larger curvature because of its smaller phase speed (compared to mode-2 wave).

The effect of topography was more evident when the results of the cases with two type of the Gaussian-bell topography are compared. As the topography was composed of a wider Gaussian bell, the excitation of the internal mode-1 was prevented. For the Gaussian bell topography for the Miyake Island (Figure 5.29), the mode-2 internal wave components were barely discernable in the vertical velocity distribution. Since every case was super-critical far upstream, successive generation of the internal wave components may have been trapped somewhere upstream. However, the numerical simulation indicated that the role, in generating internal waves, of linear shear flow and the topography cancels each out each.

This was consistent with the studies conducted in the previous subsection. The island topography tended to generate positive components of the internal wave (elevation type wave), while the background linear shear flow tended to create negative components of the internal wave (depression type wave). Although the theory was developed for strongly stratified shear flow over a point symmetric mountain topography with the assumption $(U/Nh)^2 << 1$, Brighton (1978) showed that the interface was perturbed by both the background shear flow and the topography. According to the theory, the linearly sheared background flow ($U_z > 0$) induces a negative displacement, and the topography induces a positive displacement in front of the mountain topography. For the cases with a Gaussian bell type topography, it can be seen in the temperature distribution (Figure 5.28) that interface was displaced in a negative direction (like the result of cylinder case). Since the upper level had a larger velocity, a pressure anomaly should be larger compared to lower level at the stagnation point in front of the cylinder, as the Bernouill's law predicts. The fluid in front of the island topography was displaced, so the amount of vertical displacement was reduced with broader island topography.

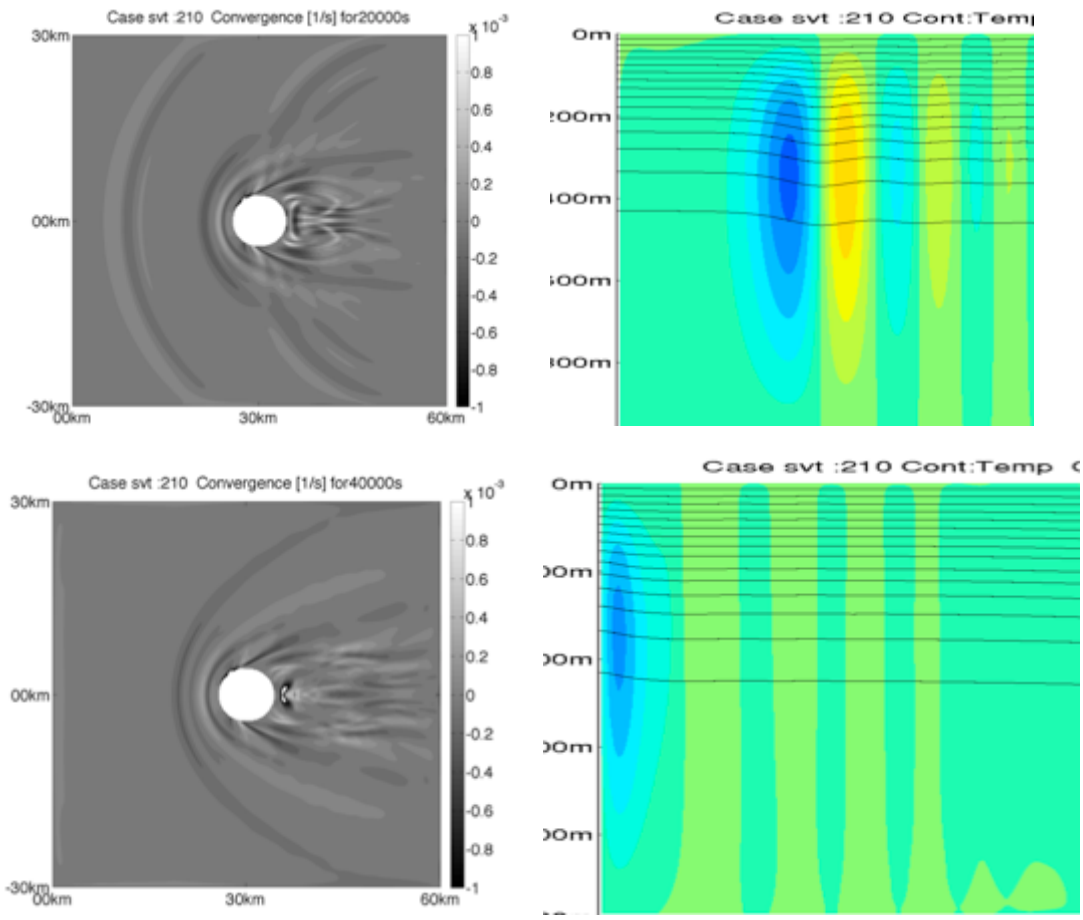

Figure 5.26　Surface velocity convergence (left) and temperature the distributions of temperature (contour) and vertical velocity (color) in the vertical section shown in red dashed line in left panels at t=20000s (top) and 40000s(bottom). Contour lines for temperature are shown with every 1 degree.

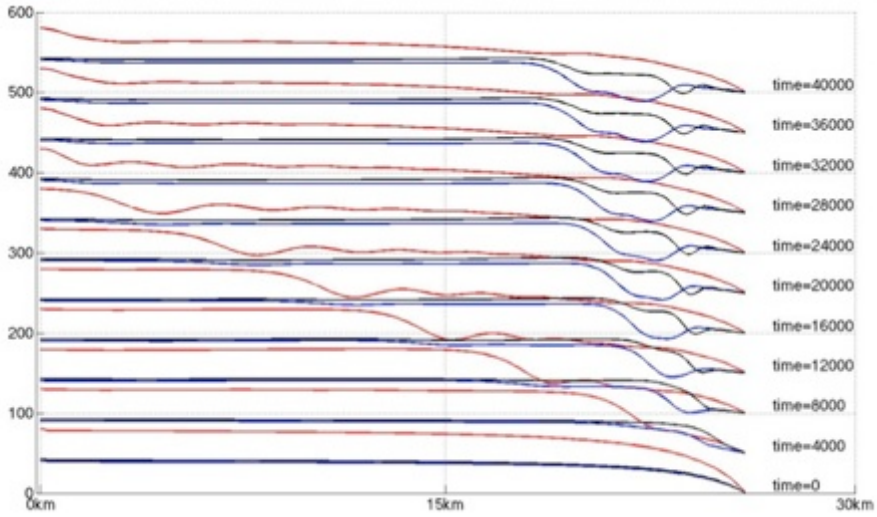

Figure 5.27　The evolution of the wave shape for each modal component calculated by the orthogonal relation. The lines are for mode-1(red), mode-2(blue) and mode 3(black).

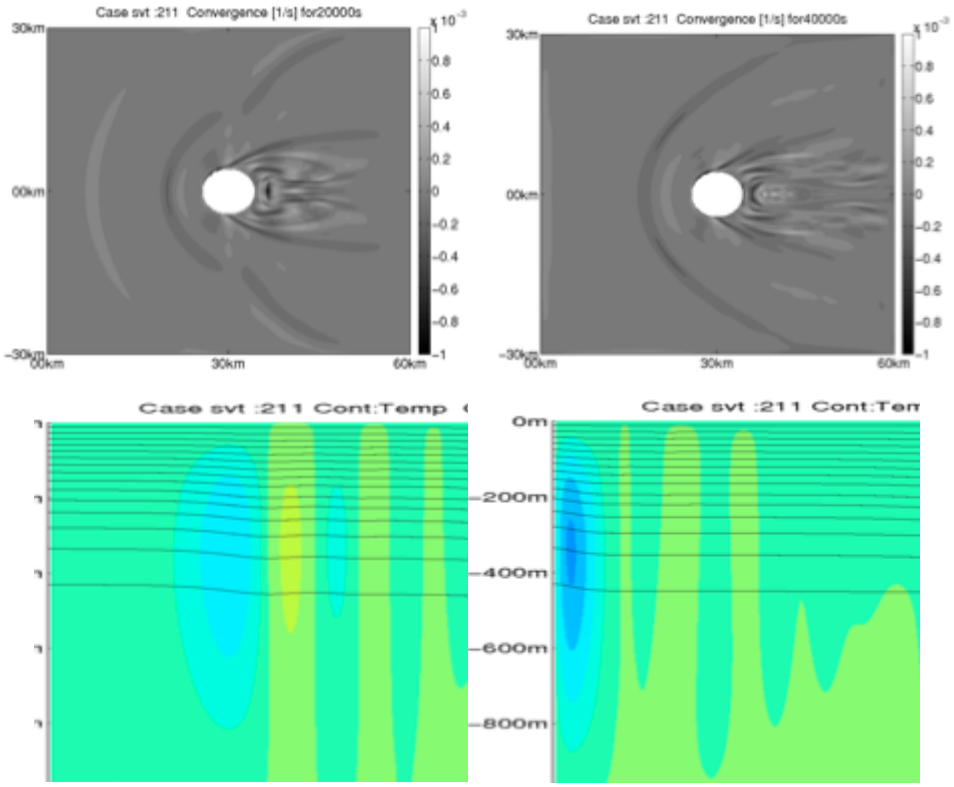

Figure 5.28 Same as Figure 5.26 but for the case of Gaussian Bell with $T_s = 1$.

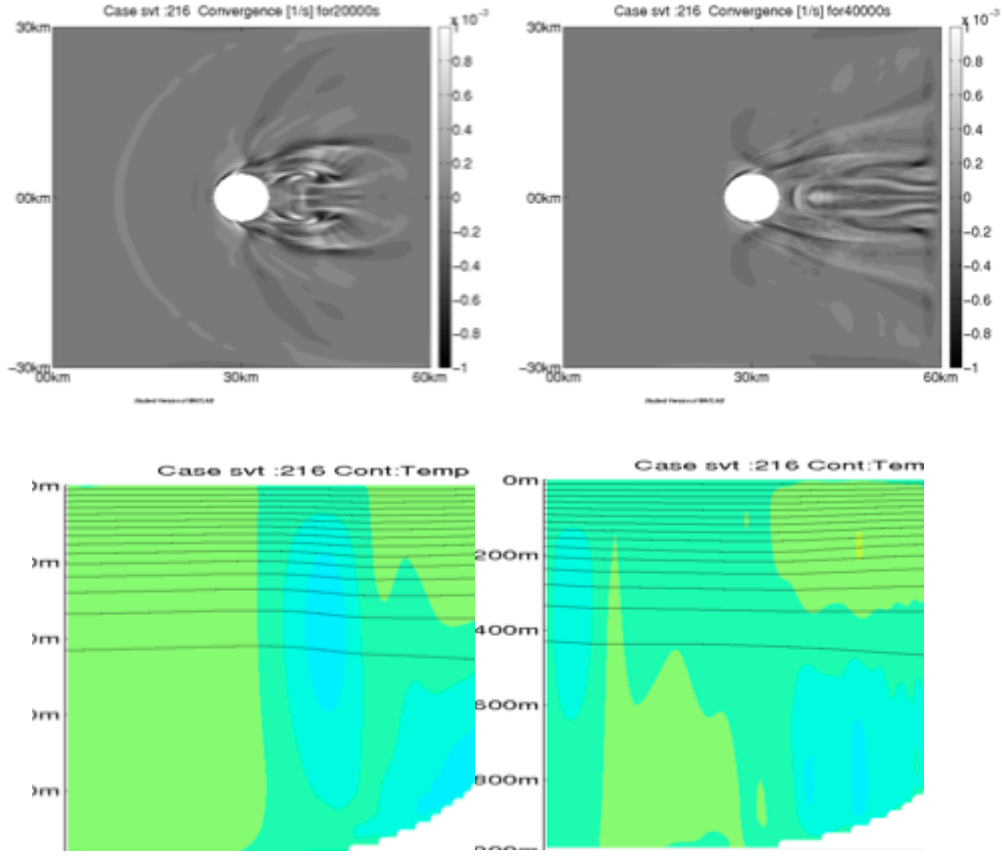

Figure 5.29 Same as Figure 5.26 but for the case of Gaussian Bell with $T_s = 6$.

5.4 Discussion and Summary

We conducted series of numerical simulations with simplified island topography and stratified shear flow. From the results of each series of numerical simulations, the following points were clarified.

Linearly stratified shear flow past the circular cylinder induced an internal displacement in front of the cylinder. In the near critical situation for the mode-1 linear internal wave, the displacement lead to a depression type mode-1 internal solitary wave train with a three-dimensional form. The three-dimensional internal wave had a parabolic shape in the horizontal dimensions and the shape was observed in the surface velocity field. The leading wave profile was close to a KdV solitary wave solution, and the phase speed was well estimated by weakly nonlinear KdV theory. These results indicate that background shear flow forces internal waves, and the generated internal waves lead to nonlinear internal waves. In addition to mode-1 wave generation, mode-2 waves were also generated very close to the circular cylinder. At the end of the numerical simulation, both the mode-1 and mode-2 waves were nearly at a steady state. This indicates that the island topography enabled the multi modes to be trapped in front.

However, there were the cases where nonlinear internal wave generation was not observed. One case was for the background shear flow with the opposite sign of vorticity from the previous cases. The other case was near critical flow for mode-2 waves. The former implies that sign of the forcing effect was important for the nonlinear internal wave generation which has polarity. The latter case would be related to the smaller forcing because the background flow speed was smaller, and the nonlinear coefficient had a smaller value. Therefore, the critical situation was not a sufficient condition to generate large amplitude nonlinear internal waves in front of the island.

Results of numerical simulation for vertical uniform flow past the Gaussian bell topography revealed that surface velocity field also showed a parabolic pattern. In the critical configuration for mode-1 waves, surface velocity was accelerated as the flow approached the topography, but then suddenly decreased. The acceleration were induced by mode-1 internal wave. Although the critical flow was set from the boundary conditions, the excited mode propagated downstream. That meant the flow was supercritical in front of the Bell topography. By reducing the Froude number to 0.8 at the boundary, the mode-1 wave was critical in front of the bell topography. A mode-1 internal wave was trapped and its magnitude was amplified with time. The generation of the depression type disturbance was related to the vertical velocity component excited by the mode-1 internal wave. The case for the Froude number of 0.6 was similar to the Fr = 0.8, although the trapped component was not a mode-1 but a mode-2 component. The result implies that Gaussian bell topography with vertically uniform flow produced a critical situation for some modes of internal waves within a wide range of the Froude numbers defined upstream.

The cases with linearly sheared flow and Gaussian bell topography were examined with focused attention on the situation of Miyake and Mikura islands. Since the configuration

was near critical for mode-2 internal waves, mode-1 internal waves propagated away at the beginning of the numerical simulation. The mode-2 wave was excited and trapped in front of the circular cylinder, but the amplitude decreased with as the topography broadened. The reason was suggested to be a modulation of the effect of pressure anomaly around the topography such which induced an interfacial displacement. The Bell topography prevents the interface from moving downward, and the generation of the internal wave was suppressed.

Since the Kuroshio had a stratified shear flow, the shear, as well as the topographic forcing, induced a perturbation. Although the description was qualitative, the series of numerical simulation showed that both the shear flow and the topography had a considerable influence on the generation of finite amplitude internal waves. In particular, the interaction reduced the generation of disturbances. However, the result was not directly applied to the actual case for Izu-Islands, particularly for the Miyake Island.

The numerical simulation with Izu-Islands topography showed internal waves were more likely to be trapped around the Miyake Island than the Mikura Island, while the numerical simulation result with isolated topography showed opposite. The complex topography such as the small island west to the Miyake Island converges and accelerates the flow, which is not reproduced in the simulation with isolated topography.

Compared to the Miyake Island, the Mikura Island had a near perfectly isolated, bell-shaped topography. Since the result of cylinder case and the Bell topography for the Mikura Island shared similar features, in particular the mode-2 internal wave with a parabolic signature was trapped around the island, we conclude that background shear flow was important for the nonlinear internal wave generation around the Mikura Island.

Chapter 6 Conclusion

Analyzing images obtained by of the ALOS/PALSAR in 138 days from 2006 to 2011, we have found more than 10 SAR images with parabolic patterns around the Izu-islands. Almost all of the images were taken during summer months. In addition, the parabolic patterns were only detected when the Kuroshio approached and the wind was gentle. These two conditions were necessary but not sufficient for the detection of the parabolic patterns. The results indicated that the parabola lines are manifestation of the oceanic internal waves, so we analyzed internal wave properties at the Kuroshio axis upstream the islands. As a result, absolute values of $[(c-u_o)\phi(z)]_z$ and μ' were maximal in the summer season suggested that the surface manifestation of internal waves was more likely in the summer than in the winter.

Therefore, both the wind and the internal wave properties during the summer increase the probability of detection of the internal waves by SAR. Since internal waves grow to finite amplitude under critical conditions, Froude numbers for each mode were estimated from existing observation and reanalysis. As a result, it was estimated that mode-2 internal waves were likely to be under critical condition around the island.

To demonstrate the idea, that the parabolic signatures around the islands were a manifestation of oceanic nonlinear internal waves trapped around the islands, more directly, non-hydrostatic numerical simulations were conducted. We set the initial and boundary conditions using vertical profiles of the Kuroshio axis reproduced in JCOPE2 reanalysis data. As a result, trapped mode-2 internal waves were observed. The comparison between the simulations with stratification for the summer and winter seasons revealed that mode-2 internal waves were trapped in both seasons, but the induced surface velocity is larger in summer season. This is consistent with the results of analysis on JCOPE2 reanalysis data. Therefore, the smaller induced velocity and the stronger wind prevented the imaging of the internal waves in winter.

To test the hypothesis that the parabolic signatures around the islands were a manifestation of oceanic nonlinear internal waves trapped around the islands, non-hydrostatic numerical simulations were conducted. We first set the initial and boundary conditions using vertical profiles of the Kuroshio axis reproduced in JCOPE2 reanalysis data. As a result, trapped mode-2 internal waves were reproduced. The trapped wave creates surface convergence area of parabola shape with its magnitude of $O(10^{-4})$. The comparison between the simulations with summer and winter stratifications revealed that mode-2 internal waves can be trapped in both seasons, but the induced surface velocity is larger in summer season. This is consistent with the results of analysis on internal wave properties with JCOPE2 reanalysis data that surface manifestation is magnified in summer months. Therefore, the smaller induced velocity and the stronger wind prevented the imaging of the internal waves in winter.

To obtain a better understanding about the generation of the three-dimensional nonlinear internal waves, numerical simulations with simplified isolated topography were

also conducted. Two situations, linearly stratified shear flow with circular cylinder and vertical uniform flow with Gaussian bell topography, were studied by setting near critical situation. The results of the two configurations indicated that both of the background shear flow and the bell topography induced the disturbance continuously and the finite amplitude wave are generated. The mode of trapped wave depends on Froude Number but the island topography admits several modes to be trapped. The cases with bell shaped topography representing the Miyake and the Mikura in Kuroshio were also studied. The results indicated that vertical shear flow played a central role in creating nonlinear internal waves around the Mikura Island with narrower bell shape. On the other hand, isolated topography is insufficient to reproduce the trapped internal waves around the broader Miyake Island even with a shear flow. The actual topography around the Miyake Island, such as small island west to the Miyake islands, is important for the generation of trapped internal waves.

We conclude that internal waves were trapped around the islands, and they are mainly responsible for the parabolic patterns shown in SAR images. The nonlinear character was not clearly observed when vertical profiles of the Kuroshio axis, reproduced from JCOPE2 reanalysis data, were used. However, the numerical simulation results with modified density and velocity profiles indicated that nonlinear internal waves can be generated and be trapped. Mode-1 nonlinear internal wave generation is also possible with a strong shock such as sudden approach of the Kuroshio, and the current speed variation for example by tide. The mode-1 wave is not likely to be trapped, but SAR may detect the transient situation. Further observational studies are necessary to definitively demonstrate the generation of three-dimensional nonlinear internal waves around the Izu-islands in Kuroshio.

Our study clarified that oceanic internal waves occur in the Izu-island region under the conditions when atmospheric wind is gentle and the Kuroshio approaches the Island. In addition, this study indicates that small-scale oceanic processes related to the Kuroshio around the Izu-Islands can be detected by SAR. The processes are spatially much smaller than the Kuroshio, but its effect should be quantitatively examined to understand the effects of Izu-Islands topography on the Kuroshio. Further observational and numerical studies are encouraged.

References

[1] Alpers, W., & Salusti, E. (1983). Scylla and charybdis observed from space. Journal of Geophysical Research: Oceans (1978–2012), 88(C3), 1800-1808.

[2] Alpers, W., & Hennings, I. (1984). A theory of the imaging mechanism of underwater bottom topography by real and synthetic aperture radar. Journal of Geophysical Research: Oceans (1978–2012), 89(C6), 10529-10546.

[3] Alpers, W. (1985). Theory of radar imaging of internal waves. Nature, 314(6008), 245-247.

[4] Alpers, W., & Huang, W. (2011). On the discrimination of radar signatures of atmospheric gravity waves and oceanic internal waves on synthetic aperture radar images of the sea surface. Geoscience and Remote Sensing, IEEE Transactions on, 49(3), 1114-1126.

[5] Arakawa, A., & Lamb, V. R. (1977). Computational design of the basic dynamical processes of the UCLA general circulation model. Methods in Computational Physics, 17, 173-265.

[6] Baines, P. G. (1998). Topographic effects in stratified flows Cambridge University Press.

[7] Benjamin, T. B. (1967). Internal waves of permanent form in fluids of great depth. Journal of Fluid Mechanics, 29(03), 559-592.

[8] Benjamin, T. B. (1966). Internal waves of finite amplitude and permanent form. J.Fluid Mech, 25(2), 241-270.

[9] Brandt, P., Alpers, W., & Backhaus, J. O. (1996). Study of the generation and propagation of internal waves in the strait of gibraltar using a numerical model and synthetic aperture radar images of the european ERS 1 satellite. Journal of Geophysical Research, 101(C6), 14237-14,252.

[10] Brighton, P. (1978). Strongly stratified flow past three - dimensional obstacles. Quarterly Journal of the Royal Meteorological Society, 104(440), 289-307.

[11] Burk, S. D., & Haack, T. (2000). The dynamics of wave clouds upwind of coastal orography. Monthly Weather Review, 128(5), 1438-1455.

[12] Camassa, R., Choi, W., Michallet, H., Rusas, P., & Sveen, J. (2006). On the realm of validity of strongly nonlinear asymptotic approximations for internal waves. Journal of Fluid Mechanics, 549, 1-24.

[13] Choi, W., & Camassa, R. (1999). Fully nonlinear internal waves in a two-fluid system. Journal of Fluid Mechanics, 396(1), 1-36.

[14] Duda, T. F., Lynch, J. F., Irish, J. D., Beardsley, R. C., Ramp, S. R., Chiu, C., . . . Yang, Y. (2004). Internal tide and nonlinear internal wave behavior at the continental slope in the northern south china sea. Oceanic Engineering, IEEE Journal of, 29(4), 1105-1130.

[15] Drazin, P. G. (1961). On the steady flow of a fluid of variable density past an obstacle. Tellus, 13(2), 239-251.

[16] Farmer, D., & Armi, L. (1999). The generation and trapping of solitary waves over topography. Science, 283(5399), 188-190.

[17] Fofonoff, N. P., & Millard, R. C. (1983). Algorithms for computation of fundamental properties of seawater.

[18] Grimshaw, R., & Smyth, N. (1986). Resonant flow of a stratified fluid over topography. J.Fluid Mech, 169, 429-464.

[19] Helfrich, K. R., & Melville, W. K. (2006). Long nonlinear internal waves. Annu.Rev.Fluid Mech., 38, 395-425.

[20] Hibiya, T. (1986). Generation mechanism of internal waves by tidal flow over a sill. Journal of Geophysical Research: Oceans (1978–2012), 91(C6), 7697-7708.

[21] Hibiya, T. (1990). Generation mechanism of internal waves by a vertically sheared tidal flow over a sill. Journal of Geophysical Research: Oceans (1978–2012), 95(C2), 1757-1764.

[22] Holloway, P., Pelinovsky, E., & Talipova, T. (2003). Internal tide transformation and oceanic internal solitary waves. Environmental stratified flows (pp. 29-60) Springer.

[23] Isoguchi, O., Shimada, M., Sakaida, F., & Kawamura, H. (2009). Investigation of kuroshio-induced cold-core eddy trains in the lee of the izu islands using high-resolution satellite images and numerical simulations. Remote Sensing of Environment, 113(9), 1912-1925.

[24] Jackett, D. R., & McDougall, T. J. (1995). Minimal adjustment of hydrographic profiles to achieve static stability. Journal of Atmospheric and Oceanic Technology, 12(2), 381-389.

[25] Jackson, C. (2007). Internal wave detection using the moderate resolution imaging spectroradiometer (MODIS). Journal of Geophysical Research: Oceans (1978–2012), 112(C11)

[26] Jackson, C. R., & Apel, J. R. (2004). Synthetic aperture radar marine user's manual US Department of Commerce.

[27] Jackson, C. R., & Apel, J. R. (2004). An atlas of internal solitary-like waves and their properties. Contract, 14(03-C), 0176.

[28] Johnson, E., & Vilenski, G. (2004). Flow patterns and drag in near-critical flow over isolated orography. Journal of the Atmospheric Sciences, 61(23), 2909-2918.

[29] Kawabe, M. (1995). Variations of current path, velocity, and volume transport of the kuroshio in relation with the large meander. Journal of Physical Oceanography, 25(12), 3103-3117.

[30] Kodaira. T, Waseda. T, Nakagawa. T, Isoguchi. O, Miyazawa. Y, Measuring the Kuroshio Current Around Miyake Island, a Potential Site for Ocean-Current Power Generation INTERNATIONAL JOURNAL OF OFFSHORE AND POLAR ENGINEERING, 23, (4):272-278; DEC 2013

[31] Koop, C. G., & Butler, G. (1981). An investigation of internal solitary waves in. J.Fluid Mech, 112, 225-251.

[32] Kubota, T., Ko, D., & Dobbs, L. (1978). Propagation of weakly nonlinear internal waves in a stratified fluid of finite depth. J.Hydronaut, 12, 157-165.

[33] Lawrence, G. A. (1993). The hydraulics of steady two-layer flow over a fixed obstacle. Journal of Fluid Mechanics, 254, 605-605.

[34] Lien, R., Tang, T., Chang, M., & D'Asaro, E. (2005). Energy of nonlinear internal waves in the south china sea. Geophysical Research Letters, 32(5)

[35] Liu, A., & Wu, S. (2001). Satellite remote sensing: SAR. Encyclopedia of Ocean Sciences, 5, 2563-2573.

[36] Liu, A. K., Ramp, S. R., Zhao, Y., & Tang, T. Y. (2004). A case study of internal solitary wave propagation during ASIAEX 2001. Oceanic Engineering, IEEE Journal of, 29(4), 1144-1156.

[37] Marshall, J., Adcroft, A., Hill, C., Perelman, L., & Heisey, C. (1997). A finite - volume, incompressible navier stokes model for studies of the ocean on parallel computers. Journal of Geophysical Research: Oceans (1978–2012), 102(C3), 5753-5766.

[38] Matsumoto, K., Takanezawa, T., & Ooe, M. (2000). Ocean tide models developed by assimilating TOPEX/POSEIDON altimeter data into hydrodynamical model: A global model and a regional model around japan. Journal of Oceanography, 56(5), 567-581.

[39] Maxworthy, T. (1979). A note on the internal solitary waves produced by tidal flow over a three-dimensional ridge. Journal of Geophysical Research, 84(C1), 338-346.

[40] McDougall, T. J. (2011). Getting started with TEOS-10 and the gibbs seawater (GSW) oceanographic toolbox

[41] Miyazawa, Y., Zhang, R., Guo, X., Tamura, H., Ambe, D., Lee, J., . . . Komatsu, K. (2009). Water mass variability in the western north pacific detected in a 15-year eddy resolving ocean reanalysis. Journal of Oceanography, 65(6), 737-756.

[42] Niwa, Y., & Hibiya, T. (2001). Numerical study of the spatial distribution of the M2 internal tide in the pacific ocean. Journal of Geophysical Research: Oceans (1978–2012), 106(C10), 22441-22449.

[43] Ono, H. (1975). Algebraic solitary waves in stratified fluids. Journal of the Physical Society of Japan, 39, 1082.

[44] Osborne, A., & Burch, T. (1980). Internal solitons in the andaman sea. Science, 208(4443), 451-460.

[45] Sourav Sil,Yasumasa Miyazawa, Sergey M. Varlamov, Toru Miyama, , Takuji Waseda, Xinyu Guo (2013): Topography-tide-interaction on the south of the Japan, Intrnational Workshop on Modeling the Ocean (IWMO-2013), Bergen, Norway, June 17 – 20, 2013

[46] Stastna, M., & Peltier, W. (2005). On the resonant generation of large-amplitude internal solitary and solitary-like waves. Journal of Fluid Mechanics, 543, 267-292.

[47] Turkington, B., Eydeland, A., & Wang, S. (1991). A computational method for solitary internal waves in a continuously stratified fluid.

[48] Usui, N., Tsujino, H., Nakano, H., & Matsumoto, S.Long-term variability of the kuroshio path south of japan. Journal of Oceanography, , 1-24.

[49] Whitham, G. B. (2011). Linear and nonlinear waves John Wiley & Sons.

[50] Yang, Y. J., Fang, Y. C., Chang, M., Ramp, S. R., Kao, C., & Tang, T. Y. (2009). Observations of second baroclinic mode internal solitary waves on the continental slope of the northern south china sea. Journal of Geophysical Research: Oceans (1978–2012), 114(C10)